UNIVERSITY OF CALIFORNIA, MERCED

From Quark Confinement to Dynamical History of Stars

A dissertation submitted in partial satisfaction of the
requirements for the degree
Doctor of Philosophy

in

Theoretical Physics

by

Davoud Masoumi

Committee in charge:

Professor Chih-Chun Chien, Chair
Professor Roland Winston
Professor Sarah Rose Loebman
Professor Jay E. Sharping
Professor James Edward Bernard

2024

The dissertation of Davoud Masoumi is approved, and it is acceptable in quality and form for publication on microfilm and electronically:

(Professor Roland Winston)

(Professor Sarah Rose Loebman)

(Professor Jay E. Sharping)

(Professor James Edward Bernard)

(Professor Chih-Chun Chien, Chair)

University of California, Merced

2024

DEDICATION

To anyone and everyone interested in knowing more about the universe!

EPIGRAPH

Wir müssen wissen, Wir werden wissen.

—David Hilbert

TABLE OF CONTENTS

LIST OF FIGURES

LIST OF TABLES

ACKNOWLEDGEMENTS

Thank you to everyone who supported me on my academic journey! The list of people I need to thank is indeed very long. Here, I follow the convention and mention only those who made recent contributions to the completion of this thesis. However, I will never forget the kindness and support of those not named here.

I would like to thank my advisor, Prof. Roland Winston, for providing invaluable advice that shaped my academic character and taught me how to think like a physicist. Thank you for the support you provided throughout my graduate school journey, for devoting your weekend time and hosting me in your house to help me find my way.

I would like to thank my co-advisor, Prof. Sarah Loebman, for her limitless patience, for giving me helpful pieces of advice, for providing direct access to the entire collection of FIRE-2 galaxy simulations and the national XSEDE supercomputer facility, for providing financial support in the form of GSR employment for a year and a half, for connecting me to influential people in the field of astrophysics, for allowing me to learn about astrophysics, for listening to me, for allowing me to mentor an undergraduate student, and for keeping me in her mind even during the hectic times. I also gratefully acknowledge the support provided by Grant HST-AR-16624.001-A for working on the study presented in the second part (in particular, Chapter 6) of this thesis.

I would like to thank Prof. Chih-Chun Chien for his unconditional support and for sharing his sense of scientific curiosity and humor. Prof. Jay Sharping, thank you for your caring and motivational support and insightful comments, which helped open my mind to new thoughts. Prof. James Bernard, thank you for the tremendous amount of time you spent for me to educate me about various subjects and for your genuine generosity.

I would like to thank my collaborators, Dr. Farid Charmchi and Prof. Leila Shahkarami, for allowing me to work with them, for teaching me patiently about

various aspects of high-energy physics, and for spending hours and hours giving me precious advice. I would like to sincerely thank Nima Arkani-Hamed for providing incredibly priceless pieces of advice.

I would like to thank my other collaborator, Prof. Nathan Kaib, for providing helpful guidance and sharing his insightful ideas with me, for spending a significant amount of time in the format of weekly meetings, and for kindly helping me refine our questions or analysis methods. I also would like to thank Prof. Andrew Wetzel for sponsoring me and allowing me to use UC Davis high-performance computing resources to conduct a significant portion of my data analysis tasks and for guiding me to know the right questions that galaxy simulations can address. I would like to thank numerous excellent astrophysicists, Prof. Josh Peek, Dr. Micheal Grudić, Prof. Mark Krumholz, Prof. Tom Quinn, Prof. Philip Hopkins, Dr. Matthew Orr, Prof. Peter Franchaboy, Prof. Andrea Ghez, Dr. Matthew Hosek, Prof. Janice Lee, Prof. Jamie Tayar, Prof. Gail Zasowski, Prof. Kathryne Daniel, Prof. Lina Necib, Dr. Catherine Zucker, Prof. Karen Masters, Prof. Daniel Beller, and Prof. Dustin Kleckner, who have generously and kindly shared their thoughtful insights with me. I would like to thank my great colleagues, labmates, and friends, Jamie Quinn, Dr. Isaiah Santistevan, Jonah Otto, Binod Bhattarai, Anna Yu, Maverick Oh, De Zhen Zhou, and Abdelaziz Hussein, for spending time with me to discuss problems and find potential solutions.

I would like to thank Prof. Linda Hirst, Prof. Ajay Gopinathan, Paul Roberts, Michelle Morrow, Belinda Braunstein, Robyn Lukens, Hamed Sadeghi, Dr. Sheida Riahinasab, Becky Mirza, Lacey Long Vejar, and the staff of graduate division for helping me to join UC Merced; I had to defer my acceptance for three semesters and without your help and support, I could not start the graduate program at UC Merced. I would like to thank the graduate group chair of the physics department, David Strubbe, for providing continuing support and always finding solutions to academic policies. Thanks to the physics department staff, Tom Martinez and Vanessa Lopez,

for their pure kindness and unconditional support.

I would like to thank Haik Stepanian, Dr. Kristina Callaghan, and Prof. Brian Utter for supervising me for my TA appointments with incredibly supportive manners, for their passion for teaching, and for helping me to improve my teaching skills. I thank my fantastic physics graduate cohorts, Dominique Davenport, Aaron Wheeler, Aluana Wheeler, and Kevin Collins, for their kindness and great attitude.

I would like to thank my friends, Ali Heydari, Amin Boroomand, Mohsen Sharifani, Alireza Aghalou, Mohammad Sohrabi, Ghazaleh Leylaz, Mina Naghshnejad, Ramuel Safarkoolan, Maryam Tabatabaeian, Shadab Tabatabaeian, Arghavan Alamatsaz, Sina Dehghan, and Ali Hasanzadeh for their help in the past seven years. I thank my long-lasting friends, Asad, Mohammad Sadegh, Ashkan, Keyvan, and Keysun, for being my real friends.

Finally, I want to give special thanks to my great teachers and friends, Prof. Pouria Pedram, Mahdi Mirzaeei, Dr. Shaahin Sharifi, Dr. Arash Ranjbar, Prof. Shahab Shahidi, Aslan Shiati, Prof. Amir Hadi Ziaie, Dr. Bahman Nadjian, Dr. Arian Vezvaee, Prof. Bijan Ahmadi, Prof. Hadi Salehi, Prof. Ebrahim Foulaadvand, Prof. Hamidreza Sepangi, Prof. Shahram Jalalzadeh, Prof. Krasoos Ghafoori Tabrizi, Prof. Mohammad Sepehri, Prof. Samad Haj Jabbari, Prof. Mahdi Behzad, Prof. Morteza Moniri, Prof. Pandora Raja, Prof. Mahdi Pourbarat, Prof. Vida Milani, Prof. Kasra Alishahi, Prof. Farshad Ebrahimi, Prof. Siamak Sadat Gousheh, Prof. Nima Khosravi, Prof. Hossein Shojaie, Prof. Shant Baghram, Prof. Sharmin Kharrazi, Prof. Mahmud Bahmanabadi, Prof. Masoumeh Ghasemkhani, Prof. Mahdi Golshani, Prof. Neda Sadooghi, Bardia Azimipanah, Dr. Mahsa Vahabi, Dr. Nader Moshiri, Babak Kazemi, Omid Eslami and Khosro Arghavani-fard for helping me over almost 20 years without any expectation.

Davoud Masoumi

Email: dmasoumi@ucmerced.edu

Phone: (209) 355-6416

COMPUTER SKILLS

Programming Language & Software
Python, Jupyter Notebook, Gluviz, Git, SQL, Mathematica, Maple, LaTeX

RESEARCH INTERESTS

- **Computational Physics:** Machine Learning, Mathematical Modeling, Big Data
- **Astrophysics and Cosmology:** Galactic Structure/Dynamics, Testing Dark Matter Theories, Star Formation, Interstellar Medium, Stellar Populations
- **String Theory:** Gauge/Gravity Duality

RESEARCH EXPERIENCE

- ***Ph.D. Thesis Research***
  University of California, Merced

  Exploring Galaxy Formation and Evolution in FIRE Simulations
  Jan 2022 – Present
  Advisor: Sarah Loebman

  - ❖ Studying the dynamical history of stars and star clusters.
  - ❖ Exploring the impact of the galactic environment on clustered star formation across the full range of galactic and ISM properties.
  - ❖ Examining the spatial correlation of star clusters and dense molecular gas.
  - ❖ Testing how individual channels of stellar feedback impact the clusters that form and the surrounding environment.
  - ❖ Inspecting how and why the Radcliffe Wave formed.

  The Notion of Duality; The Holographic Principle
  Jan 2018 – Dec 2021
  Advisor: Roland Winston

  - ❖ Using AdS/QCD correspondence to analyze and describe the Schwinger effect in SU(N) confining gauge theories.
  - ❖ Using AdS/CFT correspondence to explain gravity as an entropic force.

- ***Relativistic Quantum Information***
  Islamic Azad University (IAU), Science and Research Branch, Tehran, Iran
  Inspecting the cosmological aspects of relativistic quantum information.

- ***Noncommutative Quantum Field Theory***
  Shahid Beheshti University, Tehran, Iran
  Probing the result of the noncommutativity hypothesis in quantum mechanics and QCD.

- ***Thermodynamics and Statistical Mechanics***
  Institute for Studies in Theoretical Physics and Mathematics (IPM), Tehran, Iran
  Investigating one-dimensional Brownian motion in hard rods.

- ***BSc Thesis Research***
  Shahid Beheshti University, Tehran, Iran
  Studying classical wave motion in forced systems.

EDUCATION

Graduate Studies, *Physics*
University of California, Merced
GPA: 3.96

Bachelor of Science, *Solid State Physics*
Shahid Beheshti University, Tehran, Iran

PUBLICATIONS

- **D. Masoumi**, S. Loebman, A. Wetzel, et al., Open Star Clusters on FIRE: Identifying Young Massive Star Clusters at Present Day in the Latte Galaxy Simulations (in preparation)
- **D. Masoumi**, N. Kaib, S. Loebman, A. Wetzel, et al., Exploring the Dynamic History of Proxima and Alpha Centauri Analogs in FIRE (in preparation)
- S. Loebman, C. Zucker, **D. Masoumi**, B. Oseguera, A. Wetzel, et al., Radcliffe Wave on FIRE: Examining the Origin of Oscillatory Star Forming Gas Waves in the Milky Way (in preparation)
- **D. Masoumi**, L. Shahkarami, and F. Charmchi, Effect of electromagnetic fields on deformed AdS5 models, Phys. Rev. D **101**, 126011 (2020) (arXiv:1006.2475)
- M. Ebrahim Foulaadvand and **D. Masoumi**, Mechanical Filtering in forced-oscillation of two coupled pendulums, Phys. Educ. **27.1** (Jan-Mar 2010), pp.39-51 (arXiv:1006.2475)
- M. Ebrahim Foulaadvand and **D. Masoumi**, Investigating a one-dimensional oscillatory motion with constant restoring force, Gamma **21** (Winter 2009) (in Farsi, link)

CONFERENCE ATTENDED

- Surveying the Milky Way: The Universe in Our Own Backyard, ipac, Caltech – Pasadena, 23-27 October 2023.
- AAS 242, Albuquerque, 4-8 June 2023.
- APS April meeting, Minneapolis, 15-18 April 2023.
- AAS 240, Pasadena, 12-16 June 2022.
- APS April meeting, New York, 9-12 April 2022.
- New Physics from Precision at High Energies, Kavli Institute for Theoretical Physics at the University of California, Santa Barbara, 9 March - 21 May 2021.
- Zooming in on the Swampland, Harvard University, 8-10 March 2021.
- Cosmology at the crossroads (TMCC2021), SBU – Tehran, Iran, 22-25 Feb. 2021.
- CERN Winter School on Supergravity, Strings and Gauge Theory, CERN – Geneva Switzerland, 1-5 Feb. 2021.
- Recent Trends in String Theory and Related Topics, IPM – Tehran, Iran, 24-27 May 2016.
- Symposia on Quantum Computing and Quantum Information Processing and Experimental Aspects of Quantum Computing – Shahid Beheshti University (IRI) and Kinki University (JPA) – Tehran, Iran, 3-5 Jan. 2009.

SCIENTIFIC PRESENTATIONS

- ***Talk - APS April meeting, Minneapolis, April 2023***
  Response of a Holographic Confining Theory to External Electromagnetic Fields
- ***Poster Presentation - AAS 240, Pasadena, June 2022***
  Exploring the Dynamic History of Proxima and Alpha Centauri Analogs in FIRE (link)
- ***Talk - Cosmo-Gal 2022: UC Merced-Bryn Mawr College-Haverford College's Astrophysics Graduate Student Research Mini-Symposium***
  Exploring the Dynamic History of Proxima and Alpha Centauri Analogs in FIRE-2 Simulations
- ***Talk - APS April meeting, New York, April 2022***
  Effect of Electromagnetic Fields on Deformed AdS_5 Models
- ***Talk - Sharif University of Technology, Tehran, Iran, High Energy Physics Seminar, November 2020***
  Probing pair production in vacuum by an X-ray free-electron laser

AWARDS

- MacKenzie Scott Travel Award 2023
- UC Merced School of Natural Sciences Summer TA Top-Off Award 2022
- UC Merced Physics Department Outstanding Graduate TA Award 2021
- UC Merced Physics Graduate Group Summer 2021 Fellowship
- The 1st rank of the Islamic Azad University Master Program Entrance Exam 2014 among 10,000 participants
  LExS Silver scholarship 2014-2015

MENTORING & TEACHING EXPERIENCE

- ***Graduate Student Mentor*** ***Sept 2022 – Present***
  Department of Physics, University of California, Merced

  Mentor Biviana Oseguera, an undergraduate student, on a research project titled "The Radcliffe Wave on FIRE Simulation" in the field of astrophysics.

  - ❖ Assist with developing research skills (reviewing peer-reviewed articles, programming with Python, creating and keeping Jupyter Notebooks, using command-based interfaces), analyzing data (utilizing statistical methods), visualizing data (using Gluviz), and presenting findings (creating poster and LaTeX documents).
  - ❖ Conduct weekly meetings to discuss research progress, provide feedback, and plan for upcoming steps.
  - ❖ Co-author a research poster with Biviana Oseguera presented at the 242nd Meeting of the American Astronomical Society. Biviana won a Chambliss Astronomy Achievement award for her poster at the 242nd AAS meeting.
  - ❖ Co-authoring a manuscript based on the research project, which is currently in preparation for submission to The Astrophysical Journal.

- ***Workshop Organizer and Mentor*** ***May 2023 – July 2023***
  School of Natural Sciences, University of California, Merced

  - ❖ Volunteered as a mentor and organizer for the UC Merced Math and Computer Science Research Engagement (MCoRE) program — an outreach initiative program promoting research in Math and Computer Science to high school students, with a focus on underprivileged groups in the Central Valley.

- ***Teaching Assistant*** ***Sept 2010 – Dec 2021***

  School of Natural Sciences, University of California, Merced

  - ❖ Physics I –Bio, Physics I LAB –Bio, Introductory Physics II, Physics II –Bio, Physics II LAB –Bio, Calculus II

  Shahid Beheshti University, Tehran, Iran

  - ❖ Introductory Physics I, Introductory Physics II, Introductory Physics III, Calculus I, Calculus II, Differential Equation, Mathematical Physics I, Mathematical Physics II, Mathematical Physics III, Modern Physics I, Mathematical Analysis I, Algebra I, Linear Algebra

- ***Instructor*** ***June 2012 – Sept 2015***

  Problem-Solving Club, Physics Department of Shahid Beheshti University, Tehran, Iran

  - ❖ Teaching "An Introduction to Mathematica" to 70 first-year university students; holding regular lectures, assigning exercises and projects, designing and grading exams.
  - ❖ Instructing different problem-solving workshops:
    Complex Functions, Tensor Calculus, Variational Calculus, Green's Functions, Matrix Representation in Quantum Mechanics, Motion in Non-inertial Reference Frames.

- ***Tutoring*** ***June 2010 – Sept 2015***

  Andisheh Khordad Institute, Tehran, Iran

  - ❖ Instructing various intensive courses preparing high school students participating in the International Physics Olympiad (IPhO).

REFERENCES

- **Sarah Loebman**
  Assistant Professor, University of California, Merced.
  email: sloebman@ucmerced.edu
  phone: (805) 284-1648
- **Roland Winston**
  Director, UC Solar & Distinguished Professor, Schools of Natural Sciences & Engineering, University of California, Merced.
  email: rwinston@ucmerced.edu
  phone: (209) 201-2863
- **Chih-Chun Chien**
  Associate Professor, Department of Physics, Schools of Natural Sciences, University of California, Merced.
  email: cchien5@ucmerced.edu
  phone: (209) 228-2224
- **Leila Shahkarami**
  Assistant Professor, School of Physics, Damghan University, Damghan, Iran.
  email: l.shahkarami@du.ac.ir
- **Pouria Pedram**
  Assistant Professor, Department of Physics, Science and Research Branch, Islamic Azad University, Tehran, Iran.
  email: p.pedram@srbiau.ir

ABSTRACT OF THE DISSERTATION

From Quark Confinement to Dynamical History of Stars

by

Davoud Masoumi
Doctor of Philosophy in Theoretical Physics

University of California Merced, 2024

Professor Chih-Chun Chien, Chair

This thesis includes two parts discussing two fascinating areas of fundamental physics. **Part (I)** explores the enigma of quark confinement within the intricate domain of quantum field theory, addressing a foundational puzzle in particle physics. Quark confinement dictates that quarks are bound within hadrons, so we cannot observe quarks as free, isolated particles. Despite extensive efforts over the past fifty years, the theoretical foundation of quark confinement in quantum chromodynamics (QCD) is still unclear. Studying the Schwinger effect (particle-antiparticle pair creation in vacuum in the presence of a strong external electromagnetic field) can pave the way to explore the behavior of quarks within hadrons. We utilize an indirect method, in particular the so-called AdS/QCD correspondence, to investigate the response of a QCD-like gauge theory to a static electromagnetic field. AdS/QCD correspondence is a form of gauge/gravity duality. This duality connects a gauge theory (representing particle physics) to a gravitational theory (specifically, string theory with an Anti-de Sitter background metric). Leveraging this method enables us to study the Schwinger effect for quark-antiquark pairs through potential analysis and calculation of the pair-production rate Γ. Our findings show that both the potential analysis and the calculation of the pair-production rate yield consistent results. We identify two

critical electric fields E_s and E_c as lower and upper bounds of a range in which pair production can occur only by tunneling through a potential barrier. Below E_s, the potential barrier is insurmountable, and pair production cannot happen. Above E_c, there is no potential barrier to restrict the pair production. While previous studies have explored various aspects of the Schwinger effect using AdS/QCD duality, further investigation is required for scenarios involving QCD-like gauge theories with simultaneous electric and magnetic fields. Addressing this research gap, our findings reveal that a magnetic field perpendicular to the electric field suppresses Γ and increases E_s. Conversely, a purely parallel magnetic field does not influence the system's response to an external electric field but enhances Γ in the presence of a perpendicular magnetic field. **Part (II)** ventures into the cosmos, examining the formation of young stellar groups (both bound star clusters and unbound stellar associations) within a full cosmological context. A young stellar group is a collection of newly born stars moving together as a relatively coherent unit through a galaxy. Recent observational advancements, driven by improved precision of Gaia DR3, along with complementary near-field studies like PHANGS-HST and PHANGS-JWST, have significantly enhanced our understanding of stellar groups in the Milky Way and local universe galaxies, enabling us to study the conditions and environment that set clustered star formation across a statistically significant sample. Yet despite the exciting progress in observations, there is still a notable absence of robust theoretical cosmological models to interpret the data. Recent advancements in generating galaxy zoom-in simulations enable the comprehensive study of the formation and evolution of giant molecular clouds and stellar groups within a cosmological galactic framework and, in turn, facilitate filling the gap between observations and theoretical models. We present the fundamental properties of young massive stellar groups, both bound and unbound, formed within or near the galactic disk at the present time (at redshifts $z < 0.008$) in the *Latte* suite of FIRE-2 Milky Way-like galaxy simulations. Our analysis encompasses the measurement of various characteristics for each stellar group,

including its boundedness, mass, size (stellar group's radius), 1D velocity dispersion, dispersion in age, and dispersion in metallicity [Fe/H]. We find the properties of simulated stellar groups with ages between 0 and 3 million years are within the range of values reported in observational studies. Our results depict the capability of *Latte* simulations to generate reasonably realistic star clusters and associations and set the stage for the forthcoming project that will focus on generating synthetic images of the simulated stellar groups and measuring their properties by utilizing the conventional pipelines used in observational studies. This approach will allow a more consistent comparison between simulations and observations, aiding in the establishment of benchmarks for interpreting observations and advancing our understanding of various aspects of galaxy formation, such as stellar evolution, the impact of feedback on galactic dynamics, and the processes involved in star and planetary system formation.

Chapter 1

An Introduction to Quark Confinement

The ultimate purpose of this chapter is to describe the puzzle of quark confinement, which has remained an open question in the realm of particle physics and quantum field theory (QFT) for several decades. We start by reviewing the history of physics through the lens of particle physics to highlight the key ideas and motivations that have led us to our current understanding of this mysterious puzzle. After setting the stage, we explain the quark confinement in the final section.

1.1 From Classical Physics to Quantum Mechanics

One of the most outstanding achievements of the 17th century was the invention of classical mechanics. Despite the great success of classical mechanics in describing the physics of mechanical waves and the motion of particles at large scales, it failed in various ways. It postulates instantaneous action at a distance. Moreover, postulating absolute space and time leads to finding Galilean transformation. These were

inconsistent with the fact that Maxwell equations respect Lorentz transformation instead of Galilean transformation. Some of the other well-known failures of classical mechanics include its inability to explain the spectrum of the hydrogen atom, wave properties of matter and electron diffraction, and the experimental results of the Compton effect. Efforts to resolve these fundamental problems ended up with finding the special theory of relativity and the theory of quantum mechanics at the beginning of the 20th century.

Despite the limitations of classical mechanics, the following are some of the most important lessons and ideas we learned from it. These lessons and ideas are essential for finding and developing more fundamental theories. Classical mechanics sets the stage to explain the universe by introducing a set of quantities, such as mass, potential, force, momentum, velocity, and position. It introduces the concept of field. Also, it tells us about the connection between symmetries and the conservation laws of nature (the beautiful Noether theorem). In addition, establishing the three astonishing and equivalent formalisms, Lagrangian, Hamiltonian, and Hamilton-Jacobi, which were initially developed in classical mechanics, provides a powerful tool for studying a system of particles. The core idea of these formalisms is the foundational basis for finding and developing theories that explain the laws of nature at a deeper level.

1.2 From Quantum Mechanics to Quantum Field Theory

Quantum mechanics successfully explains the spectrum of atoms; the aim for that it was developed. By solving the Schrodinger equation, one can find the discrete energy levels of electrons bound to an atom's nucleus, which is an outstanding achievement. It also informs us about spin, an intrinsic property of subatomic particles.

Quantum mechanics also gives us insight into wave-particle duality, the uncertainty principle, and the measurement mechanism in subatomic scales. It teaches us about the quantum entanglement opposing our intuition, which is mainly developed based on an understanding of macroscopic scales. It informs us about the Pauli exclusion principle, Fermi's golden rule, and in general transition rules (a.k.a. selection rules). Furthermore, studying the Bohm-Aharonov effect [3] by quantum mechanics illustrates the connection between the geometry of space and the phase of a wave function. In addition to all these great lessons, John Von Neuman taught us how to make a transition from classical mechanics to quantum mechanics by utilizing a rigorous mathematical prescription [215].

Despite quantum mechanics' spectacular successes, there are several fundamental issues with this successful theory. In particular, two issues can be easily recognized at first sight. First, quantum mechanics does not respect the Special Relativity. It can be seen from the Schrodinger equation: it includes a first-order derivative for time, while the derivative for space is a second-order derivative. Second, quantum mechanics studies systems only with a conserved number of particles. However, with the discovery of fundamental particles, we know there are events where the number of fundamental particles is not conserved. For instance, a muon μ^- can decay into three particles: an electron e^-, an electron antineutrino $\overline{\nu_e}$, and a muon neutrino ν_μ [209, 189, 82].

$$\mu^- \longrightarrow e^- + \overline{\nu_e} + \nu_\mu \tag{1.1}$$

Resolving these issues needed proposing and developing revolutionary ideas. Among competing theories, quantum field theory (QFT) could simultaneously resolve the aforementioned issues and explain the experimental results of the growing field of particle physics [206, 196, 162].

1.3 Discovery of Elementary Particles and New Fundamental Forces

Twenty-three years after the discovery of the electron by J. J. Thomson in 1897, Ernest Rutherford in 1920 identified the hydrogen nucleus as an elementary particle and named it a proton. In 1932, positron was discovered, and since then, a large family of fundamental particles has been discovered [82]. The discovered elementary particles include leptons (electron, electron neutrino, muon, muon neutrino, tau, tau neutrino), hadrons (proton, neutron, pion, kaon, and many others), quarks (up, down, charm, strange, top and bottom) which are the building blocks of hadrons, and another group of particles named force carriers (photon, gluon, W and Z boson) and of course the Higgs boson.

In addition to these elementary particles, two new fundamental forces have been discovered in the past century. In the 1930s, Enrico Fermi discovered a new fundamental force called *weak nuclear force* [59, 219]. In the same decade, Ernest Rutherford, following his studies on the nucleus of atoms, discovered another fundamental force named *strong nuclear force*.

1.4 Quantum Field Theory

As we discussed in the previous sections, it was essential to develop a theory beyond quantum mechanics to study the physics of elementary particles. Between 1946 and 1950, Shinichirō Tomonaga [208], Julian Schwinger [197, 198], Richard Feynman [60, 61], and Freeman Dyson [55, 56] established the theory of quantum electrodynamics (QED), a quantum description of interactions between charged particles. This theory is consistent with Special Relativity and can successfully explain the scattering processes. QED also has achieved several remarkable feats. It accurately

predicts the fine structure of the hydrogen atom's spectral lines. It also predicts the electron's anomalous magnetic moment, which refers to the deviation of the electron's magnetic moment from the value predicted by classical electromagnetism. QED showed us how to transition from quantum mechanics to a more fundamental theory called quantum field theory (QFT) or gauge theory.

Quantum field theory assumes the existence of a specific type of charge and one or more than one force carrier corresponding to each of the four fundamental forces of nature. For electromagnetic interactions, the charge is called electric charge, and the particle that carries the force of electromagnetism is called photon. There are only two types of electric charges, conventionally named positive and negative. Regarding the electric charge, there is only one type of photon because they have no electric charge. It is notable that photons carry the force of electricity and magnetism while having no electric charge.

The charge associated with the strong nuclear force is called color charge, and this force is carried by gluons. There are three types of color charges and three types of anti-color charges, conventionally named red, green, blue, antired, antigreen, and antiblue. These so-called color charges are not related to actual colors. Gluons do not have a specific color in the way that quarks do; instead, they carry combinations of color and anti-color charges, resulting in eight possible color combinations: red-antired, red-antigreen, red-antiblue, green-antired, green-antigreen, green-antiblue, blue-antired, blue-antigreen. The QFT that describes strong nuclear interactions between quarks and gluons is called quantum chromodynamics (QCD) [81].

The charge associated with weak nuclear force is named weak isospin (T), which is a quantum number analogous to electric charge in electromagnetism, and three particles W^+, W^-, and Z^0 carry the weak nuclear force. The three force carriers, W^+, W^-, and Z^0, have weak isospin values of $+1$ and -1, and 0, respectively, while the weak isospin of other particles can take on values of $+1/2$ or $-1/2$. The established QFT to explain the weak nuclear interaction is called the weak interaction theory

[16, 17, 74, 160].

We still do not have a QFT explaining the gravitational interactions, but it is evident that the charge corresponding to this force must be mass. The carrier of the force of gravity is a particle called graviton. Mass can be only positive or zero, and there is typically only one type of graviton because they are proposed as massless particles in standard theoretical frameworks.

1.5 Classification of Elementary Particles

It is common to classify elementary particles into two groups, fundamental and composite particles as shown in Fig. 1.1.

1) Fundamental particles: The fundamental particles are indivisible particles. In other words, there is no experimental evidence that they are made of finer particles. Based on their spins, they can be classified as follows:
- Bosons: The Higgs particle and all force carriers fall within this group.
- Femions: This group include six leptons (e, ν_e, μ, ν_μ, τ, ν_τ) and six quarks (u, d, c, s, t, b). Leptons do not have color charges, and for each lepton, there is an anti-particle with the same mass but the opposite electric charge. In the contrary, quarks have both electric and color charges, and for each quark, there is an anti-particle with the same mass but the opposite electric and color charge.

2) Composite particles (hadrons): Composite particles are made of quarks. Based on their spins, they can be classified into two groups:
- Bosons: Composite particles, which are bosons, are called mesons. They are made of a quark and an antiquark. Pion and kaon are some examples of mesons.
- Femions: Composite particles, which are fermions, have a particular name, baryons. These particles are made of three quarks. If a particle is made of three antiquarks

instead of three quarks, we call it an antibaryon. Protons and neutrons are the most known examples of brayons.

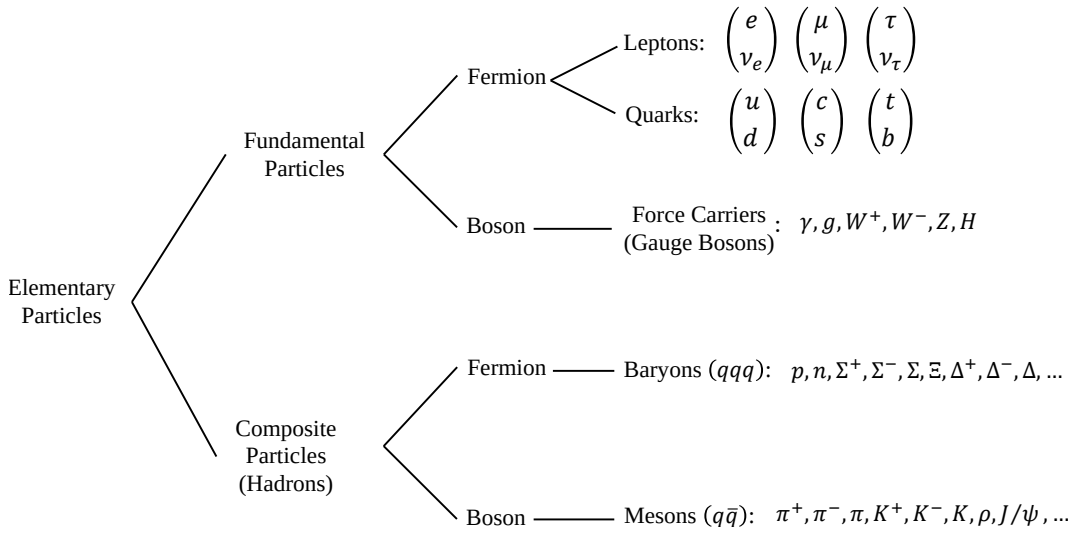

Figure 1.1: A simple classification of elementary particles.

Properties of elementary particles are listed in Ref. [82] in detail, and Ref. [85, 77, 161] describe the discovery of fundamental particles and some hadrons.

1.6 Complexity of QCD

In general, QCD computations are more complex than QED computations [76]. As mentioned in the former sections, besides having positive or negative electric charges (like electrons and protons), quarks and gluons also have color charges. Despite the electric charge that has only two possible states (positive and negative), the color charge can have six states: red and antired, green and antigreen, and blue and antiblue. This diversity of possible states of the color charge illustrates why QCD is more complicated than QED. However, this is not the end of the story. It should be noticed that photons (the carrier of the electromagnetic force) do not have an

electric charge, so two photons cannot directly interact via electromagnetic force. In contrast, gluons (the carrier of the strong nuclear force) have color charges which means gluons can interact directly with each other via strong nuclear interactions. Consequently, QCD should consider the interaction between gluons, interactions between gluons and quarks, and interactions between quarks. This is another source of higher-order complexity in QCD computations compared to QED.

1.7 Quark Confinement

Quark confinement states that quarks are bound within hadrons, so we cannot observe quarks as free, isolated particles [153]. A hadron can be thought of as a bag of quarks and gluons. A simple model for the potential of hadrons is

$$V(r) = -\frac{k_1}{r} + k_2 r \tag{1.2}$$

where k_1 and k_2 are two constants. The first term corresponds to a Coulomb-like potential and it dominates in small values of r. As shown in Fig. 1.2, the second term dominates at large values of r and dictates the confinement of quarks within hadrons.

Although this simple model can help us gain valuable insights, it does not explain all aspects of the behavior of quarks and gluons. For instance, this model cannot explain the complicated characteristics of the coupling constant of QCD. The coupling constant is a dimensionless parameter that reflects the strength of each specific type of interaction. The coupling constant of QCD is called *strong coupling* and is usually shown by α_s in the literature. Here we emphasize on some specific characteristics of α_s :

1. $\alpha_s >> \alpha$**:**

   The value of strong coupling α_s is much larger than the coupling constant of QED, α, in the range of present experiments. Consequently, in contrast with

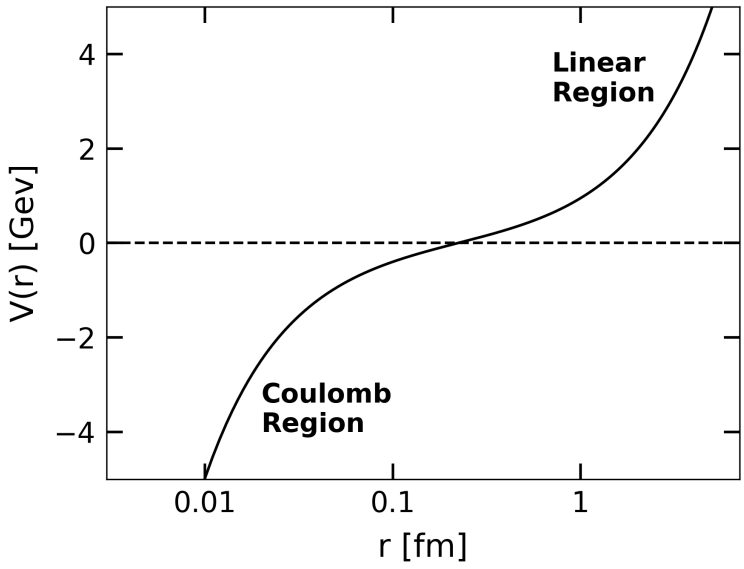

Figure 1.2: The strong interaction potential of charmonium (a bound state of charm and anticharm quarks) with $k_1 \approx 0.05\ GeV$ and $k_2 \approx 1\ GeV/fm$.

QED, employing the perturbation theory —the method of calculating interaction probabilities in terms of powers of the dimensionless coupling constant— becomes very complicated and often impossible in QCD. Thus, problems in the realm of QCD often fall in the non-perturbative regime of QFTs.

2. **Running coupling constant:**
   A central feature of the QCD is the running of its coupling constant α_s [162]. In both QED and QCD, the values of α_s and α are not determined theoretically from fundamental principles. To specify the value of α, we must measure some quantity that is sensitive to the magnitude of the electron's electric charge. For the case of α_s, we face a complicated situation, because α_s changes rapidly with the quark's wavelength at a distance of $\sim$ 1 fm. In terms of the quark equivalent energy $E = hc/\lambda$, the strong coupling $\alpha_s \approx 1$ at $E = 1\ GeV$, while

$\alpha_s \approx 0.1$ at $E = 100\ GeV$. It is why the α_s is known as the *running coupling constant*.

A direct result of this feature is the *asymptotic freedom* of quarks. In 1973, the concept of asymptotic freedom of quarks was theoretically realized by H. David Politzer [166, 45], David Gross, and Frank Wilczek [79, 78, 80], and it is experimentally verified [21, 223]. This concept states that while quarks are confined in hadrons, the shorter the distance between quarks, the more they behave like free particles. As we discussed, at shorter distances $E = hc/\lambda$ is larger and α_s is smaller, so quarks are less impacted by the strong nuclear interactions.

At the lowest order in energy, the variation of α_s with energy, shown in Fig. 1.3, can be expressed as

$$\alpha_s(E) = \frac{12\pi}{(33 - 2n_f)\ln(\frac{E^2}{\Lambda^2})} \tag{1.3}$$

where n_f is the number of quark flavors that can be involved in a binding process, and Λ is a *mass scale* constant [179]. At energies much greater than the quarks' mass energies, all flavors of quarks can be involved. The mass scale constant Λ must be determined only by experiments. This constant defines a boundary in energy: below the boundary hadrons exist, and above the boundary, quarks are not confined. The value of this constant is in the order of magnitude of the rest mass of the lightest hadron, pion [†1]. From experiments, $\Lambda \approx 0.2\ GeV$.

In brief, the theoretical foundation of quark confinement in QCD is still unclear. Noting the running of α_s, quark confinement occurs in the non-perturbative regime of QCD, where traditional perturbative methods break down. In addition, from

[1†] The mass of pion $\approx\ 0.135 MeV$.

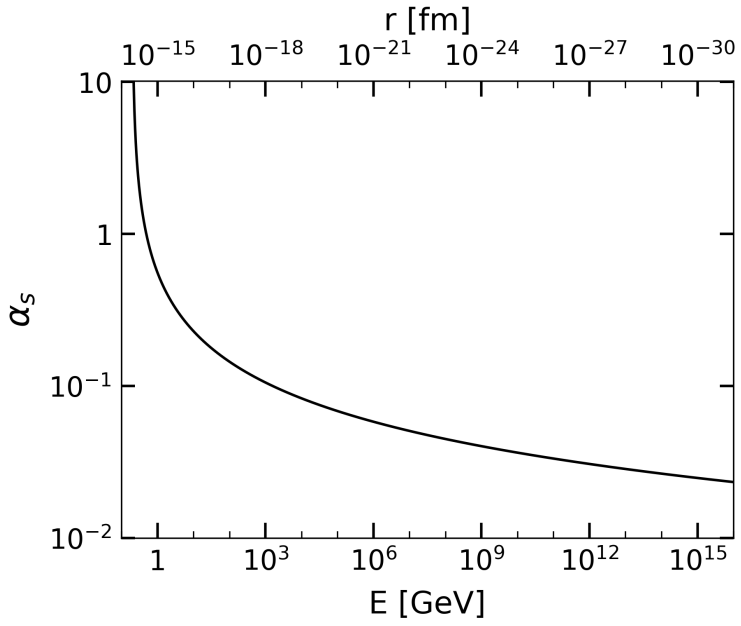

Figure 1.3: Running of strong coupling constant.

a different perspective, quark confinement arises from the non-Abelian characteristic of the strong nuclear interaction described by QCD [79], leading to complicated dynamics involving gluon self-interactions [162]. In the past decades, significant computational and analytical efforts have been made to develop new tools and techniques to study the non-perturbative regime of QCD. One approach to this is lattice QCD, a powerful numerical technique. However, it is computationally intensive and requires sophisticated algorithms to simulate the behavior of quarks and gluons in confinement accurately. Regarding analytical efforts, anti-de Sitter/quantum chromodynamics correspondence (AdS/QCD) offers a different route to attack the problem and provides exciting results. We discuss AdS/QCD and employ it to study quark confinement in Chapter 4.

In this thesis, we investigate quark confinement by analyzing the creation of quark and antiquark pairs in the presence of a strong external field, akin to the Schwinger

effect in QED, where electron-positron pairs are generated. Chapter 2 reviews the Schwinger effect for electron-positron pairs from an experimental standpoint, while Chapter 3 introduces tools essential for our study. In Chapter 4, we apply these tools to examine the Schwinger effect for quark and antiquark pairs using AdS/QCD, aiming to shed light on the puzzle of quark confinement.

Chapter 2

Schwinger Effect from Experimental Perspective: Pair Production from Vacuum at the Focus of an X-Ray Free-Electron Laser

It is known that the vacuum in quantum field theory (QFT) in the presence of external fields, such as electromagnetic fields, is unstable. In particular, electron-positron (e^+e^-) pairs can be created by a strong static electromagnetic field. The phenomenon is called the Schwinger effect [199] and is currently on the verge of being experimentally tested by using an X-ray free-electron laser (XFEL) [177]. In the last two decades, several XFELs have been constructed. The X-ray pulses produced in the SPring-8 Angstrom Compact free-electron Laser (SACLA), in the Linac Coherent Light Source (LCLS) at Stanford Linear Accelerator Center (SLAC), in the European XFEL, in the Tera Electron Volt Superconducting Linear Accelerator (TESLA)

XFEL at Deutsches Elektronen-Synchrotron (DESY), as well as in the FERMI at Elettra-Sincrotrone Trieste are far shorter than the pulses from the other X-ray sources. Their peak brilliance is approximately eight orders of magnitude higher [194]. These X-ray lasers may pave a way to make the laser beam radius in the range of its wavelength to obtain powerful electric fields—much stronger than the electric fields produced by optical lasers [29]. In the present chapter, we discuss the possibility of using X-ray lasers to get electric fields strong enough for a direct laboratory test of the Schwinger effect.

2.1 Introduction

Among the other effects leading to the production of particles, like Hawking radiation and the creation of particles in an expanding universe, the Schwinger effect is a compelling case because of its importance in understanding different aspects of quantum field theories (QFTs). The rate of pair production due to the impact of a static electric field is non-analytic [199]; this reveals the non-perturbative nature of the Schwinger effect. Therefore, this phenomenon not only can be used to explore the non-perturbative regime of QFTs but also provides an experimental tool to test the results in the non-perturbative regime, which has not been investigated deeply. Furthermore, it plays a crucial role in many problems of phenomenological and cosmological interest like quantum evaporation of black holes [89, 44, 70, 68], giving rise to gamma-ray bursts [175] and particle production in both hadronic collisions [39, 6, 23] and the early universe [156, 24].

A classical description might be useful to understand the Schwinger effect intuitively [151]. We imagine a virtual (e^+e^-) pair at a distance l from each other in a static electric field of strength E. If the energy of the virtual pair eEl received from the electric field exceeds the energy corresponds to the rest mass of the pair $eEl \geq 2m_ec^2$, they become real particles. The typical distance l between a vir-

tual (e^+e^-) pair is of the order of the reduced Compton wavelength of the electron $\lambda\!\!\!^{-}_e = \hbar/m_e c$. As a result, the minimum strength of the electric field to cause pair production equals $2m_e^2c^3/e\hbar$.

The exact formula for the minimum required strength of the electric field and the rate (per unit volume) of spontaneous (e^+e^-) pair production (SPP), $\Gamma_{\rm SPP}$, in a static electric field can be found from a full consideration in quantum electrodynamics [199, 188, 91],

$$\Gamma_{\rm SPP} \propto \exp\left(-\pi\frac{E_c}{E}\right) \tag{2.1}$$

where,

$$E_c = \frac{m_e c^2}{e\lambda\!\!\!^{-}_e} = \frac{m_e^2c^3}{e\hbar} = 1.3\cdot 10^{18}(\mathrm{V/m}). \tag{2.2}$$

Thus, a measurable $\Gamma_{\rm SPP}$ requires extraordinarily enormous electric field strengths of the order or above $10^{18}(V/m)$. For $E \ll E_c$, the SPP may occur only via quantum tunneling mechanism, and its corresponding production rate exponentially suppresses.

In the 1970s, people were interested to know whether optical lasers could make it possible to investigate the Schwinger effect's verification [31, 28]. They found out that the power density of available optical lasers was not enough for a sizeable pair creation rate [31, 65]. Simultaneously, the question was raised whether the required electric field strengths could be generated microscopically in the collision of heavy ions with $Z_1 + Z_2 > Z_c \approx 170$ [12, 222, 152]. Till the present time, it still seems impossible to produce macroscopic electric fields of the order of magnitude of the critical field strength in the laboratory, and there is still no clear experimental signal to verify SPP in heavy-ion collisions with a significant lifetime [75].

In the last two decades, several XFELs have been constructed, for instance, SACLA, LCLS at SLAC [10, 135], TESLA XFEL at DESY [29, 143, 144, 1] and FERMI at Elettra-Sincrotrone Trieste. These X-ray lasers may pave a way to make the laser beam radius in the range of its wavelength, $\sigma \geq \lambda \simeq \mathcal{O}(0.1)$ nm, to get

powerful electric fields,

$$E_c = \sqrt{\frac{\mu_0 c P}{\pi \sigma^2}} \simeq 1.1 \cdot 10^{17} (\mathrm{V/m}) \left(\frac{P}{1(\mathrm{TW})} \right)^{1/2} \left(\frac{0.1(\mathrm{nm})}{\sigma} \right) \tag{2.3}$$

much stronger than the produced electric fields by optical lasers of the same peak power P.

Here, we review recent work on SPP at the focus of XFELs [177, 178, 172, 167] and discuss the possibility of using X-ray lasers to produce electric fields strong enough for a direct laboratory test of the Schwinger effect.

2.2 Basic principles of XFELs

The principle of the Free-Electron Laser (FEL) was proposed in 1971 [120, 27]. The most common kind of lasers, optical lasers, radiate in the optical band because the gain in optical lasers is the result of cooperative stimulate emissions of electrons bound to the atoms of the material used in the laser. In XFELs, as we will discuss, the amplification medium instead is microbunches of unbound electrons [194]. These electrons are accelerated to relativistic speeds to emit X-rays, and they have a characteristic charge density modulation to guarantee the coherence of the radiated X-rays. In this section, we review the basic principles of XFELs.

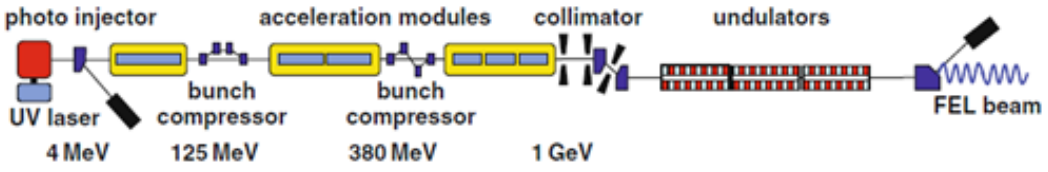

Figure 2.1: Schematic view of the UV and soft X-ray FEL FLASH at DESY (Ref. [194], Fig. 8.1).

2.2.1 XFEL

Here, we explain the procedure of producing intense and short flashes of remarkably coherent light in XFELs, usually built alongside a synchrotron storage ring, cf. Fig. 2.1. In the first part of a typical FEL, there is a photoninjector shooting packets of electrons at approximately the speed of light. Then, the electrons pass through a sequence of electromagnetic fields to gain more and more energy. They can be pictured as surfers earning energy by surfing the waves. In the next step, the packets of electrons pass through a bunch compressor—a sort of magnet package—that compresses the length of the electron beam. This process repeats a few times till the outcome is the electron bunches that are shorter and full of energy.

In the second part, the compressed electron bunches pass through a series of magnetic devices, forcing them to follow an undulating path. In the first device, which is called modulator, the electrons meet a laser wave. The spatial modulation of energy in the electron bunch becomes well-defined as a result of the interaction between the electrons and the magnetic field of the laser beam. Subsequently, because of the laser features, the electrons' energy modulation inside the bunch is transformed into a density modulation. Then, using a few magnetic devices, the electrons are concentrated into microbunches (i.e., smaller bunches). Afterward, the new electron microbunches enter the radiator, where their constant deflection from the rectilinear trajectory stimulates the emission of light. At this point, both electrons and the light produced by them proceed in the same direction.

In the third part, the electrons interact with the light, and the electrons arrange themselves into a structure dictated by the wavelength of the light. In other words, it is a kind of resonance effect. This arrangement creates a resonance effect, where the electrons and the light are bound and in sync, leading to an increase in the intensity of the produced light.

By the end of the path, the microbunches of electrons produce extremely intense

pulses of X-ray. Finally, the X-ray pulses will be sent to the experimental hall, where they will collide with the samples to be studied.

2.2.2 Single-pass free-electron laser

A single-pass free-electron laser in the self-amplified spontaneously emission (SASE) mode [147] works by passing an electron beam pulse with a peak current and the total energy E_e through an undulator—a periodic magnetic structure, cf. Fig. 2.2.

The electron beam pulse interacts with the emitted synchrotron radiation in the undulator while most of the power of the emitted synchrotron radiation is concentrated in an opening angle

$$1/\gamma \equiv m_e c^2/E_e = 2 \cdot 10^{-5}(25\ \mathrm{GeV}/E_e) \tag{2.4}$$

where m_e is the electron mass. This interaction causes a longitudinal charge density modulation called microbunching if the resonance condition,

$$\gamma \equiv \frac{\lambda_U}{2\gamma^2}\left(1+\frac{K_U^2}{2}\right) = 0.3(\mathrm{nm})\left(\frac{1/\gamma}{2\cdot 10^{-5}}\right)\left(\frac{1+K_U^2/2}{3/2}\right) \tag{2.5}$$

is met. Here λ and λ_U are, respectively, the emitted radiation's wavelength, and the length of the undulator's magnetic period. The dimensionless quantity K_U is the undulator parameter that gives the ratio of the average deflection angle of the electrons in the undulator magnetic field B_U to the opening cone of the synchrotron radiation

$$K_U \equiv \frac{e\lambda_U B_U}{2\pi m_e c} \tag{2.6}$$

The undulator parameter is typically in the range of $1-3$, but it should be of the order of one on resonance. In the end, the electrons—in the developing microbunches—radiate coherently while the number of emitted photons exponentially increases until saturation is reached. It turns out that in an undulator the radiation power P,

$$P \propto e^2 N_e^2 B_U^2 \gamma^2 \tag{2.7}$$

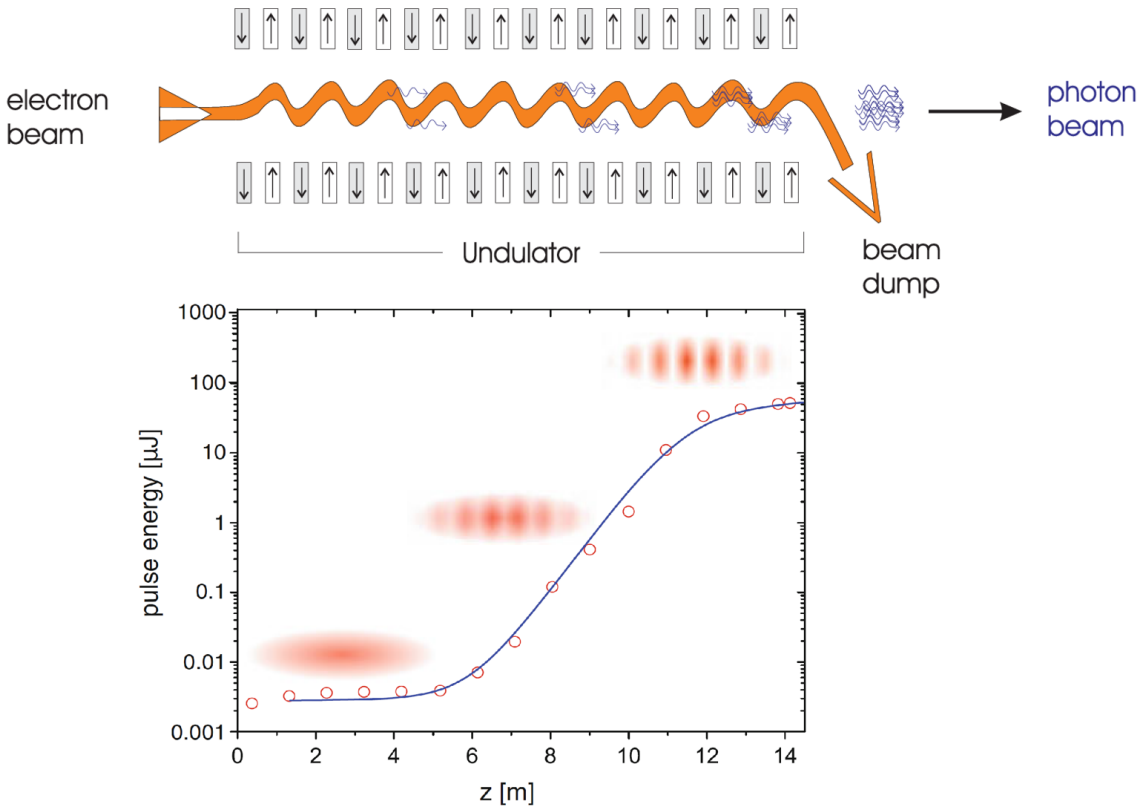

Figure 2.2: The FEL pulse energy exhibits exponential growth with the distance traveled in the undulator, denoted as z. These observations, represented by open circles, were recorded at the SASE FEL of the TESLA test facility, utilizing an electron energy of 245 MeV [177]. The schematic depiction illustrates the evolving microbunching phenomenon. Laser saturation initiates when z surpasses 12 m, indicating the full development of microbunches, with no anticipated further rise in laser power (Ref. [194], Fig. 4.2).

where $N_e \geq 10^9$ is the number of electrons in a bunch, cf. Fig. 2.3.

In 1998, the idea of using a linear accelerator for constructing an XFEL for the Stanford Linear Accelerator was proposed [10], and in 2008 it started to provide the X-ray laser beams. The X-ray pulses produced in LCLS [135] in Stanford and

in the European XFEL facility [29, 143, 144, 1] in Hamburg are far shorter than the pulses from the other X-ray sources. Their peak brilliance is about eight orders of magnitude higher. In Table 2.1, some features of the radiation produced at the TESLA XFEL laboratory are listed. The high pulse energy and the femtosecond duration of the coherent X-ray pulses have opened new fields of research.

Table 2.1: Properties of X-ray FELs at the TESLA XFEL laboratory.

	unit	SASE 1	SASE 5
wavelength	nm	$0.1 - 0.5$	$0.4 - 5.8$
bandwidth (FWHM)	%	0.08	$0.29 - 0.7$
peak power	GW	37	$110 - 200$
average power	W	210	$610 - 1100$
photon beam size (rms)	μm	43	$25 - 38$
peak power density	W/m^2	$6 \cdot 10^{18}$	$6 \cdot 10^{19}$

2.3 Semi-classical production rate estimation

In this section, we discuss the spontaneous pair production at the focus of XFELs. We use a set of assumptions and an approximation for the electromagnetic field of the laser beam. They preserve the general case's leading properties and allow us to find a closed-form solution for the (e^+e^-) pair production rate. For the critical parameters of XFELs, we estimate the order-of-magnitude required to get an observable effect.

It turns out that in a light-like static electromagnetic field characterized by

$$\mathcal{F} \equiv \frac{1}{4} F_{\mu\nu} F^{\mu\nu} \equiv -\frac{1}{2} (\mathbf{E}^2 - c^2 \mathbf{B}^2) = 0 \tag{2.8}$$

$$\mathcal{G} \equiv \frac{1}{4} F_{\mu\nu} \tilde{F}^{\mu\nu} \equiv c\, \mathbf{E} \cdot \mathbf{B} = 0 \tag{2.9}$$

pair production cannot occur [199]. Here $F_{\mu\nu}$ and $\tilde{F}^{\mu\nu}$ are, respectively, the electromagnetic field strength tensor and its dual defined as $\tilde{F}^{\mu\nu} = (1/2)\, \epsilon^{\mu\nu\alpha\beta} F_{\alpha\beta}$. It

has been suggested that laser beam fields, when focused, closely resemble a wrenchless ($\mathbf{E}\cdot\mathbf{B}=0$) light-like field, potentially suppressing pair creation significantly [210]. However, in regions near the focus where $\mathcal{F}<0$, pair production remains possible [31, 120, 27]. In general, in a light-like electromagnetic field, pair production is possible, unless $\mathcal{G}=0$ and $\mathcal{F}=0$ or $\mathcal{G}=0$ and $\mathcal{F}>0$. The latter case corresponds to a pure magnetic field in an appropriate coordinate system [199]. Therefore, one can expect to observe pair creation in a pure uniform electric field oscillating with a frequency ω

$$\mathbf{E}(t)=(0,0,E\cos(\omega t))\,,\qquad \mathbf{B}(t)=(0,0,0)\,, \tag{2.10}$$

as it corresponds to $\mathcal{G}=0$, $\mathcal{F}<0$. Such a field may be created in an antinode of the standing wave [168, 169, 170, 171, 150, 141, 41] formed by a superposition of two coherent laser beams with wavelength

$$\lambda=\frac{2\pi c}{\omega} \tag{2.11}$$

and the created electric field can be assumed uniform at distances far less than the wavelength λ.

To compute the rate of (e^+e^-) pair production in a semi-classical manner, we start with assuming that every pulse of an XFEL is split into two equal parts and recombined to form the standing wave, in regions where the electromagnetic field has the form Eq. (2.10) with a peak electric field given by Eq. (2.3). We also assume that the electric field amplitude E and the laser photon energy $\hbar\omega$ are, respectively, much smaller than the critical field E_c and the rest-mass energy of the electron:

$$E\ll E_c\,,\qquad \hbar\omega\ll m_ec^2. \tag{2.12}$$

These conditions are well satisfied with X-ray lasers (cf. Table 2.2). We use the generalized WKB method [28, 168, 169, 54, 65, 119]. The parameter η,

$$\eta=\frac{\hbar\omega}{eE\lambda}=\frac{\hbar\,\omega}{m_ec^2}\,\frac{E_c}{E}=\frac{m_ec\,\omega}{e\,E}\,, \tag{2.13}$$

Table 2.2: Comparison of Laser Parameters and Derived Quantities for Spontaneous (e^+e^-) Pair Production Estimates.

Laser Parameters				
	Optical	**X-ray FEL**		
	Focus: Diffraction limit	Design	Focus: Available	Focus: Goal
λ	1 μm	0.4 nm	0.4 nm	0.15 nm
$\hbar\omega = hc/\lambda$	1.2 eV	3.1 keV	3.1 keV	8.3 keV
P	1 PW	110 GW	1.1 GW	5 TW
σ	1 μm	26 μm	21 nm	0.15 nm
$\triangle t$	500 fs - 20 ps	0.04 fs	0.04 fs	0.08 ps
Derived Quantities				
$S = P/\pi\sigma^2$	3×10^{26} W/m^2	5×10^{19} W/m^2	8×10^{23} W/m^2	7×10^{31} W/m^2
$E = \sqrt{\mu_0\, c\, S}$	4×10^{14} V/m	1×10^{11} V/m	2×10^{13} V/m	2×10^{17} V/m
E/E_c	3×10^{-4}	1×10^{-7}	1×10^{-5}	0.1
$\hbar\omega/m_e c^2$	2×10^{-6}	0.006	0.006	0.02
$\eta = \hbar\omega/eE\lambda\!\!\!^{-}$	9×10^{-3}	6×10^4	5×10^2	0.1

plays the role of an adiabaticity parameter. The probability of creation of one (e^+e^-) pair per unit time and unit volume,

$$w = \frac{\mathrm{d}\, n_{e^+e^-}}{\mathrm{d}^3x\, \mathrm{d}t} \tag{2.14}$$

depends on the laser frequency only via η, and it can be estimated as follows [177,

172, 167]

$$w \simeq \frac{c}{4\,\pi^3 \lambda\!\!\!^{-4}} \times \tag{2.15}$$

$$\times \begin{cases} (\sqrt{2}/\pi)\,(E/E_c)^{5/2}\,\exp\left[-\pi\ (E/E_c)\left(1-\frac{1}{8}\eta^2+\mathcal{O}(\eta^4)\right)\right]\,, & :\ \ \eta \ll 1\,, \\ \sqrt{\pi/2}\,(\hbar\,\omega/m_e c^2)^{5/2} \times & \\ \qquad \times \sum_{n>2\ m_e c^2/\hbar\omega} (\mathrm{e}/4\eta)^{2n}\ \exp\left[-2\,(n-2\ m_e c^2/\hbar\omega)\right] \times & \\ \qquad\qquad \times \mathrm{Erfi}\left(\sqrt{2\,(n-2\ m_e c^2)}\ \right) & :\ \ \eta \gg 1\,, \end{cases}$$

Here Erfi is the imaginary error function. In the regime characterized by adiabatic strong-field conditions with low frequency ($\omega \ll 1$) and small $\eta \ll 1$, the obtained result is consistent with Schwinger's non-perturbative findings for a spatially uniform static field [199]. In contrast, in the non-adiabatic weak-field regime with high frequency ($\omega \gg 1$) and large η ($\eta \gg 1$), the result is perturbative. This perturbation corresponds to the perturbation order equal to or greater than n, where n represents the minimum number of quanta required to create an (e^+e^-) pair: $n \gtrsim 2, m_e c^2/\hbar\omega \gg 1$.

At this point, it is possible to discuss if the non-perturbative Schwinger pair creation mechanism has already been observed in the SLAC experiment E-144 [147, 32]. This experiment aimed to study positron production in the collision of 46.6 GeV/c electrons with terawatt optical laser pulses ($\lambda = 527\ \mu$m). In the rest frame of the incident electrons, $E \simeq 5 \cdot 10^{17}$ V/m was reached, and the adiabaticity parameter η is therefore in the range $3-10$, cf. Fig. 2.4. It corresponds to the multi-photon regime. Two studies provide convincing evidence for the interpretation of the data as multi-photon light-by-light scattering [32, 13]. The measured production rate of positrons scales as $R_{e^+} \propto \eta^{-10}$, Fig. 2.4. This agrees with Eq. (2.14) where $w \propto \eta^{-2n}$ for $\eta \gg 1$, since n is the number of involving laser photons, and five photons are required to produce a pair near threshold to satisfy the kinematic constraints.

For the strong-field adiabatic regime, using an X-ray laser ($\hbar\omega \simeq 1 - 10$ keV), to satisfy $\eta \lesssim 1$ the amplitude of the electric field should be $E \gtrsim \hbar\omega E_c/\left(m_e c^2\right) \sim 10^{15}-10^{16}$ V/m. From Eq. (2.14) it turns out that to obtain a sizeable pair production rate an electric field of about $0.1E_c \sim 10^{17}$ V/m is required [177]. To produce an electric field amplitude of this order-of-magnitude, a terawatt X-ray beam is needed.

In Table 2.2, the relevant parameters of XFELs are summarized [177]. By considering available power densities and available techniques, it is clear that the electric field strengths are still much smaller than the magnitudes required for a sizeable effect. If the peak power increases to the terawatt region, and if X-ray optics approaches the diffraction limit of focusing, 0.1-nanometer range, there would be ample room to test the Schwinger pair production mechanism at XFELs.

2.4 Summary

Advancements in XFEL technology have brought us closer to experimentally verifying the Schwinger effect, a phenomenon with profound implications for quantum field theories and cosmology. The unique capabilities of XFELs, including their ability to produce intense and short X-ray pulses with high peak brilliance, offer a promising avenue for generating the extreme electric field strengths required for observing the Schwinger effect. By exploiting XFELs' ability to focus X-ray beams to wavelengths comparable to the laser beam's radius, it becomes possible to achieve electric fields stronger than those produced by optical lasers. The semi-classical production rate estimation provides insight into the conditions required for observing the Schwinger effect in XFEL experiments. Despite significant progress, challenges remain, including ensuring precise control over experimental parameters and confirming the observance of pair creation against background noise. More advancements in XFEL technology and experimental techniques hold the promise of shedding further light on the Schwinger effect and its implications for fundamental physics.

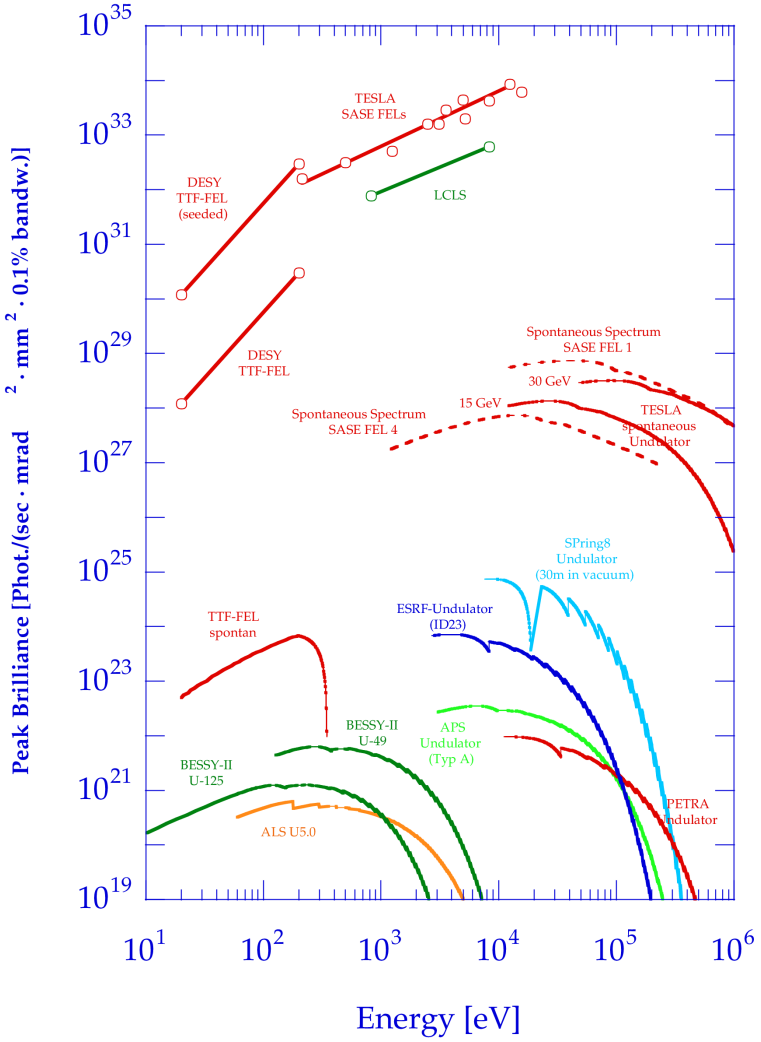

Figure 2.3: Expected peak brilliance of the planned X-ray FELs LCLS and XFEL (Ref. [144, 1], Fig. 6.2). Peak brilliance refers to the anticipated number of X-ray photons emitted per second, per unit area, per unit solid angle, and within a certain bandwidth around the peak wavelength. mrad^2 stands for milliradians squared and refers to the solid angle subtended by the X-ray beam. In the context of free electron lasers, it quantifies the spread or focus of the X-ray beam. "0.1% bandwidth" specifies the width of the wavelength range around the peak wavelength within which the photon count is calculated.

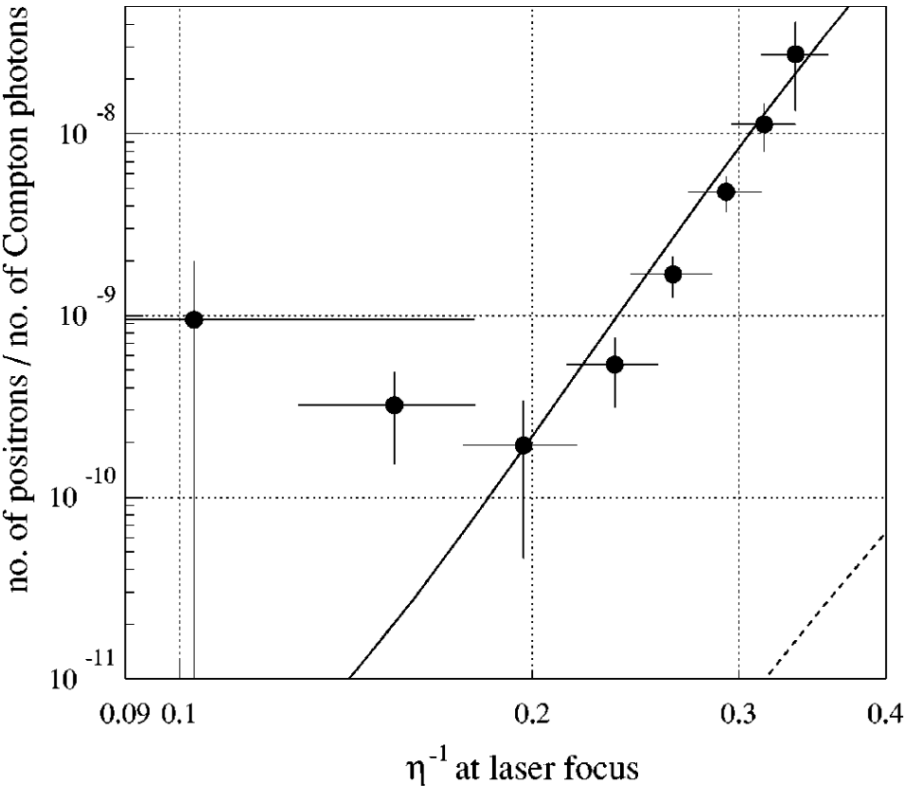

Figure 2.4: The positron rate per laser shot as a function of the inverse of the adiabaticity parameter, η^{-1}. The data were obtained by the SLAC experiment E-144. The line is a power law fit to the data. It gives $R_{e^+} \propto \eta^{-2n}$, with $n = 5.1 \pm 0.2(stat)^{+0.5}_{-0.8}(syst)$ (Ref. [32], Fig. 5).

Chapter 3

The Gauge-Invariant Wilson Loop

The ultimate aim of this chapter is to introduce the Wilson Loop, a gauge-invariant parameter, that is an essential tool to compute the pair production rate in the next chapter. To build up intuitions, we start by reviewing the most common way to introduce QED's local gauge invariance. Although this approach is straightforward, it does not reveal the geometrical origin of the procedure. In the second section, we study the gauge invariance of field theories from a geometrical perspective. In the last section, we show that the geometrical approach canonically leads to introducing the Wilson loops [163].

3.1 Introduction U(1) gauge transformation

We begin by studying the gauge invariance of Dirac Lagrangian

$$\mathcal{L}_{Dirac} = \overline{\psi}(x) i\gamma^{\mu}\partial_{\mu}\psi(x) - m\overline{\psi}(x)\psi(x) \tag{3.1}$$

where $\psi(x)$ is the complex-valued Dirac field, γ^{μ} represents Dirac 4×4 matrices, $\overline{\psi}(x) \equiv \psi^{\dagger}(x)\gamma^{0}$, and m is the Dirac field's mass. Under global U(1) transformation

$$\begin{cases} \psi(x) \rightarrow \psi^{'}(x) = e^{i\alpha}\psi(x) \\ \psi(x) \rightarrow \overline{\psi}^{'}(x) = e^{-i\alpha}\overline{\psi}(x) \end{cases} \tag{3.2}$$

$\mathcal{L}_{Dirac}$ remains invariant

$$\mathcal{L}_{Dirac} \rightarrow \mathcal{L}^{'}_{Dirac} = \mathcal{L}_{Dirac} \tag{3.3}$$

but it changes under local transformation

$$\begin{cases} \psi(x) \rightarrow \psi^{'}(x) = e^{i\alpha(x)}\psi(x) \\ \psi(x) \rightarrow \overline{\psi}^{'}(x) = e^{-i\alpha(x)}\overline{\psi}(x) \end{cases} \tag{3.4}$$

$$\mathcal{L}_{Dirac} \rightarrow \mathcal{L}^{'}_{Dirac} \neq \mathcal{L}_{Dirac} \tag{3.5}$$

By adding terms to the $\mathcal{L}_{Dirac}$, we can make it locally invariant. Substituting the partial derivative with the covariant derivative [1]

$$D_{\mu} \equiv \partial_{\mu} + ieA_{\mu}(x) \tag{3.6}$$

where $e = -|e|$ is the electron charge, and $A_{\mu}(x)$ is the vector potential with the following U(1) transformation rule

$$A_{\mu}(x) \rightarrow A^{'}_{\mu} = A_{\mu}(x) - \frac{1}{e}\left(\partial_{\mu}\alpha(x)\right) \tag{3.7}$$

the new Lagrangian equals

$$\begin{aligned} \mathcal{L}_{new} &= \overline{\psi}(x)i\gamma^{\mu}\big(\partial_{\mu} + ieA_{\mu}(x)\big)\psi(x) - m\overline{\psi}(x)\psi(x) \\ &= \overline{\psi}(x)i\gamma^{\mu}\partial_{\mu}\psi(x) - e\overline{\psi}(x)\gamma^{\mu}A_{\mu}(x)\psi(x) - m\overline{\psi}(x)\psi(x) \end{aligned} \tag{3.8}$$

[1] One may tend to think that the idea is borrowed from classical physics. The momentum p of an electron in the presence of an electromagnetic field equals $\mathcal{P} - eA$, where $\mathcal{P}$ is the canonical momentum vector [174, 71].

that is locally gauge invariant

$$\mathcal{L}_{new} \rightarrow \mathcal{L}'_{new} = \mathcal{L}_{new} \tag{3.9}$$

Finally, to write the most general locally invariant Lagrangian called $\mathcal{L}_{QED}$, it is essential to add pure gauge-invariant terms like $F_{\mu\nu}(x)F^{\mu\nu}(x)$, where

$$F_{\mu\nu}(x) \equiv \partial_\mu A_\nu(x) - \partial_\nu A_\mu(x) \tag{3.10}$$

is called field strength tensor. Hence, we have

$$\mathcal{L}_{QED} = \overline{\psi}(x)i\gamma^\mu\partial_\mu\psi(x) - e\overline{\psi}(x)\gamma^\mu A_\mu(x)\psi(x) - \frac{1}{4}F_{\mu\nu}(x)F^{\mu\nu}(x) - m\overline{\psi}(x)\psi(x) \tag{3.11}$$

3.2 The geometry of gauge invariance

3.2.1 Covariant derivative

Assuming that local gauge invariance is a fundamental principle, it is possible to employ this principle to construct gauge-invariant filed theories. We start to construct a filed theory with the complex-valued Dirac field $\psi(x)$. It is expected that the field theory be locally U(1) gauge-invariant. The mass term $m\overline{\psi}(x)\psi(x)$ is pure gauge-invariant, but terms including combinations of $\overline{\psi}(x)$ and $\partial_\mu\psi(x)$ are not.

Noting the definition of the $\partial_\mu\psi(x)$ in the direction n^μ:

$$n^\mu\partial_\mu\psi(x) \equiv \lim_{\epsilon\to 0}\frac{1}{\epsilon}\big[\psi(x+\epsilon n) - \psi(x)\big], \tag{3.12}$$

it is clear [2] that the transformation of $\partial_\mu\psi(x)$ depends on both the transformation of $\psi(x)$ and the transformation of $\psi(x+\epsilon n)$. If we define a new derivative $D_\mu\psi(x)$ whose transformation law looks like the transformation of $\psi(x) \rightarrow e^{i\alpha(x)}\psi(x)$ and use it to substitute for $\partial_\mu\psi(x)$, the term including the $D_\mu\psi(x)$ and $\overline{\psi}(x)$ will be locally gauge-invariant.

To construct such a derivative, we need to employ a factor $\mathcal{u}(y,x)$ called comparator that compensates for the difference in phase transformations from one point to the next. We introduce the comparator as a pure phase $e^{i\phi(y,x)}$ with the following properties:

$$\mathcal{u}(y,x) \equiv e^{i\phi(y,x)} \tag{3.13}$$

$$\mathcal{u}(x,x) = 1 \tag{3.14}$$

$$\mathcal{u}^{\dagger}(y,x) = \mathcal{u}(x,y) \tag{3.15}$$

$$\mathcal{u}^{\dagger}(y,x) \to e^{i\alpha(y)}\mathcal{u}(y,x)e^{-i\alpha(x)}. \tag{3.16}$$

With this transformation law for the comparator, $\psi(x+\epsilon n)$ and $\mathcal{u}(x+\epsilon n)\psi(x)$ have the same transformation law rule

$$\psi(x+\epsilon n) \to e^{i\alpha(x+\epsilon n)}\psi(x+\epsilon n) \tag{3.17}$$

$$\mathcal{u}(x+\epsilon n)\psi(x) \to e^{i\alpha(x+\epsilon n)}\mathcal{u}(x+\epsilon n)\psi(x), \tag{3.18}$$

that is precisely what we require to define the $D_\mu\psi(x)$ called covariant derivative as follows:

$$n^\mu D_\mu\psi(x) \equiv \lim_{\epsilon\to 0}\frac{1}{\epsilon}\big[\psi(x+\epsilon n) - \mathcal{u}(x+\epsilon n)\psi(x)\big]. \tag{3.19}$$

Using Eq. (3.17), Eq. (3.18) and Eq. (3.19), the transformation law for the covariant derivative is

$$D_\mu\psi(x) \to e^{i\alpha(x)}D_\mu\psi(x) \tag{3.20}$$

To find the explicit form of the covariant derivative, we need to use the expansion of $\mathcal{u}(x+\epsilon n)$ for infinitesimally separated points

$$\begin{aligned}\mathcal{u}(x+\epsilon n) &= \mathcal{u}(x,x) + \epsilon n^\mu\big[\partial_\mu\mathcal{u}(x,x)\big] + \mathcal{O}(\epsilon^2)\\ &= 1 - ie\epsilon n^\mu A_\mu(x) + \mathcal{O}(\epsilon^2);\ \big[\partial_\mu\mathcal{u}(x,x) \equiv -ieA_\mu(x)\big]\end{aligned} \tag{3.21}$$

[2]Noting the transformation law for $\psi(x)$, given by Eq. (3.4), it is trivial that under local U(1) transformation. $n^\mu\partial_\mu\psi(x) \to e^{i\alpha(x)}n^\mu\Big\{\partial_\mu + i\big[\partial_\mu\alpha(x)\big]\Big\}\psi(x)$

where e is an arbitrary constant, and A_μ represents a new vector filed called connection. Then, using Eq. (3.19) and Eq. (3.21), D_μ takes the form

$$D_\mu = \partial_\mu + ieA_\mu(x) \tag{3.22}$$

Moreover, using Eq. (3.16) and Eq. (3.21), the transformation law for $A_\mu(x)$ can be found as

$$A_\mu(x) \to A_\mu(x) - \frac{1}{e}\big(\partial_\mu \alpha(x)\big) \tag{3.23}$$

Accordingly, the following Lagrangian

$$\begin{aligned} \mathcal{L}_{QED} &= \overline{\psi}(x) i\gamma^\mu D_\mu \psi(x) - m\overline{\psi}(x)\psi(x) \\ &= \overline{\psi}(x) i\gamma^\mu \big[\partial_\mu + ieA_\mu(x)\big]\psi(x) - m\overline{\psi}(x)\psi(x) \\ &= \overline{\psi}(x) i\gamma^\mu \partial_\mu \psi(x) - m\overline{\psi}(x)\psi(x) - e\overline{\psi}(x) i\gamma^\mu A_\mu \psi(x) \end{aligned} \tag{3.24}$$

is invariant under local U(1) gauge transformation.

3.2.2 Kinetic term of $A_\mu(x)$

It should be noticed that structures like the connection mass term $A_\mu(x)A^\mu(x)$ are not locally invariant due to Eq. (3.22). As a result, to find the most general locally U(1) gauge invariant Lagrangian, we need to construct the kinetic term for $A_\mu(x)$. For this purpose, there are two approaches: 1) using the comparator, and 2) using the covariant derivative.

3.2.2.1 The first approach

For the first approach, we consider an imaginary infinitesimal square in (1,2)-plane, as defined by the unit vectors $\hat{1}$ and $\hat{2}$ in spacetime, cf. Fig. (3.1). Defining $W(x)$ as follows, we link together comparisons around the square.

$$W(x) \equiv u(x, x+\epsilon\hat{2})u(x+\epsilon\hat{2}, x+\epsilon\hat{1}+\epsilon\hat{2})u(x+\epsilon\hat{1}+\epsilon\hat{2}, x+\epsilon\hat{1})u(x+\epsilon\hat{1}, x) \tag{3.25}$$

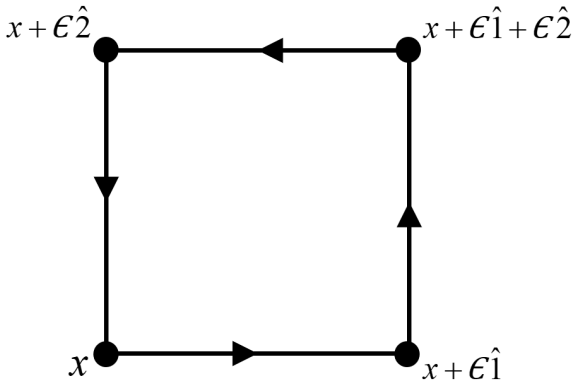

Figure 3.1: An imaginary infinitesimal square in (1,2)-plane.

The transformation law for the comparator, Eq. (3.16), indicates that $W(x)$ is locally invariant. In the limit $\epsilon \to 0$, $W(x)$ will therefore give a locally invariant function of $A_\mu(x)$. To expand $W(x)$, we use Eq. (3.15) and the following expansion for comparisons and connections:

$$w(x+\epsilon\hat{n},x) = \exp\big[-i\,e\,\epsilon\,n^\mu A_\mu(x+\frac{\epsilon}{2}\hat{n}) + \mathcal{O}(\epsilon^3)\big] \tag{3.26}$$

$$A_\mu(x+\epsilon\hat{n}) = A_\mu(x) + \epsilon\,n^\nu\partial_\nu A_\mu(x) + \mathcal{O}(\epsilon^2) \tag{3.27}$$

Consequently,

$$\begin{aligned}
W(x) &= w^\dagger(x+\epsilon\hat{2},x)w^\dagger(x+\epsilon\hat{1}+\epsilon\hat{2},x+\epsilon\hat{2})w(x+\epsilon\hat{1}+\epsilon\hat{2},x+\epsilon\hat{1})w(x+\epsilon\hat{1},x)\\
&= exp\Big\{-ie\epsilon\big[-A_2(x+\frac{\epsilon}{2}\hat{2}) - A_1(x+\frac{\epsilon}{2}\hat{1}+\epsilon\hat{2})\\
&\qquad\qquad + A_2(x+\epsilon\hat{1}+\frac{\epsilon}{2}\hat{2}) + A_1(x+\frac{\epsilon}{2}\hat{1})\big] + \mathcal{O}(\epsilon^3)\Big\}\\
&= \exp\Big\{-i\,e\,\epsilon^2\big[\partial_1 A_2(x) - \partial_2 A_1(x)\big] + \mathcal{O}(\epsilon^3)\Big\}\\
&= \exp\big\{-i\,e\,\epsilon^2 F_{12}(x) + \mathcal{O}(\epsilon^3)\big\}\\
&= 1 - i\,e\,\epsilon^2 F_{12}(x) + \mathcal{O}(\epsilon^3)
\end{aligned} \tag{3.28}$$

This reveals that $F_{\mu\nu} \equiv \partial_\mu A_\nu(x) - \partial\nu A_\mu(x)$ is locally invariant [3].

$$F_{\mu\nu}(x) \to F^{'}_{\mu\nu}(x) = F_{\mu\nu}(x) \tag{3.29}$$

Therefore, any function of $A_\mu(x)$ is locally invariant only through $F_{\mu\nu}(x)$ and its derivatives.

3.2.2.2 The second approach

Working from the covariant derivative, because of Eq. (3.4) and Eq. (3.20), it is clear that

$$D_\mu D_\nu \psi(x) \to e^{i\alpha(x)} D_\mu D_\nu \psi(x) \tag{3.30}$$

so the transformation law for the commutator of covariant derivatives is

$$[D_\mu, D_\nu]\psi(x) \to e^{i\alpha(x)}[D_\mu, D_\nu]\psi(x) \tag{3.31}$$

In Eq. (3.31), $\psi(x)$ accounts for the entire local transformation; therefore, $[D_\mu, D_\nu]$ must be locally invariant. It is interesting that the commutator $[D_\mu, D_\nu]$ is not itself a derivative at all, since

$$\begin{aligned}
[D_\mu, D_\nu]\psi(x) &= [\partial_\mu + ieA_\mu(x), \partial_\nu + ieA_\nu(x)]\psi(x) \\
&= [\partial_\mu, \partial_\nu]\psi(x) + ie\Big\{\big[\partial_\mu, A_\nu(x)\big] - \big[\partial_\nu, A_\mu(x)\big]\Big\}\psi(x) \\
&\qquad + \big[A_\mu, A_\nu(x)\big]\psi(x) \\
&= ieF_{\mu\nu}(x)\psi(x)
\end{aligned} \tag{3.32}$$

Eq. (3.32) indicates that

$$[D_\mu, D_\nu] = ieF_{\mu\nu}(x) \tag{3.33}$$

and, as a result, $F_{\mu\nu}(x)$ is locally invariant. To see the equivalence of the two approaches, we can visualize the commutator of covariant derivatives as the comparison of comparisons around the four corners of an infinitesimal square lied in (μ, ν)-plane, cf. Fig. (3.2).

[3] The invariance of this structure can be checked directly by using Eq. (3.23).

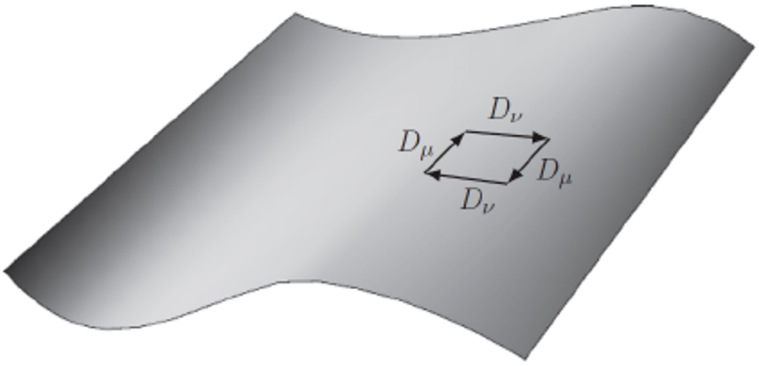

Figure 3.2: A closed path in (μ, ν)-plane.

3.2.3 Writing the most general locally invariant Lagrangian

Using the ingredients assembled in 2.1 and 2.2, we can write the most general locally invariant Lagrangian for the electron field $\psi(x)$ and its associated connection $A_\mu(x)$. In 4 dimensions,

$$\mathcal{L}_4 = \overline{\psi}(x) i\gamma^\mu D_\mu \psi(x) - \frac{1}{4} F_{\mu\nu}(x) F^{\mu\nu}(x) - c \ \in^{\alpha\beta\mu\nu} F_{\alpha\beta}(x) F_{\mu\nu}(x) - m\overline{\psi}(x)\psi(x) \quad (3.34)$$

where $\in^{\alpha\beta\mu\nu}$ is the Levi-Civita symbol. The third term violates the discrete symmetries parity P and time reversal T. Hence, if we postulate these symmetries, then we must exclude the third term, and we end up with $\mathcal{L}_{QED}$.

It should be noticed that, from the discussed geometrical point of view, all the achieved results in this section are direct consequences of the symmetry principle.

3.2.4 The Wilson loop

In 2.2.1, we defined $W(x)$ as the multiplication of four comparisons corresponding to the four corners of an infinitesimal square. Moreover, we showed that $W(x)$ is different than 1. The difference is proportional to the surface of the closed path. Inspired by Eq. (3.21) and Eq. (3.26), it seems canonical to define comparator for an

arbitrary path P that runs from x to y as

$$u_P(y,x) \equiv \exp\left[-ie \int_P dz^\mu A_\mu(z) \right] \tag{3.35}$$

where $u_P(y,x)$ is called the Wilson line. It is clear that Eq. (3.35) and Eqs. (3.13) to (3.16) agree. We check the transformation law as follows:

$$\begin{aligned} u_P(y,x) \to u'_P(y,x) &= \exp\left[-ie \int_P dz^\mu A'_\mu(z) \right] \\ &= \exp\left\{ -ie \int_P dz^\mu \left[A_\mu(z) - \frac{1}{e}\partial_\mu \alpha(z) \right] \right\} \\ &= \exp\left\{ -ie \int_P dz^\mu A_\mu(z) - i\alpha(y) + i\alpha(x) \right\} \\ &= e^{i\alpha(x)} u_P(y,x) e^{-i\alpha(y)} \end{aligned} \tag{3.36}$$

Accordingly, if P is a closed path like the path shown in Fig. (3.3), we have

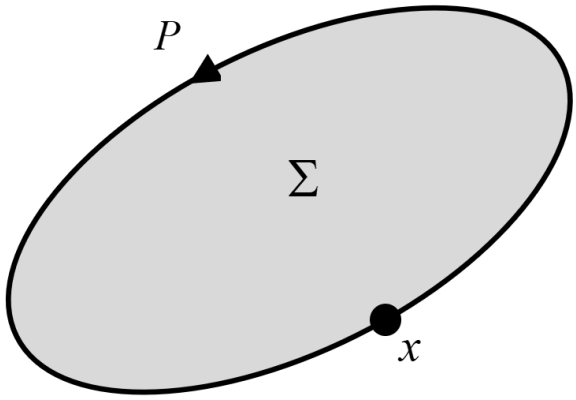

Figure 3.3: The surface that spans the closed loop P.

$$u_P(x,x) \equiv \exp\left[-ie \oint_P dz^\mu A_\mu(z) \right] \tag{3.37}$$

called the Wilson loop. Using the Stoke's theorem, the Wilson loop equals

$$\begin{aligned} u_P(x,x) &= \exp\left[-ie \oint_P dz^\mu A_\mu(z) \right] \\ &= \exp\left[-i\frac{e}{2} \int_\Sigma d\sigma^{\mu\nu} F_{\mu\nu}(z) \right] \end{aligned} \tag{3.38}$$

where $d\sigma^{\mu\nu}$ is an antisymmetric area element on the surface Σ that spans the closed-loop P.

It is crucial to emphasize that the Wilson loop is locally gauge-invariant. More importantly, all gauge-invariant functions of $A_\mu(x)$ can be thought of as combinations of Wilson loops for different path P choices.

Chapter 4

Using Ads/QCD to unveil Quark Confinement

In the present chapter, we thoroughly investigate the response of a QCD-like gauge theory, holographically dual to a deformed AdS_5 model, to a static electromagnetic field. The calculations are performed for three different cases, i.e., with only a quadratic correction, with only a logarithmic correction, and with both quadratic and logarithmic corrections, for which the parameters are chosen as the ones found in [90] by fitting to experimental and lattice results.

The critical electric fields of the system are found by analyzing its total potential. Comparing the total potential for the three cases, we observe that the quarks can be liberated easier in quadratic and then logarithmic case, for a given electric field. Then, by calculating the expectation value of a circular Wilson loop, the pair production rate is evaluated while a static electric field and a static magnetic field are simultaneously present. The aforementioned result obtained from the potential analysis is also confirmed here when no magnetic fields are present.

This chapter contains text from an article published in Physical Review D (Masoumi et al. 2020 [142]).

We moreover find that the presence of a magnetic field perpendicular to the direction of the electric field suppresses the rate of producing the quark pairs and accordingly increases the critical electric field below which the Schwinger effect does not occur. Interestingly, the presence of a parallel magnetic field alone does not change the response of the system to the external electric field, although it enhances the creation rate when a perpendicular magnetic field is also present.

4.1 Introduction

It is well known that the vacuum in quantum field theory (QFT) can be affected by external fields such as electromagnetic fields; virtual charged particle pairs become real if the external fields are strong enough. Such a phenomenon is referred to as the Schwinger effect [199]. Among other effects leading to the production of particles in high energy physics, such as the Hawking radiation from a black hole and the creation of particles in an expanding universe, the Schwinger effect is one of the most exciting ones due to its importance in understanding various aspects of QFTs.

The result that the dependence of the production rate of particles under the effect of a constant electric field is nonanalytic, shows its nonperturbative nature which motivates us to use it for exploring the nonperturbative regime of QFTs. This phenomenon can also provide an experimental tool for the verification of the results in the nonperturbative regime which has not been explored in a deep manner.

Although the Schwinger effect has not been observed directly yet by experiments, due to the very high intensity of the electric field, about $1.32 \times 10^{18}\ V\ m^{-1}$, needed for this effect to be detectable, new advances in laser technology have provided a promising ground to reach high-intensity electric fields and test the results of this phenomenon [183, 211].

The Schwinger effect was first investigated at the weak coupling (in fact eliminating the Coloumb interaction) and weak field approximation [199] and later gen-

eralized to the arbitrary coupling but weak field case[2]. Despite this effect has been first addressed in the context of quantum electrodynamics (QED), where the electron-positron pairs are created as a response to the electric field, it is also relevant to other QFTs, such as QCD. Quark-antiquark pairs can be produced in the presence of electromagnetic fields, since they also have electric charges. However, in this case, for the quark-antiquark pairs to be created, the electric force must overcome the confining force acting between the quarks.

Investigating this process, beside the fact that this is a realistic phenomenon and thus worth-noticing by itself, can be helpful in shedding light on the mysterious but not-yet discovered quark confinement. One of the most important places that strong electromagnetic fields show up experimentally is in heavy-ion collisions, e.g., in RHIC and LHC, due to the highly accelerated charged particles [116, 216, 50, 203]. In such strong electromagnetic fields, quark-antiquark pairs may be produced as well as electron-positron pairs.

Due to the nonperturbative nature of the Schwinger effect, it cannot be studied using the standard perturbation theory. The AdS/CFT correspondence or generally gauge/gravity duality [84, 220, 140, 38] provides a powerful framework to analyze this effect especially in the confining backgrounds such as QCD-like theories. Following the work of Semenoff and Zarembo [200], in which they proposed a holographic setup to investigate the Schwinger pair production rate in QED-like theories, a vast number of research has been done to explore the various aspects of this phenomenon in different systems with gravity duals including confining ones [186, 187, 184, 26, 185, 111, 64, 69, 224, 112, 202].

AdS/QCD tries to construct a five-dimensional gravity theory in such a way that its dual field theory gains the known properties of the real QCD as much as possible. Using this phenomenological approach, people employed some backgrounds which are reduced to the standard AdS in the UV but are different from it in the IR in such a way that the geometry is terminated at a finite value in the holographic radial

direction.

The existence of the IR wall is crucial to model the confinement in any bottom-up holographic theory. Such backgrounds that are shown to model experimental data or lattice results surprisingly well, can be simply constructed by slightly deformed AdS_5 metrics. It has been shown that these backgrounds have some important features in common with the QCD. Most of them lead to the asymptotic linearity of Regge trajectories and a remarkable similarity to the Cornell potential for heavy-quarks, by fitting a small set of free parameters.

In [90], they employed such a background with a deformation function containing a quadratic and a logarithmic term with three free parameters. They investigated the heavy-quark potential along with the dilaton field and dilation potential found from the Einstein equation and also examined the corresponding beta function for three cases: with only a quadratic correction, with only a logarithmic correction, and with both quadratic and logarithmic corrections.

The models with a negative and positive quadratic term known, respectively, as the soft wall [109] and Andreev-Zakharov [7, 8] model, have produced the properties related to the linear confinement including the linear Regge behavior of mesons in the former model and the linear Regge behavior along with the heavy-quark potential similar to the Cornell potential in the latter model. Various aspects of the latter model have been considered in many other articles [9, 49, 4]. Using their investigations, the authors of [90] found the best values for the parameters of the model by the best-fitted heavy-quark potential and other quantities mentioned above, in any of the three cases and in general they found the theory with only logarithmic correction to be fitted better than other theories.

Although a large number of papers have investigated different aspects of the Schwinger effect in different systems including confined ones, many other aspects are yet to be known, especially the ones regarding the effect of the simultaneous presence of electric and magnetic fields. In this regard, our plan is to consider the response of

the same theory as the one in [90] to an external electromagnetic field.

Since the theory is confining and has an IR cutoff which is a generic feature of confining theories, we expect the existence of two critical electric fields, usually denoted by E_s and E_c. Below E_s, the Schwinger effect does not happen at all. For electric fields between E_s and E_c the pairs are produced with an exponential suppression. Above E_c the pairs are produced freely and catastrophically and the vacuum of the theory is completely unstable. The organization of the paper is as follows.

In the next section, we set the basic framework in which we are working. Then, the total potential of quarks in the presence of an external electric field is evaluated in Sec. 3, and the radius of the IR wall in the three cases of our interest along with their critical electric fields are also calculated. Section 4 is devoted to the calculation and analysis of the pair production rate by extremizing the world-sheet action of a string ending on the boundary of a circular Wilson loop located on a probe D3-brane in the bulk, and equipped with a constant electric and magnetic field. In section 4, we concentrate mainly on the response of the system to the magnetic fields imposed in different directions. We finally summarize our results in Sec. 5.

4.2 The deformed AdS_5 model

We shall begin by introducing the following Euclidean background metric:

$$ds_5^2 = G^s_{mn} dX^m dX^n = e^{2A_s(z)} \left(dt^2 + d\vec{x}^2 + dz^2\right), \tag{4.1}$$

where G^s_{mn} denotes the metric in the string frame. The radial direction is denoted by z and the boundary is located at $z = 0$. To break the conformal symmetry and find QCD-like models in the dual gauge theory side, a deformed warp factor has been added to the pure AdS_5. We define the deformation function $h(z)$ using $e^{2A_s(z)} = \frac{h(z)L^2}{z^2}$, in which L is the AdS_5 radius. $h(z) = 1$ gives the Euclidean pure

AdS_5 metric. Following [90] we choose the deformation function in the form of

$$h(z) = \exp\left[\frac{\sigma z^2}{2} + \lambda \ln\left(\frac{z_{IR} - z}{z_{IR}}\right)\right], \tag{4.2}$$

with three free parameters. σ and λ can be either positive or negative and $z_{IR} > 0$. If $\lambda = 0$, the positive and negative values of the parameter σ correspond to the Andreev-Zakharov model [7, 8] and soft-wall model [109], respectively.

In what follows, we want to examine the effect of a static external electric field on this background for three cases; with only the quadratic function, with only the logarithmic term, and with both quadratic and logarithmic terms.

4.3 Studying the Schwinger effect using the total potential

This section is devoted to the analysis of the total potential of a quark-antiquark pair influencing by a constant external electric field E, in the background of our interest.

We know that the potential of a quark-antiquark pair of infinite masses is evaluated from the Wilson loop of a rectangle C with one direction along the time direction T and the other along the separation direction of the two quarks. For infinite T the expectation value of the Wilson loop gives the interaction potential of the heavy quark-antiquark pair. Holographically, this can be found by calculating the on-shell Nambo-Goto (NG) action of an open string hanging down from the boundary with its endpoints separated by a distance x in, say, x_1 direction of the field theory. Since the creation of infinitely heavy quark particles is severely suppressed, to study the Schwinger effect, we should assume quarks of finite mass. To that purpose, following Semenoff and Zarembo's proposal [200], we put a probe D3-brane at an intermediate position z_0 in the radial direction and attach the endpoints of the string to this brane.

Parametrizing the bulk coordinates as $(t=\eta_0,\ x_1=\eta_1,\ x_2=x_3=0,\ z=z(\eta_1))$ and obtaining the induced metric on the string world-sheet, the string action is given by

$$S_{\rm NG}=\frac{1}{2\pi\sigma_s}\int d\eta_0 d\eta_1 e^{2A_s(z)}\sqrt{1+z'^2}=\frac{T}{2\pi\sigma_s}\int_{-x/2}^{x/2}dx_1 e^{2A_s(z)}\sqrt{1+z'^2}, \tag{4.3}$$

where σ_s is proportional to the inverse of the string tension with a dimension of GeV^{-2}. The conserved quantity is found to be $\frac{e^{2A_s(z)}}{\sqrt{1+z'^2}}=e^{2A_s(z_c)}$, where the right-hand side has been determined by the use of the conditions $z(0)=z_c$ and $z'(0)=0$. By virtue of this relation and then substituting it into Eq. (4.3), the distance between the pair of quarks and their potential energy are derived respectively as follows:

$$x=2z_0a\int_{1/a}^{1}dv\frac{v^2\frac{h(z_0a)}{h(z_0av)}}{\sqrt{1-v^4\left(\frac{h(z_0a)}{h(z_0av)}\right)^2}}, \tag{4.4}$$

$$V_{Q\bar{Q}}=\frac{L^2}{\pi\sigma_s z_0 a}\int_{1/a}^{1}dv\frac{h(z_0av)}{v^2\sqrt{1-v^4\left(\frac{h(z_0a)}{h(z_0av)}\right)^2}}, \tag{4.5}$$

in which we have defined the rescaled dimensionless quantities $v\equiv z/z_c$ and $a\equiv z_c/z_0$. The relation (4.5) contains both the static (mass) and potential energy of the quark-antiquark pair. To obtain the total energy in the presence of an external electric field E, we need to add the potential associated with E, which leads to

$$V_{\rm tot}(x)=\frac{L^2}{\pi\sigma_s z_0 a}\int_{1/a}^{1}dv\frac{h(z_0av)}{v^2\sqrt{1-v^4\left(\frac{h(z_0a)}{h(z_0av)}\right)^2}}-Ex, \tag{4.6}$$

where x is the separation length of the quarks given in Eq. (4.4).

4.3.1 IR cutoff of the deformed AdS_5

In almost all holographic confining gauge theories, there exists a wall cutting off the AdS space in the IR region, realizing the linear confinement. One of the first

efforts in this direction was led to the hard wall model [165]. In the theories we are considering here also there is an IR cutoff z_h in the gravity side, i.e., the radial coordinate z is only allowed in the interval $z_0 \leqslant z < z_h$, where z_0 is the position of the probe D3-brane.

The value of z_h can be simply found by imposing the reality condition of the integral in Eq. (4.4) giving the separation length between the quarks in the dual gauge theory. In fact this condition should be satisfied in order for the chosen geometry could be the holographic dual of the gauge theory. Using a similar argument presented in [8] for the case of the positive quadratic function (the Andreev-Zakharov model), one can simply obtain the maximum value of the radial position z that the tip of a string hung from the boundary (or the D3-brane) can reach, which is equal to the IR cutoff of the gravity theory.

A brief explanation of the process of obtaining z_h is presented here. We suppose that the probe D3-brane is absent for a moment to make the argument simpler without changing the result. This is equivalent to $z_0 = 0$ in our calculations. To ensure that the integrand in this equation is real in the whole integral range $0 \leqslant v \leqslant 1$, the function $f(v) \equiv 1 - v^4 \left(\frac{h(z_c)}{h(z_c v)}\right)^2$ in the denominator should be positive for the whole v-interval, where we have used the replacement $z_c = z_0 a$. A simple analysis shows that in all three cases of our interest this function is equal to one at the beginning of the integral range, $v = 0$, it is zero at $v = 1$, and tends to one again as $v \to +\infty$. One concludes immediately that this function has at least one minimum at which $f(v) \leqslant 0$. To ensure the positivity of the function $f(v)$ for the whole integral range $0 \leqslant v \leqslant 1$, we demand this minimum happens at $v_{\min} \geqslant 1$. When $v_{\min} = 1$, the integral develops a logarithmic singularity and for $v_{\min} > 1$, it is definitely real. By the use of the condition $v_{\min} \geqslant 1$, we find a constraint on the permitted values of z_c in terms of the parameters of the theory as $z_c \leqslant z_h$.

Here we report the results, found by this calculation, for the three cases of our

interest. In the quadratic case where $\lambda = 0$, the function $f(v)$ can be written as

$$f(v) = 1 - v^4 e^{\sigma z_c^2 \left(1 - v^2\right)}.$$

The only extremum of this function found with the aid of the condition $\frac{df(v)}{dv} = 0$ is obtained as $v_{\min} = \sqrt{\frac{2}{\sigma z_c^2}}$. Then from $v_{\min} \geqslant 1$, we obtain $z_c \leqslant \sqrt{\frac{2}{\sigma}}$ meaning that $z_h = \sqrt{\frac{2}{\sigma}}$. For the logarithmic case, i.e., $\sigma = 0$, we can write

$$f(v) = 1 - v^4 e^{-2\lambda \log \frac{z_{IR} - z_c v}{z_{IR} - z_c}} = 1 - v^4 \left(\frac{z_{IR} - z_c v}{z_{IR} - z_c}\right)^{-2\lambda},$$

and following the above mentioned procedure we simply find $z_h = \frac{2 z_{IR}}{2 - \lambda}$. And, for the last case where both the quadratic and logarithmic terms are present the function $f(v)$ can be written as follows

$$f(v) = 1 - v^4 \exp\left[\sigma z_c^2 \left(1 - v^2\right) - 2\lambda \log \frac{z_{IR} - z_c v}{z_{IR} - z_c}\right].$$

This function has only one real extremum from which we can again obtain the IR cutoff in terms of the parameters of the theory. In this case from the condition $\frac{df(v)}{dv} = 0$, we arrive at the algebraic equation $\sigma z_c^3 v^3 - \sigma z_{IR} z_c^2 v^2 + (\lambda - 2) z_c v + 2 z_{IR} = 0$. Using the condition $v_{\min} \geqslant 1$ in which $v_{\min}$ is the real root of this algebraic equation, one finds the value of z_h in terms of the parameters of the theory.

Notice that $a = \frac{z_c}{z_0}$ which is the rescaled radial value of the tip of the string in the bulk cannot be larger than $\frac{z_h}{z_0}$. In fact, at the maximum value of z_c, i.e., z_h a logarithmic singularity is developed in the integral of Eq. (4.4) and the effective string tension reaches its minimum. Also, the integral becomes complex for $z_c > z_h$.

4.3.2 Critical electric fields

According to the previous studies, for every confining field theory, there are two values of electric fields at which the response of the theory alters critically. One of them, usually represented as E_s and restricted to confined theories, is the threshold

value of the electric field required for liberating the lightest quarks and starting the Schwinger effect. The other critical electric field, usually denoted as E_c, is the one above which there is no potential barrier and the vacuum is completely unstable. The existence of E_c is common in deconfined as well as confined phases. For $E_s < E < E_c$ the quarks are faced with a finite potential barrier and they can be liberated only through a tunneling process.

In this section, we search for the critical electric fields in the confined theories of our interest. As mentioned above, E_c is the electric field at which the total potential barrier vanishes completely or equivalently $\lim_{x\to 0} \frac{dV_{\rm tot}}{dx} = 0$. To obtain the derivative of the total potential with respect to x, we can use the chain rule for the first term in Eq. (4.6) as $\frac{dV_{Q\bar{Q}}}{dx} = \frac{dV_{Q\bar{Q}}}{da}/\frac{dx}{da}$. From Eq. (4.4), it can be seen that $x \to 0$ is equivalent to $a \to 1$, where a is related to the maximum radial value of the string. The derivatives are obtained as

$$\begin{aligned}\frac{dV_{Q\bar{Q}}}{da} =& \frac{-L^2}{\pi\sigma_s a^2 z_0}\int_{1/a}^{1} dv \frac{h(z_0 a v)}{v^2\sqrt{1-v^4\left(\frac{h(z_0 a)}{h(z_0 a v)}\right)^2}} + \frac{L^2}{\pi\sigma_s a z_0}\int_{1/a}^{1} dv \frac{\partial}{\partial a}\frac{h(z_0 a v)}{v^2\sqrt{1-v^4\left(\frac{h(z_0 a)}{h(z_0 a v)}\right)^2}} \\ &+ \frac{L^2}{\pi\sigma_s a z_0}\frac{h(z_0)}{\sqrt{1-\frac{1}{a^4}\left(\frac{h(z_0 a)}{h(z_0)}\right)^2}}, \end{aligned} \tag{4.7}$$

$$\begin{aligned}\frac{dx}{da} =& 2z_0\int_{1/a}^{1} dv \frac{v^2\frac{h(z_0 a)}{h(z_0 a v)}}{\sqrt{1-v^4\left(\frac{h(z_0 a)}{h(z_0 a v)}\right)^2}} + 2a z_0\int_{1/a}^{1} dv \frac{\partial}{\partial a}\frac{v^2\frac{h(z_0 a)}{h(z_0 a v)}}{\sqrt{1-v^4\left(\frac{h(z_0 a)}{h(z_0 a v)}\right)^2}} \\ &+ 2a z_0\frac{\frac{h(z_0 a)}{h(z_0)}}{\sqrt{1-\frac{1}{a^4}\left(\frac{h(z_0 a)}{h(z_0)}\right)^2}}. \end{aligned} \tag{4.8}$$

All the integrals in both Eqs. (4.7) and (4.8) vanish in the limit $a \to 1$. Thus, we simply have

$$\frac{dV_{Q\bar{Q}}}{dx} = \frac{L^2}{2\pi\sigma_s a^2 z_0^2}\frac{h(z_0)^2}{h(z_0 a)}. \tag{4.9}$$

Since $\lim_{a\to 1} h(z_0 a) = h(z_0)$, we finally arrive at

$$\frac{dV_{\rm tot}}{dx} = \frac{L^2}{2\pi\sigma_s}\frac{h(z_0)}{z_0^2} - E, \tag{4.10}$$

which gives the critical electric field as $E_c = \frac{1}{2\pi\sigma_s}\frac{L^2 h(z_0)}{z_0^2}$.

The critical electric field E_c can also be evaluated from the DBI action of a probe D3-brane including a constant world-volume electric field, located at the radial position z_0 in the bulk. To do so, we need to work in the Lorentzian signature in which the first term in the deformed AdS_5 metric (4.1) is negative. The DBI action simply reads

$$\begin{aligned} S_{\rm D3} &= -T_{\rm D3}\int d^4x \sqrt{-\det\left(g_{\mu\nu} + 2\pi\sigma_s F_{\mu\nu}\right)} \\ &= -T_{\rm D3}\int d^4x \frac{h\left(z_0\right)L^2}{z_0^2}\sqrt{\left(\frac{h\left(z_0\right)L^2}{z_0^2}\right)^2 - \left(2\pi\sigma_s\right)^2 E^2}, \end{aligned} \tag{4.11}$$

where $T_{\rm D3}$ is the D3-brane tension. The integral is only real for $E \leqslant E_c$ where $E_c = \frac{1}{2\pi\sigma_s}\frac{L^2 h(z_0)}{z_0^2}$ which agrees with the critical value obtained from the analysis of the total potential of the quarks. Notice that E_c is a function of z_0, meaning that the critical electric field above which the pairs can be produced freely depends on the mass of the quarks, since according to the AdS/CFT dictionary the quark mass corresponds to the self-energy of a straight string stretched from the probe D3-brane, placed at z_0, to the IR-cutoff at z_h, which can be written as $m = \frac{L^2}{2\pi\sigma_s}\int_{z_0}^{z_h}\frac{h(z)dz}{z^2}$ in our problem. Thus, by changing the position of the probe D3-brane z_0, the mass of the corresponding quark would change.

Now, we turn our attention to the other critical electric field, E_s, below which quark-antiquark pairs even the ones of zero mass cannot be created from the vacuum. Thus, E_s is the electric field at which the quarks are faced with an infinitely large potential barrier, i.e., $\lim_{x\to\infty}\frac{dV_{\rm tot}}{dx} = 0$, or equivalently the total potential becomes completely flat.

Performing the same calculations as those illustrated above, the critical electric field is found as $E_s = \frac{1}{2\pi\sigma_s}\frac{L^2 h(z_h)}{z_h^2}$. Using a simple comparison, one can see that the relations of both of the critical electric fields are consistent with the ones found for the general backgrounds in [187].

4.3.3 Potential analysis

Let us now study the effect of the external electric field on the theory of our interest. In all the following results we use the values found and reported in [90]. We set the AdS radius as $L = 1\ GeV^{-1}$, and the string tension as $\sigma_s = 0.38\ GeV^{-2}$ in all cases. Also, for the quadratic deformation function we choose $\sigma = 0.22\ GeV^2$ and for the logarithmic deformation function the related parameters are chosen to be $\lambda = -0.272$ and $z_{IR} = 2.1\ GeV^{-1}$. And, for the case with both the quadratic and logarithmic terms the parameters are $\sigma = -0.34\ GeV^2$, $\lambda = -1$ and $z_{IR} = 2.54\ GeV^{-1}$. Using these values, the critical electric field below which the pair production does not occur is $E_s \approx 0.125234\ GeV^2$, $E_s \approx 0.218321\ GeV^2$ and $E_s \approx 0.248432\ GeV^2$ for the three theories mentioned above, respectively. The other critical electric field E_c depends on the mass of the quarks through z_0, the position of the probe D3-brane. In all the calculations we set $z_0 = 0.5\ GeV^{-1}$.

We first depict the graphs of the separation of the quark-antiquark pair, given in Eq. (4.4), as a function of $1/a$. Here, $1/a$ is the inverse of the rescaled radial position z of the tip of the corresponding string in the bulk, which takes its values in the interval $[z_0/z_h, 1]$, where z_h is the maximum value of z that can be reached in any case. For the pure AdS, $z_h \to \infty$, i.e., the whole radial interval is attainable. The separation lengths of the quarks for different cases are shown in Fig. 4.1. By increasing the distance x between the quarks, the tip of the corresponding string moves farther away from the boundary until it lies on a horizon at $z = z_h$, where the quarks are eventually infinitely far from each other. This happens at a finite value

of z_h for all the deformed AdS cases and is a characteristic of any confining field theory. However, in the pure AdS case, as can be seen, the quarks can be infinitely far away from each other only when the tip of the string has reached the end of the AdS space at $z \to \infty$.

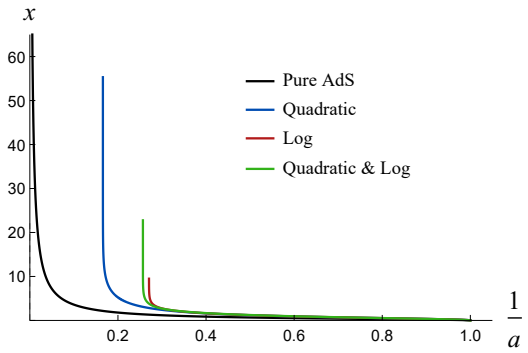

Figure 4.1: The separation length of the quarks versus the rescaled radial position of the turning point of the string for different theories.

The results for the total potential of the quarks in the presence of the electric field are summarized in Fig. 4.2. Notice that in this figure and in the following results the parameter $\alpha \equiv \frac{E}{E_c^0}$ denotes the rescaled electric field with respect to the critical electric field of the pure AdS case, i.e., $E_c^0 = \frac{1}{2\pi\sigma_s}\frac{L^2}{z_0^2}$. The left panel shows the total potential for the case with only a quadratic deformation function. As is obvious, the slope of the diagram at $x = 0$ goes to zero for $E = E_c$ and the diagram of $E = E_s$ becomes flat as $x \to \infty$, as expected from the discussions and calculations of the previous subsection. Moreover, for a sample electric field between these two critical fields, the quarks are faced with a finite potential barrier. In the right panel we compare the total potential for three values of the electric field and for three different deformation functions. It can be seen that, $\mathrm{PB}_{\mathrm{Quad}} < \mathrm{PB}_{\mathrm{Log}} < \mathrm{PB}_{\mathrm{Quad\&Log}}$, where PB stands for the potential barrier. This means that the quarks can be liberated simpler and faster in the quadratic case than in other cases. Since the Schwinger

effect happens through a tunneling process, a smaller potential barrier means that the quarks can be freed for a smaller value of the electric field.

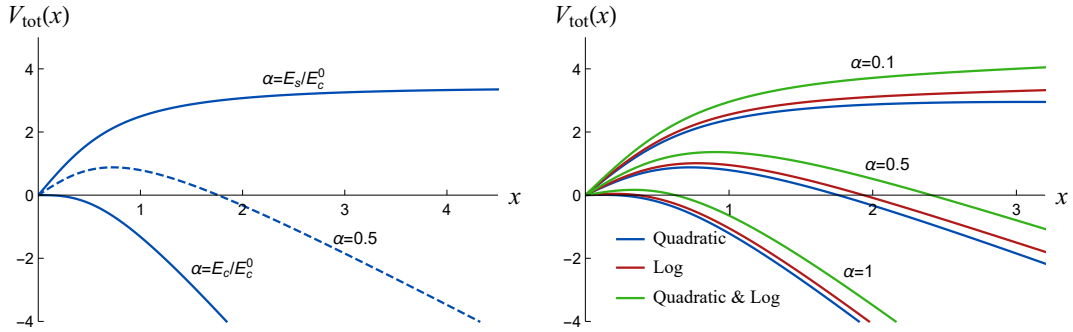

Figure 4.2: Left graph: The total potential versus x for various electric fields in the case of the quadratic deformation function. Right graph: Comparison of the total potential for different deformation functions.

Notice that the choice of the form of the deformation function in the gravity side, per se, does not have any meaning in the physics of the field theory side. In fact, in the bottom-up holographic theories one pursues the geometries with free parameters that lead to the most similar results to the experimental and lattice data. And, at the present, there exists no real experimental data in this subject as a reference. However, among these geometries with the parameters found in [90], the one leading to the results with the most similarity to the upcoming results by the next generation light sources aiming at detecting the Schwinger effect is favored as a good holographic model of QCD.

We should mention a very important issue here. The difference of the total potential of the three theories for a given external electric field comes from the fact that we have used the parameters found in [90] using the best fitted *heavy*-quark potential of these theories to the Cornell potential with the coefficients adjusted to fit the charmonium spectrum. Notice that in our problem the mass of the quarks is chosen to be finite. This assumption is required in order to be able to study

the effect of the external electromagnetic fields on the system. Therefore, we use the parameters found in [90] as the only available values, which would work as an approximation for our case with a different quark mass.

4.4 Pair production rate

This section is devoted to the calculation of the pair production rate Γ. This quantity is equivalent to the expectation value of a circular Wilson loop, in the $t-x_1$ plane, on the probe D3-brane located at z_0. x_1 is the direction of the applied electric field. Holographically, we need to evaluate the NG action of a string, attaching to the D3-brane, coupled to a constant electric NS-NS 2-form $B_2 = B_{01}dx^0 \wedge dx^1$. Then, according to the AdS/CFT dictionary, Γ corresponds to the exponential of the total action as follows

$$\Gamma \sim e^{-S} = e^{-S_{\rm NG}-S_{B_2}}. \tag{4.12}$$

The problem we are dealing with is to consider the effect of both electric and magnetic fields on the confining theory of our interest. In [184] the proposal of Semenoff and Zarembo was generalized so as to contain the study of the pair production rate in the presence of both electric and magnetic fields. We first describe the setup to calculate Γ in the presence of a constant electric field and then study the creation of quarks under the influence of both electric and magnetic fields.

To calculate the extremal surface in the bulk that shares the same boundary as the temporal-spatial Wilson loop on the D3-brane, we first need to obtain the induced metric on the string world-sheet. We choose the following ansatz for the bulk coordinates

$$t = r(\rho)\cos(\phi), \quad x^1 = r(\rho)\sin(\phi), \quad z = z(\rho), \tag{4.13}$$

where (ρ, ϕ) are the polar coordinates of the string world-sheet, and $0 \leqslant \phi \leqslant 2\pi$ and $0 \leqslant \rho \leqslant \rho_0$. The other coordinates of the bulk are chosen to be zero. Having found

the induced metric on the string world-sheet using the above ansatz and inserting it into the NG action, we arrive at

$$S_{\rm NG} = \frac{L^2}{\sigma_s}\int_0^R dr \frac{r\ h(z)}{z^2}\sqrt{1+z'^2}, \tag{4.14}$$

$$S_{B_2} = -\frac{1}{\sigma_s}B_{01}\int_0^R dr\ r = -\frac{R^2}{2\sigma_s}B_{01}, \tag{4.15}$$

where R is the radius of the circular Wilson loop on the D3-brane. Notice that we have converted the integration variable from ρ to r, and supposed that $r(\rho=0)=0$ and $r(\rho=\rho_0)=R$. When only an electric field is turned on, the only nonvanishing component of B_2 is $B_{01} = E\,(2\pi\sigma_s)$. From Eq. (4.14), the equation of motion for $z(r)$ is given by

$$2r\left(1+z'^2\right) + z\left[z' + z'^3 - r\frac{1}{h(z)}\frac{dh(z)}{dz}\left(1+z'^2\right) + rz''\right] = 0, \tag{4.16}$$

where a prime denotes the derivative with respect to r. This equation is solved numerically with the boundary conditions $z'(0)=0$ and $z(0)=z_c$ with $z_0 \leqslant z_c \leqslant z_h$. Then, to find the solution consistent with the presence of B_2, we select the configuration that satisfies the following constraint condition

$$z'|_{z_0} = -\sqrt{\frac{1}{\alpha^2}-1}. \tag{4.17}$$

Through this constraint, classical action depends on the value of the electric field.

The total action and its exponential part, i.e., the decay rate Γ are respectively shown in the left and right graphs of Fig. 4.3, where different lines indicate the results for different deformation functions with the same parameters as in the previous section. As can be easily seen, for an arbitrary value of the electric field $\Gamma_{\rm Quad} > \Gamma_{\rm Log} > \Gamma_{\rm Quad\&Log}$. This means that the pairs are produced easier in the case with a quadratic deformation function and in the case with both quadratic and logarithmic functions a stronger electric field is needed to have the same pair production rate as the other two cases. However, when the electric field approaches the critical electric

field E_c^0, the difference between the production rates in various cases becomes less obvious.

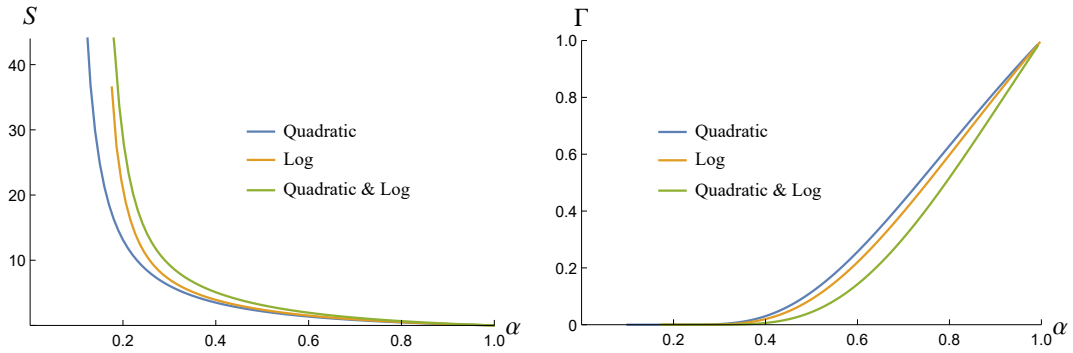

Figure 4.3: The left and right graphs respectively show the action and the production rate Γ versus the rescaled electric field for different deformation functions.

Let us now turn to the case where both electric and magnetic fields are present. Using the results of [184], the critical electric field E_c^B in the presence of parallel and perpendicular magnetic fields can be found, from analyzing the DBI action of the probe D3-brane placed at z_0, as follows

$$E_c^B = E_c\sqrt{1+\frac{B_\perp^2}{E_c^2+B_\parallel^2}}, \tag{4.18}$$

in which E_c is the critical electric field in the absence of magnetic fields, and $B_\perp$ and $B_\parallel$ are the components of the magnetic field in the perpendicular and parallel directions with respect to the direction of the electric field, respectively. It can be seen that the critical electric field is independent of $B_\parallel$ when $B_\perp = 0$ and increases with $B_\perp$ regardless of the value of $B_\parallel$.

According to the discussions and calculations of [184], all the calculations of the production rate are generalized to the case at which the magnetic fields are present

if we replace E in all the calculations with the following relation

$$E \to \frac{1}{\sqrt{2}} \left(E^2 - B_\parallel^2 - B_\perp^2 + \sqrt{\left(E^2 - B_\parallel^2 - B_\perp^2 \right)^2 + 4E^2 B_\parallel^2} \right)^{1/2}. \tag{4.19}$$

Moreover, the critical electric field E_c^B could be found by solving the same relation as follows

$$E_c = \frac{1}{\sqrt{2}} \left(E_c^{B\,2} - B_\parallel^2 - B_\perp^2 + \sqrt{\left(E_c^{B\,2} - B_\parallel^2 - B_\perp^2 \right)^2 + 4E_c^{B\,2} B_\parallel^2} \right)^{1/2}. \tag{4.20}$$

A simple analysis shows that the solution to this equation is the one in Eq. (4.18). This equality is also correct for the replacements $E_c \to E_s$ and $E_c^B \to E_s^B$, which gives

$$E_s^B = E_s \sqrt{1 + \frac{B_\perp^2}{E_s^2 + B_\parallel^2}}. \tag{4.21}$$

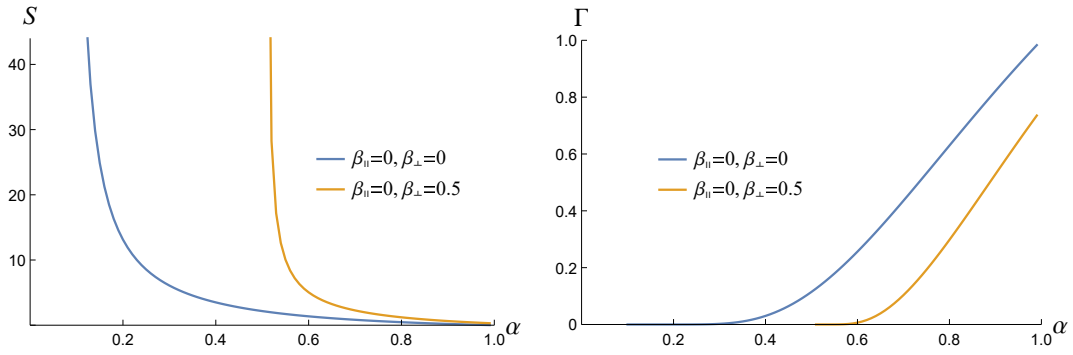

Figure 4.4: The left and right graphs respectively show the effect of the parallel magnetic field on the action and the production rate in the case of the quadratic function.

Here, we report the results in the presence of magnetic fields. In what follows we use the rescaled parameters $\beta_\perp = \frac{B_\perp}{E_c^0}$ and $\beta_\parallel = \frac{B_\parallel}{E_c^0}$. Figure 4.4 shows the effect

of the magnetic field perpendicular to the electric field direction. As a result of the presence of $B_\perp$, the pair production starts at a larger value of the electric field as expected from Eq. (4.21). Furthermore, it can be seen that $B_\perp$ decreases the decay rate at any given electric field, i.e., in the presence of $B_\perp$ we need a stronger electric field to have the same pair production rate as the case without $B_\perp$.

The next interesting problem is to consider what happens by turning on a magnetic field parallel to the direction of the electric field. As can be simply observed from Eqs. (4.19) and (4.21), when $B_\perp = 0$, there remains no track of the parallel magnetic field in the calculation of the decay rate Γ. This result is not in agreement with the results obtained in [88] where they explore the instability of confining theories influenced by external electromagnetic fields by evaluating the imaginary part of the DBI action of a probe D7-brane embedded in the bulk. Based on their calculations, they found the same qualitative results as ours, in the case where only a magnetic field perpendicular to the electric field direction is present. However, in the case of ($B_\perp = 0,\ B_\parallel \neq 0$), they realized that although the presence of a parallel magnetic field does not alter the critical electric field E_s, as in our results, it definitely affects the instability of the system for $E > E_s$; the decay rate of the system is enhanced due to the presence of $B_\parallel$. In fact, they concluded that the behavior of the system under the effect of the perpendicular magnetic field shows a magnetic catalysis, while the effect of the parallel magnetic field can be interpreted as an inverse magnetic catalysis.

Surprisingly, here in our calculations we observe no effect from the presence of the parallel magnetic field. However, by the use of Eqs. (4.19) and (4.21), we see that the instability of the system is influenced by $B_\parallel$ when both the components of the magnetic field are present. To explore the effect of $B_\parallel$ when there exists also a perpendicular magnetic field, the classical action and the decay rate of the theory are drawn as a function of the rescaled electric field α in the left and right graphs of Fig. 4.5, respectively. As can be seen from the graph of Γ, the pair production

rate increases by increasing the parallel magnetic field, showing an inverse magnetic catalysis as expected from the results in [88].

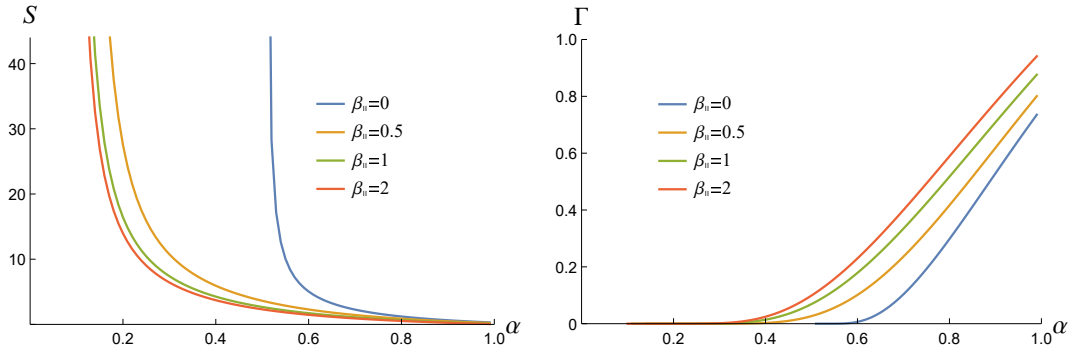

Figure 4.5: The left and right graphs represent, respectively, the classical action and the decay rate as a function of α for $\beta_\perp = 0.5$ and different values of $B_\parallel$.

We moreover depict the pair production rate versus the rescaled parallel magnetic field while the rescaled electric field α and the rescaled perpendicular magnetic field $\beta_\perp$ are fixed and nonzero, as indicated in the caption of Fig. 4.6. In this figure the results have been drawn for three deformation functions that we are interested in, for comparison. The results for the quadratic and logarithmic functions are closer to each other than the other function. From this figure one can see that for a given deformation function the production rate approaches a constant value as $\beta_\parallel$ goes to infinity, regardless of the value of $\beta_\perp$. And, the asymptotic value is the same as the value of Γ for the given α in the absence of all the magnetic field components.

Another interesting result extracted from this figure can be found in $\beta_\parallel \to 0$. It can be seen that in the absence of the parallel magnetic field, the production rate for three functions of our interest would be more similar when the value of $\beta_\perp$ increases. In fact, the difference between the theories is removed since as $\beta_\perp$ becomes large enough, the production rate vanishes, as shown in the left graph of Fig. 4.7 for a sample value of α. Similar graphs, for the case of the quadratic function, are drawn

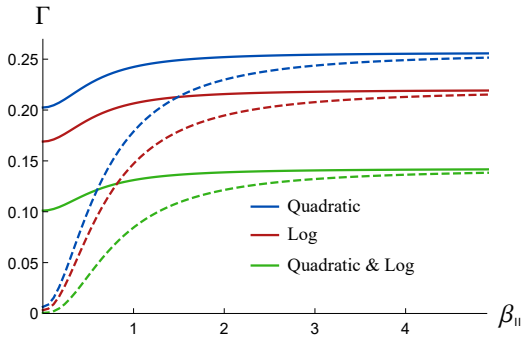

Figure 4.6: The decay rate as a function of the rescaled parallel magnetic field $\beta_{\parallel}$ with $\beta_{\perp} = 0.2,\ 0.5$ for solid and dashed lines, respectively. In all cases $\alpha = 0.6$.

in the right panel of this figure, where we can see that the presence of the parallel magnetic field postpones the decrease of the vacuum decay rate, as expected.

4.5 Summary and conclusion

The response of a confining field theory to a constant homogenous electromagnetic field has been thoroughly investigated using the gauge/gravity duality. We have chosen the metric of the gravity side to be a deformed AdS_5 with a deformation function containing a quadratic and a logarithmic term. The metric has three free parameters which have been fixed by virtue of the similarity to the Cornell potential as done in [90]. We have compared some of our results for three deformation functions; the quadratic function, the logarithmic function and the function with both quadratic and logarithmic terms. The values we have used for the parameters only works as an approximation for our problem, since here we deal with the quarks with finite mass as required for the investigation of the Schwinger effect. However, in [90] they found these parameters using the comparison of the heavy-quark potential with the Cornell potential of heavy quarks.

The critical electric fields of the system and its total potential have been found

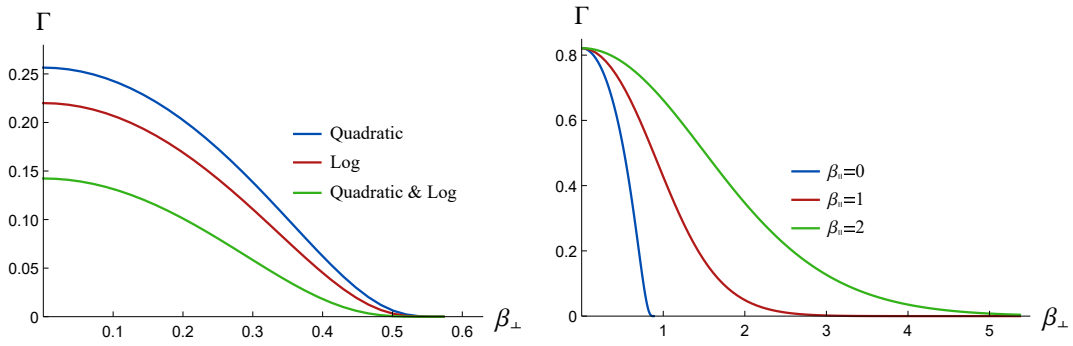

Figure 4.7: Left graph: Decay rate versus the rescaled perpendicular magnetic field $\beta_\perp$ for $\alpha = 0.6$, $\beta_\parallel = 0$ and different deformation functions. Right graph: Decay rate versus $\beta_\perp$ for the case of the quadratic function with $\alpha = 0.9$ and different values of $\beta_\parallel$.

by extremizing the action of a string attached to a D3-brane placed in the bulk near the boundary, and also the IR cutoff of the three theories, which is a generic feature of confining theories, has been obtained. We have learnt that the potential barrier the quarks are facing with, is smaller in the case of the theory with a quadratic deformation function and the theories with only logarithmic and then with both logarithmic and quadratic functions have larger barrier potential, respectively.

Furthermore, we have investigated the Schwinger effect for the system of our interest through the pair production rate which is calculated from the expectation value of the circular Wilson loop in the temporal-spatial plane on a probe D3-brane located at an intermediate radial position. Holographically, this is evaluated by extremizing the NG action of a string whose world-sheet ends on the boundary of the circular Wilson loop. We have also turned on a magnetic field to consider the effect of the simultaneous presence of electric and magnetic fields. The aforementioned result for the three cases obtained from the potential analysis has been confirmed by exploring the results of the pair production rate in the absence of the magnetic field.

We have also observed that the presence of the perpendicular magnetic field increases the value of both of the critical electric fields, meaning that the Schwinger effect begins at a higher electric field. It also suppresses the creation rate of the quarks for a given electric field above E_s. Both of these results can be interpreted as a magnetic catalysis. These results are in exact agreement, at least qualitatively, with the results obtained by calculating the imaginary part of the DBI action of a probe D7-brane equipped with an electromagnetic field strength [88]. However, for the parallel magnetic field the results found by the present approach (the string approach) and the D7-brane approach are not consistent. Here, we have found that the parallel magnetic field does not alter the critical electric fields and the instability of the system at all, while in the D7-brane approach, although $B_\parallel$ does not change E_s, it enhances the creation rate of the quarks at a given electric field. This contradiction is probably due to the fact that the string world-sheet and DBI action are different approximations of the string theory and some particular corrections are ignored in the DBI action. We have mentioned one other consequence of the difference between the two approaches in our previous work on the Schwinger effect [201].

To reveal any effect of $B_\parallel$, we have considered the response of the system to the increase of $B_\parallel$ when $B_\perp$ is also present but have a fixed value. In this situation, $B_\parallel$ starts to show off. Its effect is the increase of the production rate consistent with the result in the D7-brane scenario. However, the increase of Γ due to the increase of $B_\parallel$ continues until at $B_\parallel \to \infty$, Γ approaches an asymptotic value which is the same as the one in the absence of all components of the magnetic field. In fact, the only effect of the increase of $B_\parallel$ is to compensate the decrease of Γ due to the presence of $B_\perp$. In conclusion, we realize that, according to the string approach, one cannot find a higher chance of producing quarks by applying magnetic fields and the highest values for Γ are the ones with zero $B_\parallel$ and $B_\perp$. However, in the D7-brane approach the result is completely different; one can enhance the production rate at will and make the Schwinger effect more detectable by applying a magnetic field parallel to

the electric field. This result is important in that the Schwinger effect is too weak to be observed experimentally by the strongest electric fields that can be produced in our present laboratories and therefore any theoretical or experimental effort to make this elusive effect observable should be scrutinized.

Chapter 5

An Introduction to Star and Galaxy Formation

This chapter aims to provide the minimum essential background knowledge for the following chapter. We start by describing the structure of a galaxy and its components. Also, we explain the classification of galaxies based on their morphologies, and we go over the structure of our galaxy, the Milky Way. After that, we introduce different types of stellar groups and point out the importance of studying young stellar populations. Then, we discuss the necessity of leveraging galaxy simulations. Finally, we introduce a clustering algorithm called Frineds-of-Friends, and we argue why it is a suitable tool for identifying stellar groups in galaxy simulations.

5.1 Galaxies

Most of the content of Section 5.1 can be found in any standard astrophysics textbook [e.g., 37, 108, 204]; so, definitions and numbers given in this specific section are not necessarily the most updated definitions and measured values. However, they are sufficiently accurate to create a holistic and coherent picture of the subject and

to provide a general sense of (1) common jargon used in astrophysics and astronomy and (2) the order of magnitude of different parameters for the reader. Regarding parameters that we need to be mindful of their most updated values for our study in Chapter 6, we have provided accurate values and explicitly included the source reference.

5.1.1 Components of A Galaxy

A galaxy is made of several components; stars, gas, dust (a.k.a. dust grains), light (electromagnetic radiation), and dark matter. Some stars are near others, forming stellar groups, while some are part of binary pairs. Additionally, some stars exist without nearby companions within a relatively short distance of a few parsecs [†]. Gas and dust are spread in the space between the stars known as the *Interstellar Medium (ISM).*

Gas exists in different forms, atomic, molecular, and ionized gas. Neutral atomic hydrogen (HI) is the most abundant component of the ISM and exists both within and outside of star-forming regions with temperatures typically in the range of 100 to 10,000 Kelvin.

Molecular gas usually refers to molecular hydrogen (H2), carbon monoxide (CO), water (H2O), ammonia (NH3) and some organic molecules. H2 and CO are often in the colder and denser regions of galaxies, primarily in molecular clouds which are the formation sites of stars. The temperature within molecular clouds is typically in the range $10 - 30$ Kelvin.

The dominant type of ionized gas, within a galaxy, is hydrogen ions (HII or simply protons). Ionized hydrogens are often around hot young stars where the ultraviolet radiation of such stars has enough energy to ionize the nearby hydrogen

[†] A parsec, usually denoted by pc, is a unit of distance commonly used in astronomy and astrophysics, equal to ≈ 3.26 light-years.

atoms. Regions of ionized gas are called HII and have temperatures of 8000-10,000 kelvin [‡]. HII regions are very important in the context of star formation.

In contrast to gas, dust grains—in the context of galaxies and astrophysics—are tiny solid particles composed of chemical elements like carbon, silicon, oxygen, iron, and hydrogen. The most common types of dust grains are silicates (i.e., silicate-rich dust), carbonaceous material (i.e., carbon-rich dust), and metallic oxides. The size of dust grains is on the order of a few nanometers to a few micrometers. They can be found throughout the ISM of galaxies, often mixed with molecular clouds. Dust grains play a crucial role in shielding the cold dense regions of ISM where star formation occurs, because they can absorb ultraviolet and visible light and re-emit it at infrared and longer wavelengths. When a clump of gas molecules is cold and sufficiently dense, it can collapse—due to the gravitational interaction between its gas molecules—and form a star. In the absence of dust, the UV photons from other stars can move through the ISM and break up the cold dense molecules, and in turn, stars cannot form.

5.1.2 Classification of Galaxies

Galaxies can be classified based on various criteria, with morphology being a common one. Regarding morphology as a criterion, we list and briefly introduce only three types of galaxies, although the complete list contains more than three types.

1. **Spiral galaxies:** A spiral galaxy has a flat disk shape that is composed of a few spiral arms. The disk keeps rotating and spiral arms keep winding outward. Our own Milky Way and Andromeda are two classic examples of spiral galaxies.

[‡] In this thesis we do not need to introduce Coronal or *Hot Ionized Medium (HIM)* where the temperature of ionized gas can be as high as several million kelvin.

2. **Elliptical galaxies:** Elliptical galaxies have a round shape, ranging from nearly spherical to elongated ellipses. Their stars are usually older and cooler than stars in spiral galaxies.

3. **Irregular galaxies:** Shapes of irregular galaxies look chaotic. The unusual shape of these galaxies can be the result of recent interactions with passing galaxies or mergers.

5.1.3 The Milky Way

The Milky Way is a spiral galaxy containing baryonic mass (stars, gas, dust), non-baryonic mass (dark matter), and electromagnetic radiation (photons). The spatial distribution of these elements determines the physical shape of the Milky Way. The Milky Way's shape, at scales of kiloparsec, is composed of four independent components: a central spheroid called the *central bulge* centered on the *galactic center* with a radius of ~ 4 *kpc*, two galactic disks called the *thin disk* and *thick disk* each with a radius of ~ 25 *kpc*, and a huge spheroid called the *Galactic Halo* centered on the *glactic disk* with a radius of > 100 *kpc* [†].

For projects discussed in this thesis, our focus is on gas and stars residing in the thin disk and thick disk. These two disks are not cylindrically symmetric; instead, they look elliptical with an eccentricity—i.e., the ratio of the length of the minor to major axis—of ~ 0.9. Thin disk. The stellar number density $n(z, R)$ —i.e., the number of stars per unit volume—for the thin and thick disk can be derived from star count data. The empirical fits to the star count data can be expressed as

$$n(z, R) = n_0(e^{-z/z_{thin}} + 0.085e^{-z/z_{thick}})e^{-R/h_R} \tag{5.1}$$

where z is the vertical distance from the *galactic midplane*, and R is the cylindrical radial distance from the galactic center. The coefficient $n_0 \sim 0.02$ stars per pc^3,

[†] See Joss Bland-Hawthorn and Ortwin Gerhard (2016) [25] for more trusted and accurate values.

and the coefficient 0.085 indicates that stellar density in the thick disk is 8.5% of the stellar density in the thin disk at galactic midplane ($z = 0$). The parameters z_{thin}, z_{thick} are the scale height of the thin and thick disk, and h_R is the disk scale length. The thin disk is the region of current star formation, so it mainly consists of relatively young stars. In contrast, the thick disk is generally composed of the older population of stars.

5.2 Stellar Groups

A stellar group is a collection of stars held together by mutual gravitation and moving together through a galaxy as a relatively coherent unit. Stellar groups exist in various forms, shapes, gravitational bounding statuses, and sizes, ranging from small, irregular *loose associations* of a few dozen stars to large, dense, symmetric, *bound clusters* containing thousands or even millions of stars. In this section, we review the key characteristics of only a subset of different types of stellar groups including open clusters, globular clusters, embedded clusters (a.k.a. young star clusters), and young star associations.

5.2.1 Open Clusters

An open cluster (OC) is a group of 10s-100,000s stars generally thought to have formed from the same molecular cloud of gas and dust at approximately the same time and location. The stellar mass of an open cluster is in the range 10^3 to 10^7 $M_\odot$, and the typical radius of an open cluster is in the range 0.5 to several parsecs [173]. To highlight the high stellar mass density of open clusters compared to our nearby regions, we just need to recall that the Sun and Alpha Centauri—i.e., the closest star to the Sun—are $\sim$ 1.3 parsec away. In contrast, open clusters contain tens to tens of thousands of stars within approximately a similar distance, making them significantly denser stellar environments than our immediate surroundings.

Stars of an OC are usually relatively young (within the range of 1 Myr to a few hundred Myrs), but there are rare OCs with ages estimated of the order of 10 Gyrs [181]. OCs exist in spiral and irregular galaxies, as these galaxies have star-forming regions. In contrast, they cannot be found in elliptical galaxies, because these galaxies do not form new stars and their OCs have already been dispersed. In spiral galaxies, such as our Milky Way, the majority of OCs reside in the galactic disk inside and between the spiral arms. The number of cataloged Milky Way's OCs is nearly 14,000 [159]. The majority of OCs are gravitationally unbound and short-lived on cosmic timescales, and their shapes are asymmetric with huge amounts of gas between the stars.

As OCs move through space, the gravitational pulls from other passing massive bodies and structures (stars, molecular gas, and clumps of dark matter) and their internal dynamics can disperse their stars. Consequently, many OCs gradually drift apart over a few Myrs [22, 127]. This may be the case with our Sun. It may have formed in an open cluster and later dispersed from its natal cluster [126]. OCs are important subjects to study, because each OC is a unique factory of star formation and evolution.

5.2.2 Globular Clusters

Globular are groups of $10,000 - 1,000,000s$ of stars tightly bound together by gravity. In comparison to open stars, the size, stellar mass and stellar density of globuar clusters are significantly larger. As reflected in their name, globular clusters have a roughly spherical appearence. Due their highly dense structure, their gravitational bound is intense and keeps stable and long-lived (for several billion years); as opposed to open clusters that usually disperse within a few Myrs. Consequently, stars in globular clusters are older than stars in open clusters. Globular clusters can be found in all types of galaxies. In spiral galaxies, they are generally located in the

bulge and halo, and not in the disk. So far, $\sim$ 150 of Milky Way's globular clusters [87, 214], $\sim$ 400 of Andromeda's open clusters have been identified [157]. The old age—typically in the range $9-13$ Gyrs [212]—of stars in globular clusters make them informative structures to study, as they have imprints of the formation and evolution of old metal-rich stars (a.k.a *population II stars*).

5.2.3 Embedded Clusters

An embedded stellar group is a collection of newly born stars still embedded in their natal molecular cloud which is an active star formation region (HII region). As the newly born stars get older, stars and their natal gas fall apart through various mechanisms (for instance, due to stellar feedback that will be discussed in section 6.2.1). After star formation ceases, if an embedded stellar group does not disperse, it becomes an open cluster or a stellar association, but the majority of young stellar groups drift apart before the star formation ends—from stellar feedback and passing objects due to their weak gravitational cohesion. Bound young stellar groups have a higher chance to survive from disruptions and are called *young star clusters*. In contrast, unbound young stellar groups usually drift apart, and are named *young stellar associations* (a.k.a. *young loose association*).

Although the embedded phase of young stellar groups often lasts $2-7$ Myrs [118, 117], different authors set different upper limits for stellar ages—typically a value less than 100 Myrs—to separate young stellar clusters from the general term of open star clusters. For instance, in [173] and [137] authors define young massive star clusters as groups of stars younger than $\sim$ 100 Myr, that is more than a few current crossing times, with masses greater than $\sim 10^4$ $M_\odot$, but in [124] authors study YMCs and YMAs with ages in the range $1-5$ Myrs with stellar masses in the range $\sim 10^2$ - 10^4 $M_\odot$. Young stellar groups exist in galaxies with star-forming regions (spiral and irregular galaxies). In spiral galaxies, they are in the galactic disk.

5.3 Importance of Young Stellar Groups

There are various motivations for studying young stellar groups. In this section, we briefly highlight some of them.

1. **Early Stage of Star Formation:** It must be noticed that the process of star formation is nonlinear and usually chaotic. If we want to know about this process, young stellar clusters are the most reasonable system to study.

2. **Stellar Feedback:** We may ask why do young stellar associations disperse before the end of star formation or within a few million years afterward? Which star feedback drives this process?

3. **Connecting the Physics of Different Scales:** As mentioned in subsection 5.2.3, in spiral galaxies, young stellar groups are in the disk and often along the spiral arms. In practice, we can think of young massive clusters as the building blocks or at least a statistical sample of spiral arms [126]. We should also note that the size of young stellar groups is a few parsecs, while the length of spiral arms is often > 10 kpc. These together mean by connecting the physics of young star clusters to the physics of spiral arms, we can find the connection between the physics of two different scales. It is evident that to find this connection, we first need to gain a deep understanding of the physics of each of these two significantly different scales.

4. **History of Open and Globular Clusters:** Embedded clusters identified at low and high redshifts precede the formation of open and globular clusters, respectively. It simply means they can tell us about the formation history of open and globular clusters.

5. **Exploring Novel Horizons:** Studying the physics of young stellar groups has opened new horizons to explore such as the following interesting case. When we

observe the stars moving through the galaxy, we see two classes of stars; stars that are part of a stellar group, and stars that are not part of any specific stellar group. Stars of the latter class are called *field stars*. Our Sun is a very good example of a field star. We also know that stars can be born either individually or in groups. Some stars are formed in isolation, without the presence of other stars nearby. These stars form from the gravitational collapse of dense regions within molecular clouds. Other stars are born in groups, where multiple stars form at the same time within a short distance (< a few parsec) from one another from the same parent molecular cloud. As we discussed in subsection 5.2.3, most stellar groups, especially young stellar associations, break apart within a few Myrs, and their stars disperse into the general population of field stars. Now, it is very natural to ask if we can determine which field stars were born in isolation and which ones were born in groups. We can ask this question for a very special case, the Sun. And as discussed in [126], is it possible to know if the Sun was born in a group or isolation? If yes, then how? And, if the Sun was born in a group, where are the siblings of the Sun? And, do they host planets like the Earth? Indeed such interesting questions can be addressed by studying the evolution of stellar groups.

5.4 Simulations

In general, simulations complement observations and provide a framework for interpreting observations [51]. By comparing simulation results with observational data, we can test the validity of theoretical models in a controlled environment, allowing us to explore a wide range of parameter space and initial conditions. Subsequently, we can refine existing models and develop new theories that better explain the observed universe.

5.4.1 The Vital Role of Galaxy Simulations in Astrophysical Studies

In astrophysics, simulations of galaxies have emerged as indispensable tools for several reasons. Here we briefly point out only two main reasons.

First, astrophysical systems are inherently complex, involving a multitude of physical processes operating over a wide range of scales (from $\sim$ parsec scale to $\sim$ 100 Mpc scales). The relevant physical processes are diverse including gravity, gas dynamics (hydrodynamics), star formation, feedback from supernovae, stellar winds and active galactic nuclei, gas heating and cooling, and chemical evolution. These processes interact in nonlinear ways, making it challenging to theoretically model all aspects of galaxy formation and evolution.

Second, observational data alone often provide only momentary instances of cosmic phenomena, limited by the constraints of telescopes, detectors, and observational techniques. Many important aspects of galaxy formation and evolution occur on timescales or in environments that are impossible or challenging to observe directly. Simulations offer a way to study these aspects, filling in gaps in our observational knowledge. Simulations can make predictions of observable signatures of galaxy evolution, such as star formation rate (SFR), morphology of galaxies, and properties of various stellar populations, et cetera. By comparing these predictions to observations and theoretical models, we can infer the underlying physical processes driving galaxy formation and evolution and, in turn, refine or constrain theoretical models.

5.4.2 What Lies Within Galaxy Simulations

Simulations of galaxies are helpful tools for testing astrophysical hypotheses related to galaxy formation and evolution, stellar dynamics, and the interplay between different physical processes. By varying parameters such as the density of dark matter or the strength of feedback processes, we can assess the impact of different

physical mechanisms on the formation and evolution of galaxies. The following is a list of the astrophysical hypotheses that can be addressed by utilizing simulations of galaxies.

1. **Galaxy Formation and Evolution:** Investigating the processes that lead to the formation of galaxies, and their morphological evolution.

2. **Stellar and Galactic Dynamics:** Studying the dynamics of stars and gas within galaxies, including the formation of spiral arms, bars, and central bulges, as well as the interaction between galaxies and nearby satellite and dwarf galaxies.

3. **Feedback Mechanisms:** Understanding the role of feedback mechanisms such as supernovae, stellar winds, photoionization, photoelectric heating, radiation pressure, and active galactic nuclei in regulating star formation, shaping the interstellar medium, and driving galactic outflows.

4. **Cosmological Parameters:** Confronting simulations with observations allows for the determination of cosmological parameters such as the density of dark matter, the amplitude of density fluctuations, and constrain the nature of dark matter.

5.4.3 Limitations and Caveats

Despite all the valuable insights that galaxy simulations can offer, they come with limitations and may not be able to address certain questions that require new physics or exploration of inaccessible regimes. Some important caveats include:

1. **Fundamental Physics Beyond Our Current Understanding:** Simulations rely on our current understanding of physical laws and processes, so they

cannot probe phenomena that require entirely new physics or are beyond the scope of our current theoretical framework.

2. **Unobservable or Inaccessible Regimes:** Simulations are limited by computational resources and physical models. Due to the latter limitation, simulations may not be able to explore extreme environments such as the interiors of black holes or the earliest moments of the universe.

3. **Fine-Tuning or Fine-Scale Structures:** Simulations have finite resolution and may not capture fine-scale structures or require fine-tuning of parameters beyond current capabilities.

4. **Simplified Models:** Our understanding of many astrophysical processes is incomplete, and models often rely on simplifications and approximations due to computational constraints. While these simplifications are necessary for practical reasons, they may not fully capture the complexity of astrophysical processes.

5. **Uncertainties and Assumptions:** Simulations are subject to uncertainties in model parameters, initial conditions, and the treatment of physical processes. Assumptions made in the simulation setup can introduce biases or inaccuracies into the results.

6. **Numerical Artifacts:** Numerical techniques used in simulations can introduce artifacts or biases into the results, particularly at small scales or in regions of high density or velocity.

7. **Stochasticity and Randomness:** Some astrophysical phenomena exhibit stochastic behavior or randomness, which cannot be fully captured by deterministic simulations. For example, the formation of individual stars within molecular clouds involves random fluctuations and turbulence.

8. **Degeneracies:** There may be multiple combinations of physical parameters or feedback mechanisms that produce similar observational features. This degeneracy makes it challenging to uniquely determine the underlying physical processes solely based on observations or simulations.

9. **Interpretations:** Interpreting simulation results requires careful consideration of the underlying physical processes and their implications for observed phenomena. Misinterpretation or overinterpretation of simulation results can lead to wrong conclusions.

We should also note that while observational data provide valuable constraints for testing models, they may not fully capture the complexity of astrophysical systems. Observations are often limited by instrumental effects, observational biases, and the difficulty of observing certain regions.

Due to these challenges, the process of matching simulations with observations is iterative and involves refining models based on comparisons with observational data, exploring parameter space, and testing alternative hypotheses. It requires a combination of theoretical insight, computational techniques, and observational data analysis to develop robust models that can accurately reproduce observed phenomena. Additionally, interdisciplinary collaboration between theorists, computational scientists, and observers is crucial for advancing our understanding of astrophysical processes and improving the fidelity of simulations.

5.5 Clustering Algorithms

Clustering is a very well-studied subject in both computer science and applied mathematics, and it has found a lot of applications in other fields. The main idea is to classify a set of data into some subsets according to a specific feature or criterion—or in general, a set of criteria. For the study discussed in Chapter 6, we need to utilize a

clustering algorithm to find stellar groups, so the simplest and most generic criterion for a clustering algorithm is spatial proximity of data points—location of stars in three dimensions—using Euclidean metric and assuming the space is flat.

Within the past 40 years, different groups in different fields of studies including astrophysics and cosmology, have contributed to and worked on developing various algorithms like Friends-of-Friends (FoF)[57], KMeans, Spectral, Ward, OPTICS, Birch, Gaussian mixture, DBSCAN, and HDBSCAN. Hunt and Reffert (2018) [104] have discussed and compared the efficiency of Gaussian mixture, DBSCAN, and HDBSCAN in identifying stellar groups in Gaia data, and concluded that HDBsacan is the most efficient algorithm and returns the most accurate results. Despite Hunt and Reffert's conclusion, we choose to use FoF to identify stellar groups for our work. In this section, we explain how FoF works, and why we believe it is a more suitable algorithm for our study.

5.5.1 Friends-of-Friends (FoF)

This algorithm employs a fixed value for a parameter called linking length, which the user should set. The FoF algorithm starts by selecting an arbitrary star. Then, it links the star to all stars in a distance $\leq$ linking length. These stars are named the "friends" of the star. Then, the FoF algorithm repeats this process on each "friend" to find the "friends of (this) friend". The collection of stars linked together is identified as a group (here, either a cluster or an association), and the number of stars in a group is called the group's size (or population).

5.5.2 History of FoF

The evolution of the FoF algorithm is intricately woven through several key contributions. Huchra and Geller in 1982 [103] laid the foundation, introducing a basic algorithm illustrated as a flowchart. Their approach, developed for identifying galaxy

clusters, set the stage. In this work, linked galaxies are named "companions of companions." Simultaneously, Press and Davis in 1982 [176] presented a refined version to identify virialized subsystems. They coin the term "friends of friends" instead of "companion of companions." Notably, they acknowledged Huchra's work, stating, "Huchra and Geller (1982) have identified galaxy groups in the CfA Redshift Survey data by means of an overdensity criterion which does not discriminate against unvirialized systems." Advancements continued. In 1984, Einasto et al. in 1984 [57] put forth a more precisely defined FoF algorithm. This work is pivotal, as it explicitly articulates the fundamental idea behind the FoF algorithm. It has become a standard reference in educational settings, forming the basis for understanding FoF algorithms. The year after, Davis et al. in 1985 [47] delved into the intricacies of the algorithm. They explored the critical aspect of the linking length's significance, especially in the context of galaxy clusters and N-body simulations. This detailed examination significantly influenced subsequent research, particularly in studying large-scale structures. That is why people working on large-scale structures often cite Davis et al. (1985) when they discuss FoF algorithms. It might be worth mentioning that Huchra, Geller, Davis, and Einsasto were collaborators in the 1980s.

5.5.3 Pros and Cons of FoF

FoF offers both benefits and drawbacks when compared to other methods employed for the same purpose. Understanding these advantages and limitations is crucial for making informed choices in cluster analysis. In this subsection, we will discuss the drawbacks and benefits of using FoF in comparison to other methods and explore how the benefits outweigh the drawbacks when an appropriate choice of *linking length* and *age cut*—the upper limit for the age of stars; we set this parameter to study stars with a specific range of ages—is made for the FoF algorithm.

One of the significant drawbacks of the FoF algorithm is its sensitivity to the

choice of the *linking length* parameter. The *linking length* determines the spatial distance within which stars are considered connected. If the *linking length* is too large, it may lead to the merging of distinct clusters, resulting in the loss of cluster separation. On the other hand, if the *linking length* is too small, it may fail to identify physically connected stars within a cluster. Therefore, careful parameter tuning is required to achieve optimal results.

Another limitation of the FoF algorithm is its dependence solely on spatial information. It does not take into account other characteristics such as stellar velocities or photometric properties, which can be important indicators of cluster membership. This limitation can result in the inclusion of field stars within a cluster.

Despite these drawbacks, the FoF algorithm offers several benefits that make it a popular choice in cluster analysis. One of the key advantages is its ability to identify spatially extended and irregularly shaped clusters or associations effectively. FoF can capture complex morphologies that may not be easily detected by other methods. In contrast, HDBSCAN—identifying stellar groups characterized by varying densities—may encounter challenges in effectively discerning stellar groups characterized by irregular shapes and sizes.

Additionally, when an appropriate choice of *linking length*—while considering the resolution limits—and *age cut* is made for the FoF algorithm, the benefits can outweigh the drawbacks. By carefully selecting the *linking length*, the FoF algorithm can accurately capture the desired level of cluster connectivity. Similarly, the *age cut* parameter can be used to refine the identified clusters and associations based on their age characteristics. By tuning these parameters, one can achieve a balance between capturing the true cluster structure and minimizing contamination from field stars.

Furthermore, the FoF algorithm is computationally efficient and easily implemented, making it suitable for analyzing large datasets with millions of stars. Its simplicity and intuitive nature allow to quickly explore the clustering properties of stellar systems. Traditional photometric methods used in observational studies

(such as stellar density threshold, color-magnitude diagram analysis, and color-color diagrams) heavily rely on the accuracy and completeness of the photometric data, stellar evolution models, and assumptions about the reddening law, and often rely on predefined criteria or require manual identification, limiting their effectiveness in large-scale surveys. In contrast, the FoF algorithm can automatically identify groups of stars based on their spatial properties, enabling the detection of structures that may have gone unnoticed in large-scale surveys otherwise. For our study presented in Chapter 6, FoF works well, because we do not have errors on positions or distances of stars in galaxy simulations.

In conclusion, while the FoF algorithm has certain drawbacks, such as its sensitivity to parameter choices and reliance solely on spatial information, its benefits make it a valuable tool in identifying star clusters and associations. Its ability to detect complex morphologies and accommodate varying levels of cluster density, coupled with its computational efficiency, contributes to its widespread usage. In the next chapter we explore if by selecting appropriate values for *linking length* and *age cut*, the FoF algorithm can yield reliable results, enabling us to unravel the structures and properties of stellar systems effectively.

Chapter 6

Young Massive Star Clusters at Present Day in the *Latte* Galaxy Simulations

Star clusters provide valuable insights into star formation processes in the Local Universe. While a significant fraction of the stars in the Galactic disk are believed to form in clusters, their evolutionary path from cluster to field population remains unclear. In this study, we explore the generation of realistic young massive star clusters (YMCs) and young massive stellar associations (YMAs) in cosmological galaxy simulations at present day and investigate the relationship of their properties with the Galactic environment. Additionally, we aim to establish suitable criteria for comparing YMCs and YMAs in Milky Way-like simulations with observationally detected YMCs and YMAs in the Milky Way. To achieve our goals, we utilize the *Latte* suite of FIRE-2 Milky Way-like galaxy simulations [217, 102], which offer high spatial, mass, and temporal resolution for zoom-in cosmological galaxy simulations; along with the default (metal diffusion) physics runs, we analyze the effects of magneto-hydrodynamics on re-runs of the same simulations [99, 97, 207].

Employing the friends-of-friends (FoF) algorithm, we identify stellar groups with masses $\gtrsim 10^{4.5}$ $M_\odot$) within the simulations. To ensure robust results, we carefully explore the parameter space of the FoF algorithm, optimizing the values of FoF parameters to identify reasonably realistic star clusters. Preliminary analysis of six *Latte* galaxies reveals promising agreement with Hubble Space Telescope, Gaia and SDSS observations across key stellar group metrics, including median cluster size ($r_{half} \sim 2.7$ pc), 1D velocity dispersion ($\sigma_{v1D} \sim 4.0$ km/s), and spread in metallicity ($\sigma_{[Fe/H]} \sim 0.02$ dex). Our study demonstrates the potential of the *Latte* suite of FIRE-2 simulations to reproduce realistic star clusters and their properties. Further investigation will enable us to unravel the intricate connection between cluster formation, galactic environment, and the evolution of star clusters in the Milky Way.

6.1 Introduction

Star clusters and associations[†] are fundamental structures in the cosmos, providing valuable insights into stellar evolution, galactic dynamics, and the formation of stars and planetary systems [48, 137]. In particular, identifying and characterizing these stellar groups is crucial for advancing our understanding of how and why stars and stellar groups form [e.g., 43, 95, 123], why stars form at the rate they do [e.g., 193, 121], why stars and star clusters and associations form with a particular mass distribution [128, 15, 94], and how stars and star clusters and associations influence gas around them and vice versa [113, 83, 149].

In recent years, Gaia has revolutionized our statistical understanding of stellar groups including open clusters (OCs) and loose unbound associations within the Milky Way. The number of OCs cataloged pre-Gaia was ~ 3000, but now it's nearly 14,000, with the majority discovered by Gaia [159]. Furthermore, the high precision

[†] It is a common convention to use the term 'cluster' to denote a gravitationally bound stellar group, distinguishing from 'association,' which refers to an unbound stellar group.

of Gaia DR2 enabled both probing the internal kinematics of star clusters at the sub-km s^{-1} scale [124], and refinement of catalogs to exclude coincidental asterisms and include new sources based on coherent positions, proper motions and parallaxes [36].

The enhanced accuracy in proper motion (by a factor of about 2) and parallax (by a factor of about 1.5) in Gaia DR3, compared to Gaia DR2, significantly impacts the precision of cluster parallax measurements [30, 66]. The improved proper motion enables better identification of cluster members, particularly those at greater distances. With Gaia DR3 and utilizing the Hierarchical Density-Based Spatial Clustering of Applications with Noise (HDBSCAN) algorithm [35], a study identified 4105 highly reliable clusters, including 739 new clusters [104]. The authors also proposed that numerous clusters, which they could not identify, might not be real clusters. This includes 1152 clusters listed in the Milky Way Star Cluster (MWSC) catalog [114, 115, 192, 195] that were expected to be identifiable in Gaia data.

This advancement coincides with a critical phase in near-field studies of star clusters in external galaxies with programs like LEGUS [33, 34], PHANGS-HST [129, 131, 133], and PHANGS-JWST [130, 132]. Through programs like these, catalogs of star clusters in 88 local universe galaxies, at distances of $\sim 3.5 - 23$ Mpc, are now publicly available. These datasets, combined with PHANGS-ALMA [134] and PHANGS-MUSE [58] data, enable us for the first time to link young stellar groups with their birth environments across a statistically significant sample of environments [73, 191, 190].

Although there is a large sample of observed OCs, the number of YMCs and YMAs observed in the Milky Way is limited, because the search for these objects is challenged by their complex birth surroundings. In this study, we consider YMCs and YMAs as both embedded stellar groups and very young open clusters. In the early stages of YMCs and YMAs, they are embedded in their natal environment and in turn obscured by the dense interstellar medium and neighboring clusters

[126, 218, 125, 132], making it intricate to distinguish their individual emissions. In short, they are rare objects and difficult to observe due to extinction and inclination effects.

A study [173] compiled data on the measured properties of YMCs and YMAs observed in the Milky Way, in the Local Group and outside the Local Group before Gaia DR2. They reported properties of 12 observed YMCs in the Milky Way; their total masses are in the range $10^{3.80}$ $M_\odot$ to $10^{4.70}$ $M_\odot$ with ages of $2.00 - 18.00$ Myr, and one-dimensional velocity dispersion is reported only for three of them[†] , falling in the range $3.40 - 5.80$ km s^{-1}. They also reported properties of 13 YMAs in the Milky Way; their masses are in the range $10^{3.30}$ $M_\odot$ to $10^{4.40}$ $M_\odot$ with ages between $1.00 - 14.50$ Myr, and one-dimensional velocity dispersion is not reported for any of these thirteen stellar associations.

Using Gaia DR2, [124] studied a sample of 28 YMCs and YMAs with half-mass radii in the ranges 0.3 to 3.7 pc, with stellar masses $10^{2.12}$ $M_\odot$ to $10^{4.14}$ $M_\odot$, with ages $\sim 1 - 5$ Myr and found one-dimensional velocity dispersions for their sample in the range $\sigma_{1D} = 0.8$ to 2.8 km s^{-1} with a mean of 1.8 km s^{-1}.

Despite persistent observational challenges, recent progress in galaxy zoom-in simulations enables the comprehensive study of Giant Molecular Clouds (GMCs) and star clusters within a cosmological galactic framework. Unlike earlier galactic models, which were constrained by limited resolution in capturing stellar feedback, internal cloud structure, cloud motions, and shocks, the latest simulations overcome these challenges. Previous models also struggled to replicate observed GMC temperatures and densities and often excluded magnetic fields [53].

To achieve simulations incorporating all these features as well as larger-scale processes—such as cosmic gas accretion, wind recycling, and perturbations from

[†] While in [173], from the twelve listed YMCs, only three of them have reported one-dimensional velocity dispersion, in subsequent literature there are reported one-dimensional velocity dispersion for some of these YMCs.

satellite galaxies—in a cosmological context, it is required to overcome the computational limitations, primarily stemming from the essential wide range of time and spatial scales—spanning from parsec scales, where star formation occurs, to tens of kiloparsecs encompassing galactic structures, and finally, to megaparsecs where cosmological effects dominate. The recent evolution of simulation code has remarkably reduced run times, providing the realism and resolution necessary for studying the formation and evolution of star clusters throughout the evolution of their natal molecular cloud in a cosmological setting [217, 100, 102].

In this chapter, our primary goal is to examine the basic properties of YMCs and YMAs younger than 3 Myr at identification and more massive than $\sim 10^{4.5}$ $M_\odot$ in cosmological galaxy simulations at redshifts $z < 0.008$. We limit our study to young stellar populations because we want to ensure identifying truly conatal populations, and we pick massive stellar populations because that is what we can resolve with the current resolution ($\sim$ 7100 $M_\odot$)) of the simulations. The measured properties include boundedness, mass, size, 1D velocity dispersion, spread in metallicity [Fe/H] and age. We utilize the *Latte* suite of Feedback in Realistic Environments (FIRE-2) Milky Way-like galaxy simulations [217], which offer high spatial ($\sim$ 1 parsec), gas & star particle mass ($\sim$ 7100 $M_\odot$), and temporal ($\sim$ 1 Myr) resolution. We present analysis of three galaxy simulations, `m12f`, `m12i` and `m12m`; we include analysis of runs that include the default (metal diffusion) FIRE-2 physics, as well as analysis of runs that include the effects of magneto-hydrodynamics [99, 97, 207]. A discussion of the kinematics and metallicity of all the stars at birth in the default physics runs can be found in [145] and [18].

For identifying star clusters and associations, while observational studies often rely on photometric estimators like light blobs and concentration indexes, we adopt a Friends-of-Friends (FoF) algorithm [57]. This choice is driven by our ability to access the exact positions of individual stars in galaxy simulations, and the ability of FoF in identifying stellar groups with irregular shapes and complex morphologies. The FoF

algorithm, initially developed in cosmology and N-body simulations [103, 176, 47], has found a natural application in the study of star clusters and associations, because it is a versatile algorithm and can be adapted to different spatial scales; from very large scales $\sim$ Mpc (to identify galaxy groups and clusters) down to much smaller scales $\sim$ pc (to identify stellar groups and clusters). Briefly, the FoF algorithm leverages the concept of spatial proximity, enabling the connection of stars that exhibit close proximity in space. This characteristic empowers the algorithm to discern both dense clusters and looser associations within a given dataset, thereby facilitating comprehensive analyses [52, 136, 19].

After identifying YMCs and YMAs in our simulations, studying their characteristics is straightforward, because we can directly extract information such as position, velocity, mass, and chemical abundances for each member of these clusters and associations from our simulations. Furthermore, by utilizing different snapshots with a $\sim$ 1 Myr timestep of our simulations, we can track the evolution of the identified stellar groups over time. This comprehensive approach allows for a detailed exploration of the dynamical and chemical properties of stellar structures in our simulated galaxies.

In Section 6.2, we describe the *Latte* suite of FIRE-2 Milky Way-mass galaxy simulations, and we explain how we identify star clusters and associations in these simulations. In Section 6.3, we present our analysis, which includes an exploration of the parameter space traversed by our FoF algorithm. Then, we focus on YMCs and YMAs with ages less than 3 Myr at identification and masses exceeding $\sim 10^{4.5}$ $M_\odot$ identified by a friends-of-friends algorithm with a linking length of 4 parsecs (that is the fixed gravitational softening for stars in the *Latte* suite of FIRE-2 Milky Way-like galaxy simulations [217]). We provide data on various properties, such as boundedness, mass, size, 1D velocity dispersion, and the spread in metallicity [Fe/H] and age, for these identified YMCs and YMAs. Furthermore, we conduct comparative analyses of these properties for these YMCs and YMAs between default-physics-run simulations and magneto-hydrodynamics re-runs of the same simulations. Moreover,

we delve into the implications of our findings and compare them with observational results to assess the capability of the *Latte* suite of FIRE-2 simulations to replicate realistic star clusters and associations and their properties.

6.2 Methods

6.2.1 *Latte* Suite of FIRE-2 Simulation

Cosmological "zoom-in" simulations model a specific region at high resolution within a cosmological background at lower resolution. Some examples of these simulations include the work of Katz and White in 1993 [110] and Oñorbe et al. in 2014 [154]. With recent progress, the current version of cosmological galaxy zoom-in simulations can resolve individual star-forming regions within galaxies. In addition, various elements of stellar feedback are incorporated into the current generation of simulations. These together allow the creation of realistic stellar populations in simulations, which can then be compared with observations.

We analyze six cosmological "zoom-in" galaxy simulations from the *Latte* suite of FIRE-2 Milky Way-like simulations [217]. In particular, we select three galaxy simulations with the default (metal diffusion) physics runs `m12i` (first presented in [217]), `m12f` (first presented in [67]), and `m12m` (first presented in [102]) for this work. These simulations include gas, star, and dark matter particles and provide high spatial ($\sim$ 1 pc), initial star particle mass (7100 $M_\odot$), and temporal (1 Myr) resolution. The three simulations have different stellar and gas masses by a factor of 2. In [182], various characteristics of these simulations at reshift $z = 0$ are presented in tables and compared with the Milky Way. Their morphologies are also different (see [155] for details): the spiral structure of `m12f` is slightly perturbed, and m12m spirals are flocculent. Along with the default (metal diffusion) version of these simulations, we also analyze the magneto-hydrodynamics version of the same

Table 6.1: Properties of the MW and Simulated Galaxies.

Galaxy	N_*	M_* [$M_\odot$]	$R_{*,90}$ [kpc]	$Z_{*,90}$ [kpc]	$R_{*,e}$ [kpc]	$M_{\rm gas}$ [$M_\odot$]
`m12i`	9,000,000	5.5e10	8.6	2.1	2.7	0.8e10
`m12f`	11,000,000	6.9e10	11.9	2.1	3.4	1.2e10
`m12m`	15,800,000	1.0e11	11.6	2.3	3.2	1.5e10

N_*: number of star particles in the galaxy. M_*: stellar mass within the galaxy. $R_{*,90}$: radius that encloses 90% of stellar mass. $Z_{*,90}$: vertical height that encloses 90% of stellar mass. $M_{\rm gas}$: mass of gas within the galaxy. SFR: star-formation rate within the galaxy, averaged over the last 100 Myr.

simulations [99, 97, 207], `m12i-mhdcv`, `m12f-mhdcv`, and `m12m-mhdcv` to study the effects of magneto-hydrodynamics on the formation of YMCs and YMAs and their characteristics. The star formation rate (SFR) of each of these simulations across the latest 100 Myrs is shown in Fig. 6.1

These simulations are generated by using the FIRE-2 physics model [102] and the code Gizmo [96] that is a multi-method code to solve equations of hydrodynamics and gravity numerically. The code Gizmo solves the equations of hydrodynamics by utilizing a Lagrangian (move with the fluid flow) mesh-less finite-volume Godunov-type method. This method, in turn, allows continuous and automatic adaptive spatial resolution and deformation with the flow and simultaneously keeps mass, energy, momentum, and angular momentum conserved. To solve equations of gravity, the code Gizmo employs an enhanced Tree+PM solver adapted from GADGET-3 [205], incorporating fully adaptive and conservative gravitational force softening for gas to ensure matching hydrodynamic resolution. For simulations we aim to analyze in this chapter, the fixed gravitational force softening is 4 pc for stars and 40 pc for dark matter particles.

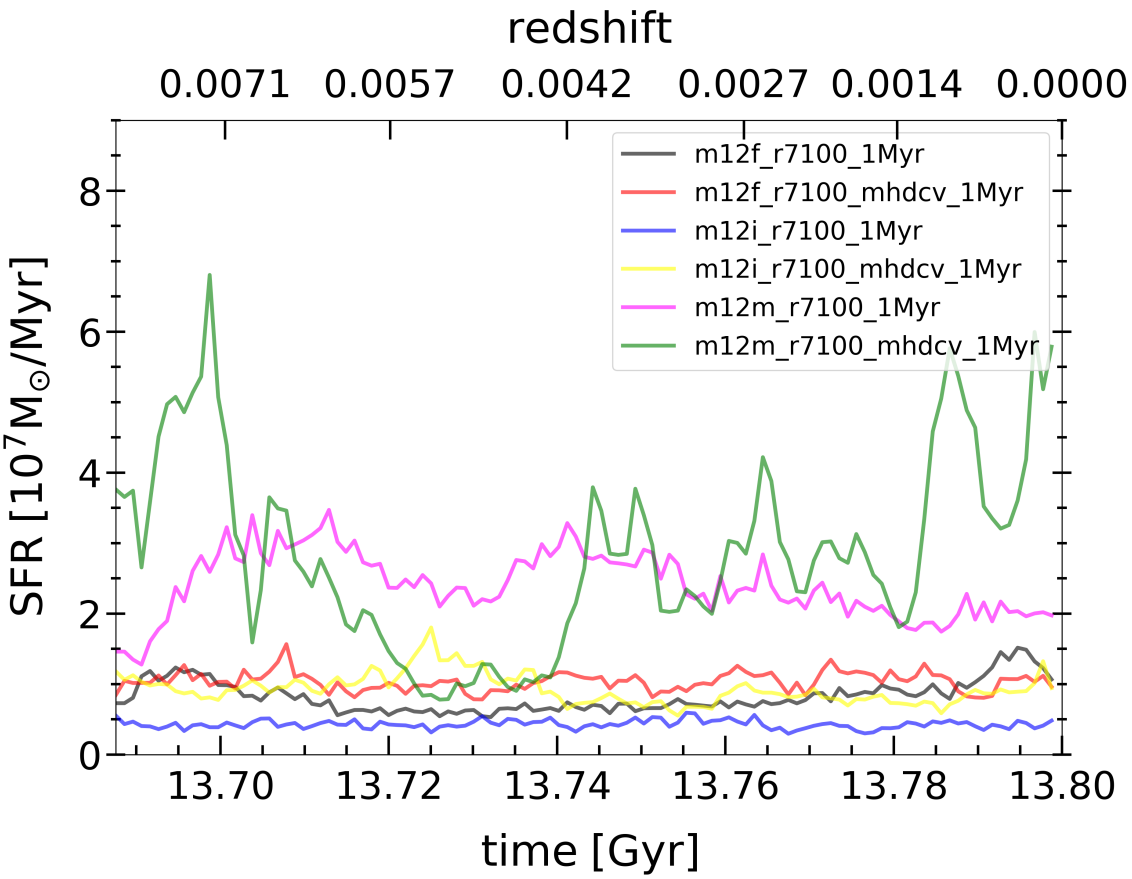

Figure 6.1: Star formation rate (SFR) of six different simulations, `m12f`, `m12i`, `m12m`, `m12f-mhdcv`, `m12i-mhdcv`, and `m12m-mhdcv`, across 100 Myrs (from redshift $z = 0.008$ to $z = 0$). For each simulation, SFR is computed for a region enclosed by $r_{spherical} < 20$ kpc and $|z| < 1.5$ kpc where $r_{spherical}$ is the spherical radial distance from the galactic center, and z is the vertical distance from the galactic midplane.

In these simulations, while accounting for a wide range of relevant gas heating and cooling mechanisms across $10 - 10^{10}$ K, different forms of stellar feedback—including type Ia and II supernovae [101], stellar winds (OB and AGB), photoionization, photoelectric heating, and radiation pressure in UV-through-IR [98]—are explicitly modeled based on standard stellar evolution models. For star formation, by leveraging a sink-particle approach in these simulations, gas turns into star under specific conditions: it must be locally self-gravitating (where potential energy exceeds thermal plus kinetic energy within the resolution scale), self-shielding (or 'molecular' as described in [122]), Jeans unstable (where thermal Jeans mass is below the maximum of the particle mass or $10^3 M_\odot$), sufficiently cold ($T < 10^4$ K), and above a dense threshold ($n > 1000$ cm^{-3}).

For the work presented in this chapter, we use a re-run of each of the six simulations `m12f`, `m12i`, `m12m`, `m12f-mhdcv`, `m12i-mhdcv`, and `m12m-mhdcv` covering 100 Myrs, from redshift $z = 0.008$ to $z = 0$. While the default cadence for snapshot output in the final 100 Myr of FIRE-2 simulations is ≈ 2 Myr intervals, for this work, we have generated a finer (1 Myr) cadence for the final 100 Myr. This increased precision allows for a more extensive exploration of the dynamical evolution of stellar groups.

6.2.2 Identifying Stellar Groups

We adopt a Friends-of-Friends (FoF) algorithm [57] to identify star clusters and associations [52, 136, 19]. We choose the FoF algorithm from various clustering algorithms like KMeans, Spectral, Ward, OPTICS, Birch, Gaussian mixture, DBSCAN, and HDBSCAN, because FoF is efficient in data sets containing a large number (several hundred million) of stars and can identify star clusters and associations even with irregular shapes. Additionally, FoF works well for our study as there are no errors in the positions or distances of stars in galaxy simulations.

For our analysis, we select all stars with an upper bound for their ages $\leq 3-25$ Myrs—to ensure identifying truly conatal populations—from the galactic disk from each snapshot of each of the six simulations `m12f`, `m12i`, `m12m`, `m12f-mhdcv`, `m12i-mhdcv`, and `m12m-mhdcv`. To select stars from the galactic disk, we apply the following criteria $r_{spherical} < 20$ kpc and $|z| < 1.5$ kpc, where $r_{spherical}$ is the spherical radial distance from the galactic center and z is the vertical distance from the galactic mid-plane. Then, we apply a FoF algorithm with a fixed linking length of $4-10$ pc to identify stellar groups (both bounds star clusters and unbound stellar associations). In this work, we explore how changing the linking length impacts the resultant properties of the star clusters we identify. We also set a minimum number of star particles per stellar group for identification; $\mathrm{n_{min}} = 5$ star particles, which is the minimum number that is statistically significant when calculating the standard deviation of a population [106]. This lower limit in combination with the average mass of a star particle in our simulations at birth (7100 $\mathrm{M_\odot}$) means that the lowest mass stellar groups we can resolve are $\gtrsim 10^{4.5}$ $\mathrm{M_\odot}$ (analogous to a massive star cluster in the MW).

6.2.3 Analyzing Identified Stellar Groups

For each stellar group, we measure its following characteristics: total stellar mass $\mathrm{M_{stellar\ group}}$, spatial size metrics $\mathrm{R_{50}}$ and $\mathrm{R_{90}}$[†], 1-dimensional velocity dispersion σ_{v1D}, and dispersion in age σ_{age}, and dispersion in metallicity $\sigma_{\mathrm{[Fe/H]}}$. In the following sections, we discuss if having stellar groups with small populations (as low as 5 stars) makes a significant impact on our results. In addition to the mentioned metrics, we analyze the boundedness of each stellar group. We use three different criteria to distinguish bound star clusters (YMCs) from unbound stellar associations (YMAs):

[†] R_{50} and R_{90} are two radial distances, measured from the center of mass of the stellar group, that contain 50 and 90 percent of its total mass, respectively. In particular, R_{50} is called the half-mass radius.

1. **Virial parameter:** The first criterion for the boundedness of a stellar group is called the virial parameter. It equals 2K.E./P.E., where K.E. is the sum of the kinetic energy of all stars within a stellar group, and P.E. is the total gravitational potential energy of the stellar group as a system. As we have the detailed knowledge of the mass, position, and the velocity of all individual stars from our simulations, we can directly compute the virial parameter. A stellar group is bound if its virial parameter < 1.

2. α_{90}**:** In observational studies, it is common to estimate the virial parameter by using the following equation [20]:

$$\frac{2K.E.}{P.E.} \approx \frac{5\sigma_{v1D}R_{90}}{GM} \tag{6.1}$$

where R_{90} is the radius that contains 90 percent of the total mass of the stellar group, G is the gravitational constant, and M is the total mass of the stellar group. We call the right-hand-side α_{90}.

$$\alpha_{90} \equiv \frac{5\sigma_{v1D}R_{90}}{GM} \tag{6.2}$$

Since we can compute σ_{v1D}, R_{90}, and M directly from simulation data, we can directly calculate the right-hand-side of Eq. 6.1. This allows to to check if the results of the two sides of Eq. 6.1 match.

3. α_{50}**:** In observational studies, it is also common to use a slightly different estimator of the boundedness. By replacing R_{90} with R_{50}, we have

$$\alpha_{50} \equiv \frac{5\sigma_{v1D}R_{50}}{GM} \tag{6.3}$$

where R_{90} the radius that contains 50 percent of the total mass of the stellar group.

We perform these steps on 100 snapshots (corresponding to the 100 Myr period preceding $z = 0$) of the six simulations. Then, for each simulation, we accumulate the stellar groups identified from multiple snapshots. To avoid double counting, in our statistical sample, depending on the fixed value of age, we skip an appropriate number of snapshots. This allows us to create a statistical sample with a larger number of stellar groups for each simulation and potentially sufficient for statistical analysis. For instance, if the age of stars is set to 3, we create our statistical samples from snapshots n, n+3, n+6, ..., up to the last snapshot.

6.3 Results

6.3.1 Number of Identified Stellar Groups

We can now show the number of identified stellar groups accumulated across 100 snapshots for each pair of an upper age limit and a fixed linking length for each simulation. Here we showcase the results in Fig. 6.2 for only one simulation, `m12f`. Results for the other simulations are in Appendix A.

From Fig. 6.2, we can see that the number of stellar groups from 100 snapshots of `m12f` varies—with both the upper age limit and the linking length—between 74 and 1195. Moreover, this figure depicts two evident trends.

First, the number of identified stellar groups in our accumulated sample is smaller for larger upper age limits, because for larger upper age limits we stack stellar groups from a smaller number of snapshots. As explained in 6.2.2, for instance, for the upper age limit of 3 and 25 Myrs, we stack stellar groups from 34 and 4 snapshots, respectively, to avoid double counting. Therefore, it should be noted that our accumulated sample is biased when we compare two samples of two different upper age limits.

Second, for any fixed upper age limit, the number of identified stellar groups in our accumulated sample is greater for larger linking lengths. For instance, for the

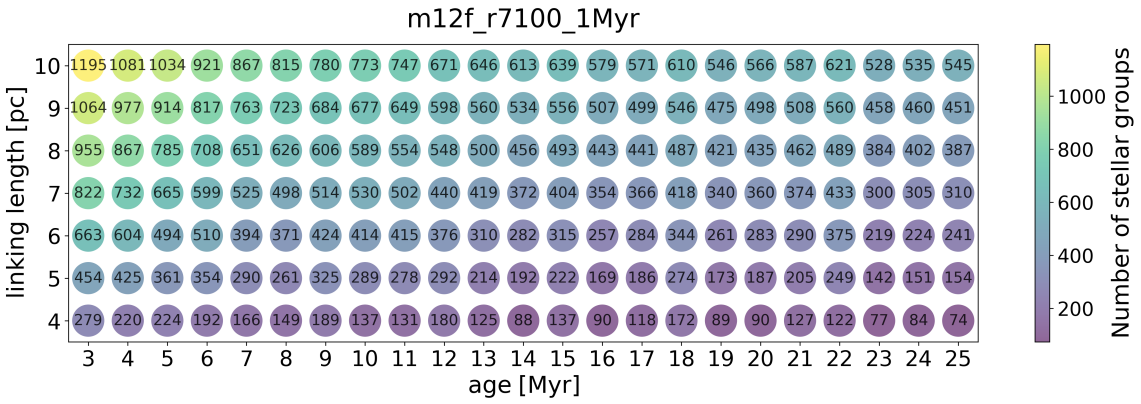

Figure 6.2: Number of identified stellar groups (both bound and unbound) for each pair of an upper age limit and a fixed linking length in `m12f`. Both the color and the numbers inside the points show the number of stellar groups that we have accumulated from 100 snapshots of `m12f`.

upper age limit of 3 Myrs, we have 279 and 1195 identified stellar groups for the two linking lengths of 4 pc and 10 pc.

Looking at Fig. A.1 and Fig. A.2, in Appendix A, it is easy to recognize that our accumulated samples for the other five simulations, follow the same trends.

6.3.2 Boundedness

In this subsection, we focus on analyzing boundedness where the upper limit for the age is in the range $3 - 25$ Myrs and the linking length is set to 4 pc. The result is shown in Fig. 6.3

By comparing the three panels of Fig. 6.3, we can see an identical pattern for each simulation; the larger upper age limit, the larger boundedness ratio. But, we should notice that (i) for estimation boundedness, α_{50} is not as strict as α_{90} and the virial parameter, and (ii) the virial parameter is the most strict criterion in compare with α_{50} and α_{50}, and (iii) the ratio of boundedness estimated by α_{90} and the virial

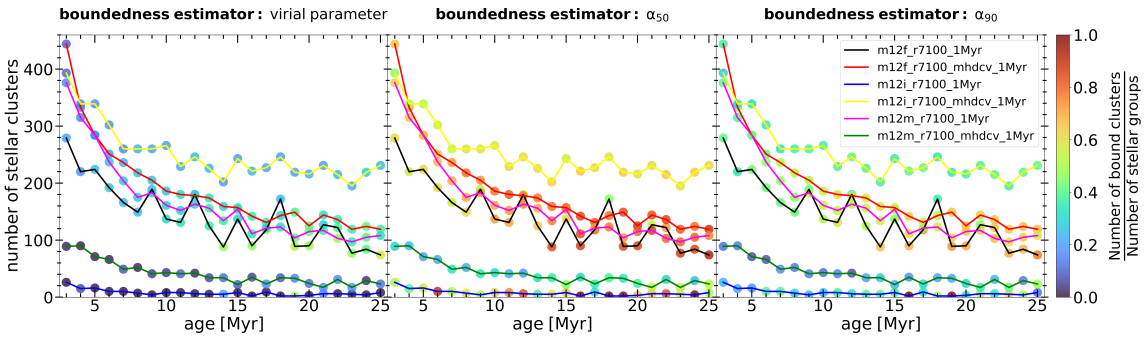

Figure 6.3: Depicting how the number of identified stellar groups and the boundedness ratio change in response to the upper age limit. The boundedness ratio is defined as the number of identified bound clusters divided by the total number of identified stellar groups (including both bound and unbound). The results are shown for a fixed linking length of 4 pc and six different simulations, `m12f`, `m12i`, `m12m`, `m12f-mhdcv`, `m12i-mhdcv`, and `m12m-mhdcv`, as indicated in the legend.

parameter are similar but slightly different.

In addition, we see that the number of identified stellar groups and the boundedness ratio for any specific upper age limit are almost the same for `m12f`, `m12f-mhdcv`, and `m12m`. In contrast, `m12i` and `m12m-mhdcv` have significantly smaller number of stellar groups, and the majority of their stellar groups are loose stellar associations. Interestingly, `m12i-mhdcv` has the highest number of stellar groups, and it seems for this simulation the boundedness ratio does not depend on the upper age limit.

6.3.3 Characteristics of Young Stellar Groups

Here, we focus on the most strict case where the upper limit for the age is 3 Myrs, and the linking length is set to 4 pc, and we analyze the stellar group metrics for each simulation. A fixed linking length of 4 pc equals the gravitational softening for stars in our *Latte* simulations, and the strict age requirement of ≤ 3 Myrs enables us to study YMCs and YMAs before the onset of type II supernovae, which typically

occur just after 3 Myr. We make this choice, because we want a pure sample of truly co-natal stars. For each stellar group metric, we include the histograms of all simulations in the same chart to make it easier to compare the results across the six different simulations. In Subsection 6.2.1, we mentioned that our simulations have different morphologies, different dynamical histories, and different amounts of stellar and gas contents (by a factor of 2), so these plots can help us to see whether the mentioned differences among these six simulations are reflected in the properties of their stellar groups or not.

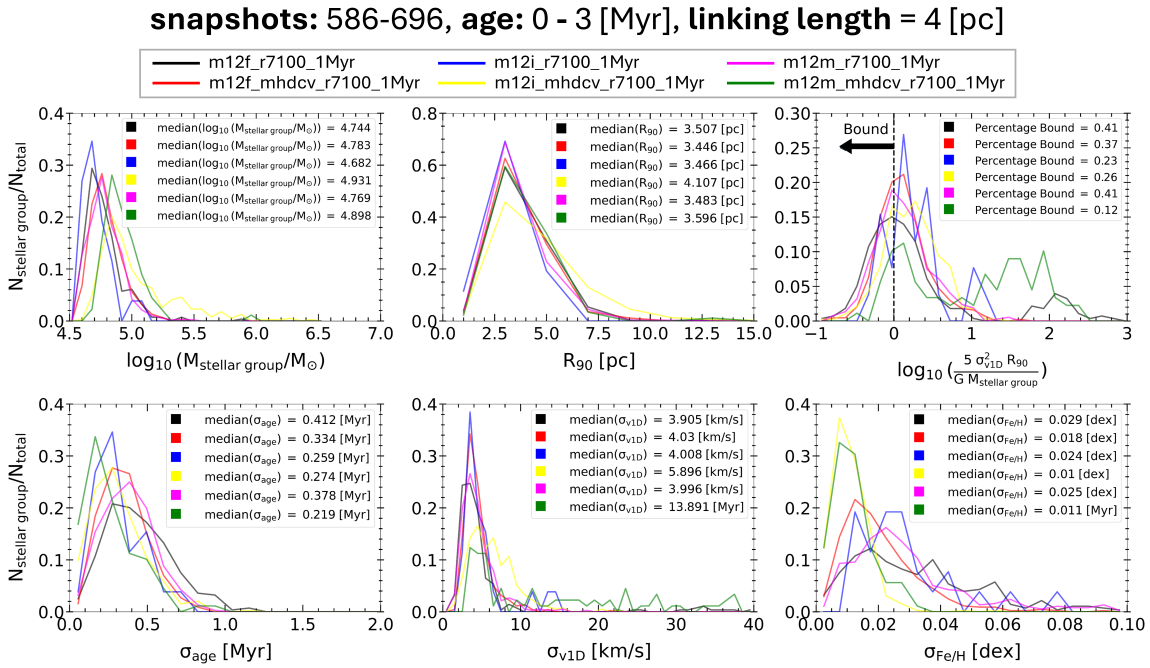

Figure 6.4: Each panel depicts histograms of one stellar group metric for all six simulations `m12f`, `m12i`, `m12m`, `m12f-mhdcv`, `m12i-mhdcv`, and `m12m-mhdcv`. The exact definition of each metric is given in Subsection 6.2.3. The medians of metrics, shown in legends, can be compared with the results of observational studies. Our identified stellar groups resemble realistic YMCs and YMAs.

Fig. 6.4 contains a large amount of information, which we will breakdown in

turn. The first two panels on the top row, total stellar mass $M_{\text{stellar group}}$ and spatial size metrics R_{90} of stellar groups, can help in evaluating whether simulated and observed stellar groups share similar properties. The $M_{\text{stellar group}}$ of the majority of stellar groups in our simulations are in the range $\sim 10^{4.5} - 10^{5.3} M_\odot$ with a median of $\sim 10^{4.7} M_\odot$. The lower bound of this range is the direct result of requiring to have at least 5 star particles in a stellar population to be considered as a stellar group. Almost all stellar groups in our simulation have R_{90} within the range $0.5 - 10$ pc with a median ~ 3.5 pc. The medians and ranges of these two metrics for stellar groups in *Latte* simulations fall within the range of values reported in observational studies (see Table 2 and Table 3 in Simon F. Portegies Zwart et al. (2010) [173]—both tables are included in B). In [173], Table 2 includes the properties of 4 YMCs and 7 YMAs observed in the Milky Way with ages ≤ 3.00 Myr; their stellar mass and virial radius are reported in the range $10^{3.80} - 10^{4.70} M_\odot$, $0.68 - 1.36$ pc, $10^{3.60} - 10^{4.40} M_\odot$, and $3.40 - 21.22$ pc, respectively. In the same paper, Table 3 includes the properties of one YMC and one YMA with ages ≤ 3.00 Myr observed in the local group—in particular, in large magellanic cloud, and small magellanic cloud, respectively. The stellar mass and virial radius of each of these young stellar groups are reported as $10^{4.78} M_\odot$, 2.89 pc, $10^{5.60} - 10^{4.40} M_\odot$, and 15.28 pc.

The third panel on the top row shows the distribution of α_{90} of the stellar groups, and the legends tell us what percent of stellar groups are bound clusters (vs. unbound stellar associations). Interestingly, for some simulations like `m12f` and `m12m` up to $\sim$ 40 percent of stellar groups are bound clusters, while for `m12m-mhdcv` only 12 percent of stellar groups are bound clusters, and for the other simulations ~ 30 percent of stellar groups are bound clusters. These differences in the ratio of boundedness across different simulations are most likely related to their differences in $M_{\text{stellar group}}$ and σ_{v1D}, because the histograms of R_{90} of all simulation are almost the same (have almost the same median and dispersion). The gravitational interactions between a group and its surroundings together with stellar feedback determine σ_{v1D} of the

stellar group, so the middle panel in the bottom row highlights the differences of the galactic disks of our simulations. Exploring these differences is important and interesting, but it goes beyond the scope of our study.

The two panels for $\sigma_{\rm [Fe/H]}$ and $\sigma_{\rm age}$ show that spreads in age and metallicity for all simulations are relatively small ($\sim 0.2 - 0.4$ Myrs in age and $\sim 0.01 - 0.03$ dex in metallicity) indicating that stellar group's members share a common birth origin and identical natal giant molecular cloud (GMC). This suggests our identified stellar groups are not predominantly populated with field stars, but this suggestion may not be valid if the GMC is homogeneous for [Fe/H]. Moreover, small $\sigma_{\rm [Fe/H]}$ in stellar groups suggests the possibility of assigning a specific metallicity to each group, such as the mean of [Fe/H] of its star members. However, further investigation is needed to determine if [Fe/H], along with other chemical abundances, can act as a unique identifier for each stellar group, supporting the concept of chemical tagging—i.e., identifying stars that were born together in the same stellar group by using only their present-day chemistry of star—(Bhattarai et al. 2024, in preparation).

We might also be interested in knowing about the distribution of the radial location of our identified stellar groups. In Fig.6.5, $\rm R_{cyl,\ stellar\ group's\ cm}$ is the radial distance between the center of mass of each stellar group and the galactic center in cylindrical coordinate. This plot tells us if stellar groups can be found across the entire galactic disk or if they can be found only near the galactic center where the gas density is typically high. Surprisingly, only the histogram of `m12m-mhdcv` has a peak near the galactic center. The stellar groups of `m12i-mhdcv` and `m12m-mhdcv` are predominantly formed in the inner and intermediate region of the galactic disk (within an annulus with $\rm R_{cyl,\ stellar\ group's\ cm}$ in the range $\approx 0 - 10$ kpc), and in contrast in `m12f`, `m12i`, `m12m`, and `m12f-mhdcv` the majority of stellar groups are formed in the outer regions (within an annulus with $\rm R_{cyl,\ stellar\ group's\ cm}$ in the range $\approx 10 - 20$ kpc) of the galactic disk.

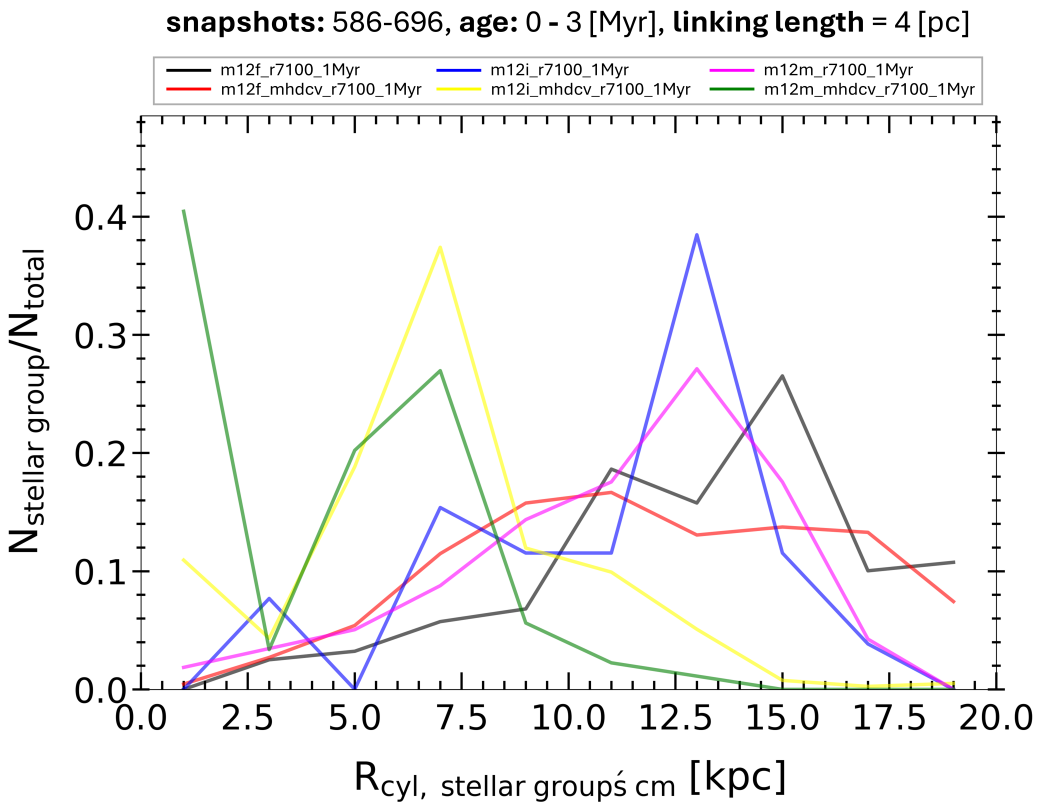

Figure 6.5: Histograms of the radial location of our identified stellar groups. $R_{\text{cyl, stellar group's cm}}$ is the radial distance between the center of mass of each stellar group and the galactic center in cylindrical coordinate.

6.3.4 The Impact of Changing Linking Length

In Subsection 5.5.3, we highlighted a significant drawback of FoF: its sensitivity to the choice of linking length. Here we check if changing the linking length has a significant impact on our measured stellar group metrics. In this subsection, we select stars with ages $\leq$ 3 Myrs, and compare the stellar group metrics for each simulation across different values for the linking length in the range $4 - 10$ pc. As our analysis of the all six simulations shows similar trends, here we showcase our results only for `m12f` depicted in Fig. 6.6. A catalog of all generated plots for all six

simulations for this subsection is in Appendix C.

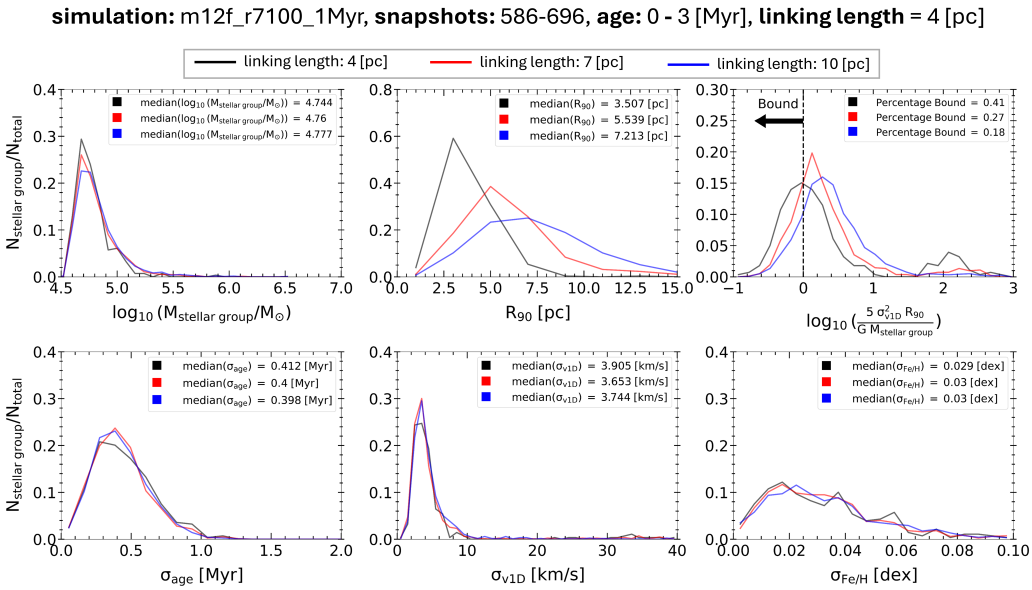

Figure 6.6: Each panel depicts histograms of one stellar group metric for `m12f`. These stellar groups have ages $0-3$ Myrs and are identified by using three different linking lengths 4, 7, and 10 pc. The exact definition of each metric is given in Subsection 6.2.3. The medians of metrics, shown in legends.

By using a larger linking length, we expect (i) to identify more stellar groups, and (ii) to have more stellar groups with larger spatial sizes, for obvious reason. From 6.2, we know that for the upper age limit of 3 Myrs and the linking lengths of 4, 7, and 10 pc, the number of stellar groups equal 279, 822, and 1195. This confirms our first expectation. From middle panel from the top row of Fig. 6.6, we can see that by changing the linking length the peak of the distribution shifts towards larger values for R_{90} confirming our second expectation. The legend shows that the by changing linking length form 4 to 10 pc, the median of R_{90} increase from ~ 3.5 to ~ 7.2 pc.

Interestingly, from the left panel of the top row and the three bottom row panels of Fig. 6.6, it can be easily seen that changing the linking length form 4 to 10 pc has only

a very minimal impact on both distributions and the medians of $M_{\text{stellar group}}$, σ_{age}, σ_{v1D} and $\sigma_{\text{[Fe/H]}}$. This mitigates concerns about the sensitivity of FoF to the choice of linking length for these four stellar group metrics, and dispersion in metallicity $\sigma_{\text{[Fe/H]}}$, and ensures the robustness of our results discussed in Subsection 6.3.3.

Having larger R_{90} but almost the same $M_{\text{stellar group}}$ and σ_{v1D} for stellar groups identified by using a larger linking length, means catching more unbound loose associations. It is reflected in the right top panel of Fig. 6.6; by increasing the linking length form 4 to 10 pc, the ratio of boundedness drops form 0.41 to 0.18.

6.3.5 Probing Possible Corealtions

In this subsection, we examine a potential correlation between the cylindrical radial position of our identified stellar groups, their status of boundedness, and their stellar mass. In other words, we want to answer three questions:

1. Is there a correlation between the status of boundedness of stellar groups and their total stellar mass $M_{\text{stellar group}}$?

2. Is there a correlation between the status of boundedness of stellar groups and their cylindrical radial locations $R_{\text{cyl, stellar group's cm}}$?

3. Is there a correlation between the total stellar mass of stellar groups $M_{\text{stellar group}}$ and their cylindrical radial locations $R_{\text{cyl, stellar group's cm}}$?

We perform our analysis for the fixed linking length of 4 [kpc], and the upper age limit of 3 Myrs.

Fig. 6.7 depict our results for `m12f`. For each column, we have leveraged a different boundedness estimator. As we see, for any choice of boundedness estimator, both bound clusters (asterisks) and unbound associations (dots) appear across almost the same range of stellar mass and radial position implying that there is no

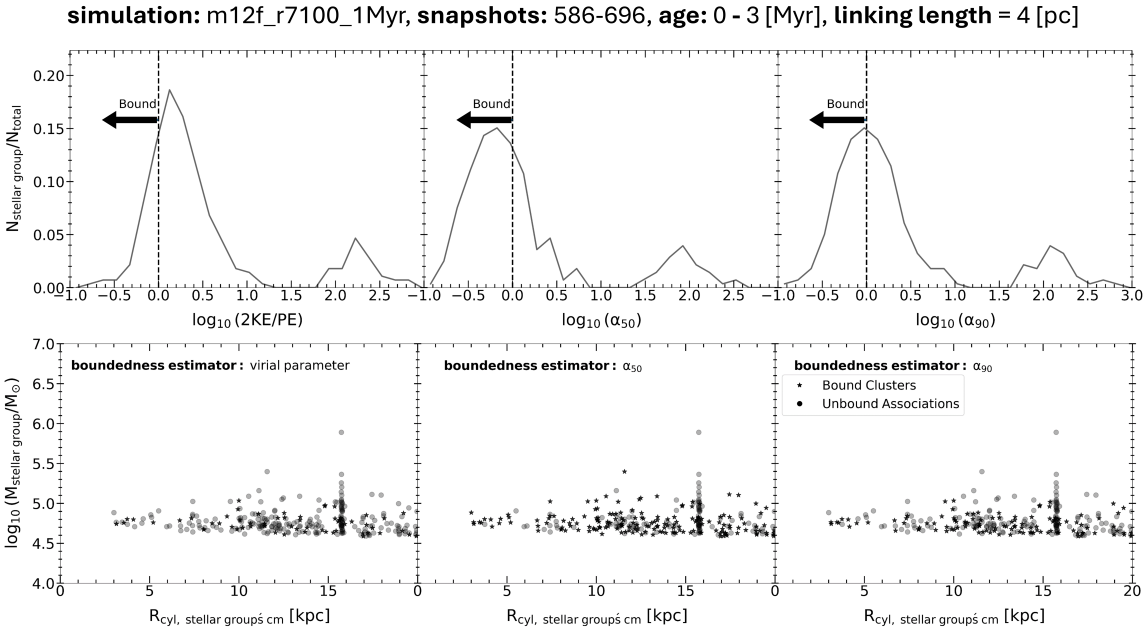

Figure 6.7: Cylindrical radial position of identified stellar groups (both bound and unbound) in `m12f` and their total stellar mass. The upper age limit is 3 Myrs and linking length is 4 pc. Asterisks show bound clusters and dots represent unbound associations. There is no specific correlation among the status of boundedness, $M_{\text{stellar group}}$ and $R_{\text{cyl, stellar group's cm}}$.

correlation between any pair of the following three metrics: the status of boundedness, $M_{\text{stellar group}}$, and $R_{\text{cyl, stellar group's cm}}$. The result of our analysis on `m12i`, `m12m`, `m12f-mhdcv`, `m12i-mhdcv`, and `m12m-mhdcv` is the same. A catalog of all generated plots for all six simulations for this subsection is in Appendix D.

6.4 Summary and Conclusion

We identify and measure different characteristics of stellar groups with ages $0-3$ Myrs, predating supernova feedback, in cosmological zoom-in simulations. We find that our measured characteristics, with the exception of R_{90} and boundedness, are

not sensitive to the choice of linking length within the range of $4-10$ pc for FoF. We find that the properties of our identified stellar groups are within the range of values reported in observational studies. We find that $12-41$ percent of our identified stellar groups are bound clusters, and it can be ~ 80 percent if we include stars with ages $0-25$ Myrs. We do not recognize any correlation between the status of boundedness of stellar groups, their cylindrical radial distance from the galactic center, and their stellar mass.

To find the optimized value for the linking length, it is essential to explore a broader range of lengths. We are planning to extend our analysis for linking lengths of $20-100$ pc. We are also planning to investigate the impact of type II supernovae on our identified stellar groups by tracking our stellar groups at snapshots when their ages falls within $3-6$ Myrs. Moreover, we are planning to generate new re-run simulations to explore the impact of individual channels of stellar feedback on formation, properties, and evolution of stellar groups. In addition, the forthcoming project will focus on generating synthetic images of our identified stellar groups and measure different characteristics of our stellar groups by utilizing the methods used in observational pipelines. This will make a more consistent comparison between simulations and observations.

Chapter 7

Conclusion

7.1 Quark Confinement

The first part of this thesis addresses the unsolved problem of quark confinement [153]; why quarks can never be found as free particles in isolation. Quark confinement is a fundamental puzzle within the realm of quantum chromodynamics (QCD), the theory governing the strong nuclear force in particle physics. Quark confinement dictates that quarks, the building blocks of hadrons like protons and neutrons, can never exist in isolation but are eternally bound within color-neutral structures called hadrons. While experiments and lattice gauge theory-computer simulations show that quark confinement is a real phenomenon, the exact mechanism of quark confinement is still an open question in QCD. This problem is tightly connected to the Yang-Mills mass gap problem [107], which is an open Millennium problem[†] .

The AdS/QCD conjecture, an offspring of the broader gauge/gavity duality [140], intertwines anti-de Sitter space (AdS), a spacetime construct from string theory, with QCD that explains the strong nuclear force. This conjecture indicates that string theory has some crucial similarities with QCD so that we can use string theory

[†] See https://www.claymath.org/millennium/yang-mills-the-maths-gap/

to solve problems in QCD. Leveraging the AdS/QCD correspondence, my research unravels the intricate connection between quantum field theory and string theory, aiming to illuminate this perplexing phenomenon. In this framework, quark confinement emerges as a string-theoretic concept. As quarks move apart, a 'string' forms between them, akin to a flux tube, exerting a linearly rising potential energy. This acts as an invisible force, forever binding the quarks.

In the quest to unveil quark confinement, we propose to utilize AdS/QCD to study the creation of quarks in the vacuum due to the presence of an external electromagnet field (EMF). In quantum electrodynamics (QED), it is known that external strong fields render the vacuum unstable, generating electron-positron pairs, a phenomenon known as the Schwinger effect [199] that is on the verge of being experimentally tested.

Although the Schwinger effect was first addressed in QED, it is relevant to other quantum field theories (QFTs) like QCD. The Schwinger effect explains how electrons and positrons come to exist if the vacuum gets exposed to external EMFs, and it is natural to ask if EMFs could also cause other fundamental charged particles such as quarks to appear out of emptiness. The Schwinger effect is thoroughly investigated in QED at the weak-coupling condition and weak-field approximation $eE << {m_e}^2$ [1], where e is the elementary charge, E is the electric field strength, and m_e is the electron rest mass. In contrast, there are ongoing theoretical efforts to explore this remarkable effect in QFTs like QCD, whose coupling constants are large [112].

As "quark confinement" and "quark and antiquark pair creation" are closely related, the standard QCD apparently cannot help us to study the Schwinger for quark and antiquark pairs. In addition, the standard formalisms of QFTs are based on perturbation theory, while the Schwinger effect is an intrinsically non-perturbative phenomenon. Thus, it is essential to employ an approach beyond the well-studied standard perturbative QFTs to study this effect. Our research aims to leverage AdS/QCD as an indirect approach, to probe the response of QCD and, in general,

QFTs with large coupling constants called SU(N) gauge field theories to an external EMF.

In Chapter 1, we explained the mysterious problem of quark confinement. In Chapter 2, we described how the Schwinger effect can provide an experimental setup to get a better understanding of the confinement mechanism of quarks. In addition, we discussed the potential for experimental verification of the Schwinger effect using X-ray free-electron lasers (XFELs). In Chapter 3, we introduced the gauge-invariant Wilson loop as an essential tool to compute the pair production rate. Finally, in Chapter 4, we showed that a form of gauge/gravity duality known as AdS/QCD can provide valuable insight to the confinement mechanism.

7.1.1 Contribution

The contribution of this thesis to the field of quantum field theory is presented in Chapter 4. We used AdS/QCD correspondence to thoroughly investigate the Schwinger effect in a QCD-like gauge theory (a.k.a. confining field theory) to a constant homogeneous electromagnetic field. AdS/QCD is a form of gauge/gravity duality —where the AdS side stands for gravity (string theory) and the QCD side refers to gauge theory (particle physics).

Numerous studies have investigated various aspects of the Schwinger effect in different systems, including confined systems [186, 187, 184, 26, 185, 111, 64, 69, 224, 112, 202]. However, many other aspects, particularly the impact of the simultaneous presence of electric and magnetic fields on quark and antiquark pair production, remain unknown. In our research, we not only studied the impact of an electric field but also thoroughly examined the effect of the simultaneous presence of a magnetic field and an electric field on the Schwinger effect for quark and antiquark pairs. The latter case (scenario) is our main contribution to enhance our understanding of this complex effect and, in turn, quark confinement.

7.1.2 Results

We used a deformed AdS_5 metric —for the gravity side of AdS/QCD— with three deformation functions; the quadratic function, the logarithmic function, and the function with both quadratic and logarithmic terms. Employing this metric, we determined the two critical electric fields E_s and E_c as lower and upper bounds of a range in which pair production can occur only by tunneling through a potential barrier. We showed that below E_s, the potential barrier is insurmountable, and pair production cannot happen. In contrast, above E_c, there is no potential barrier to restrict the pair production. We also found the total potential of a system composed of a pair of a virtual quark and antiquark in the presence of an external electromagnetic field through extremizing the action of a string attached to a D3-brane. By comparing results across three deformation functions, we found that the potential that quarks face is smaller in the case of the theory with a quadratic deformation function. The theories with only logarithmic and then with both logarithmic and quadratic functions have larger potential barriers, respectively.

In addition to potential analysis, we used calculation of the pair-production rate and showed that the two approaches agree. We computed the pair production rate Γ of quarks and antiquarks by utilizing a holographic prescription. From quantum field theory, we know that the circular Wilson loop can be used to compute the pair production rate. This approach, according to a holographic prescription, corresponds to extremizing the NG action of a string whose world-sheet ends on the boundary of the circular Wilson loop. As we know how to do the calculations on the AdS side, we can compute the pair production rate.

We have also examined the case of the simultaneous presence of electric and magnetic fields. We found that the presence of a pure perpendicular magnetic field (i) increases the value of both critical electric fields, meaning that the Schwinger effect begins at a higher electric field, and (ii) suppresses the creation rate of the quarks for

a given electric field above E_s. We discussed that these results agree with the results obtained by calculating the imaginary part of the DBI action of a probe D7-brane equipped with an electromagnetic field strength [88]. In contrast, the results of the leveraged approach in our study and the D7-brane approach are inconsistent for a pure parallel magnetic field. We found that a pure parallel magnetic field does not change the critical electric fields $\mathrm{E_s}$ and $\mathrm{E_c}$. On the contrary, the D7-brane approach concludes that a parallel magnetic field —without any impact on $\mathrm{E_s}$— enhances the creation rate of the quarks at a given electric field. We discussed that this inconsistency likely arises because the string world-sheet and DBI action represent different ways of approximating string theory, with certain corrections being overlooked in the DBI action.

To complete our investigation, we also explored the response of the system to the increase of $B_\parallel$ when $B_\perp$ is also present with a fixed value. When this happens, $B_\parallel$ makes the production rate go up, just like what can be found with the D7-brane setup. But, here is the twist: as $B_\parallel$ keeps increasing, the production rate, represented by Γ, keeps going up too, until eventually, when $B_\parallel$ goes to infinity, Γ settles at a fixed value, which turns out to be the same as when there is no magnetic field at all. The only effect of the increase of $B_\parallel$ is to compensate for the decrease of Γ due to the presence of $B_\perp$.

In summary, according to the string method, there's no better chance of creating quarks with magnetic fields, and the highest production rates, denoted by Γ, happen when both $B_\parallel$ and $B_\perp$ are zero. But in the D7-brane method, it's a whole different story: you can boost the production rate as much as you want and make the Schwinger effect more noticeable by adding a magnetic field parallel to the electric one. This finding is crucial because the Schwinger effect is too faint to see with the strongest electric fields we can generate in today's labs, so any theoretical or experimental attempt to make this elusive effect visible needs careful examination.

7.1.3 Future Work

From an experimental perspective, although the Schwinger effect is yet to be experimentally verified, the recent developments in experimental facilities seem very promising in offering chances to know more about quarks and their behavior. For instance, the recent completion of the 12 GeV upgrade of the Continuous Electron Beam Accelerator Facility (CEBAF) at Jefferson Lab [†] offers new opportunities to explore the structure of nuclei, including the ability to image quarks in three dimensions. With the upgraded machine, it will be possible to explore how quarks interact, spin, and are distributed within protons and neutrons.

On the theoretical side, recent developments in QCD show that a direct approach, the Hamiltonian truncation method, can be utilized to investigate the non-perturbative regime of QFTs [93]. In our future research project, we plan to employ the Hamiltonian truncation method to investigate the pair production in an external EMF to verify the results presented in this thesis (derived by using AdS/QCD as an indirect approach).

7.2 Young Stellar Groups in Cosmological Simulations

The second part of this thesis aims to explore the potential of zoom-in cosmological simulations in generating realistic stellar groups. The Milky Way (MW) is our detailed galaxy laboratory, unraveling galaxy formation, stellar evolution, and feedback mysteries. Cutting-edge observations like Gaia, Pan-STARRS, LSST, Nancy Grace Roman Space Telescope (WFIRST), and various spectroscopic surveys promise to reveal the Milky Way's cosmic secrets. However, there's a critical challenge, a lack of cosmological theoretical models to interpret these data. Understanding how, why,

[†] See https://www.jlab.org/news/releases/jefferson-lab-completes-12-gev-upgrade

and when stars form in clusters and associations and their effects on their environment is a key to gaining a fundamental understanding of how the Milky Way's structure built up over time [173, 123]. My study aims to fill this gap by creating benchmarks for young stellar groups for survey-to-simulation comparisons. For this aim we use MW-like galaxy simulations with the highest resolution up to date, the *Latte* suite of FIRE-2 simulations [217, 102] to study the early stage of formation young stellar groups within a full cosmological setting.

In Chapter 5, we discussed about different components of the Milky Way and its structure, different types of stellar groups and their importance in astrophysics, and the essential role of simulations in developing modern astrophysics, as well as the value of one clustering tool, the FoF algorithm. Chapter 6 then presented the results of applying this clustering algorithm to identify and characterize young stellar groups in the *Latte* suite of FIRE-2 cosmological simulations.

7.2.1 Contribution

The contribution of this thesis to the field of astrophysics is presented in Chapter 6. The presented study is the first in a series of projects defined as a research program. The ultimate goal of this program is twofold: (1) to fill the gap in translating observations into astrophysical insights and (2) to connect the physics of different spatial scales, from the scale of relatively small stellar groups to the scale of giant molecular clouds and larger-scale structures like spiral arms.

It is essential to emphasize the ambitious nature of these goals. While we have a flood of observational data, we currently still do not have a rich understanding of how to interpret observations correctly and consistently. Most interpretations are based on theoretical models, while (i) there are often various models that produce similar results, and (ii) most of these models need to be verified, too. In addition to these challenges, in the context of astrophysics, the connection between the physics

of different scales is poorly understood because, at each scale, several mechanisms simultaneously come into play, and each of them is often a non-linear and chaotic mechanism.

To address these challenges, we use the *Latte* suite of FIRE-2 simulations—which are along Auriga [72], the only generated (up-to-date) cosmological zoom-in simulations of the Milky Way-like galaxies—to study different characteristics of young stellar groups that can be thought of as the building blocks of spiral galaxies. Characterizing young stellar groups allows us to provide a benchmark and a toolkit to translate observations into astrophysical insight about the formation and evolution of stellar groups within realistic galactic environments, from scales of pc to 10's kpc, all within a fully cosmological context.

In particular, the main goals of our study—presented in Chapter 6—are (1) to ensure we have reasonably realistic stellar groups in our simulations, and (2) to assess the efficiency and accuracy of the tools and methods we developed and utilized to identify and characterize young stellar groups. As our findings validate the realism of our simulated stellar groups and the effectiveness of our computational tools for identifying and characterizing these informative stellar structures, people in our collaboration can now proceed with the upcoming projects to reach the ultimate goals of this research program.

7.2.2 Results

In the study presented in Chapter 6, we examined various properties of stellar groups with ages $0-3$ million years in six Milky Way-like cosmological "zoom-in" simulations. Our findings indicate that many but not all the stellar groups' characteristics we measured remain consistent across linking lengths of $4-10$ parsecs for FoF. The properties of our identified stellar groups align with those observed in previous studies. About $12-41\%$ of stellar groups in *Latte* simulations are bound clusters,

increasing to approximately 80% when including stars with ages up to 25 million years. We observed no correlation between stellar groups' boundedness status, their radial distances from the galactic center, and their stellar masses.

7.2.3 Future Work

We need to explore a broader range of values for the linking length, from 20 to 100 parsecs, to determine the optimal linking length for the FoF algorithm. To assess the influence of type II supernovae on our stellar group, we need to track their evolution within the $3 - 15$ million-year age range. To investigate how individual channels of stellar feedback impact the surrounding medium and in turn formation, properties, and evolution of stellar groups, we need to generate "re-run" *Latte* simulations which are the same as the existing *Latte* suite, except individual channels of feedback will be turned on/off for the duration of the run. Our upcoming efforts will also involve generating synthetic images of identified stellar groups and analyzing their characteristics using methods akin to observational pipelines, facilitating a more consistent comparison between simulations and observations.

Appendix A

one simulation in each plot, age $\leq$ 3-25 Myrs, linking lengths: 4-10 pc

This Appendix includes all the plots of Subsection 6.3.1.

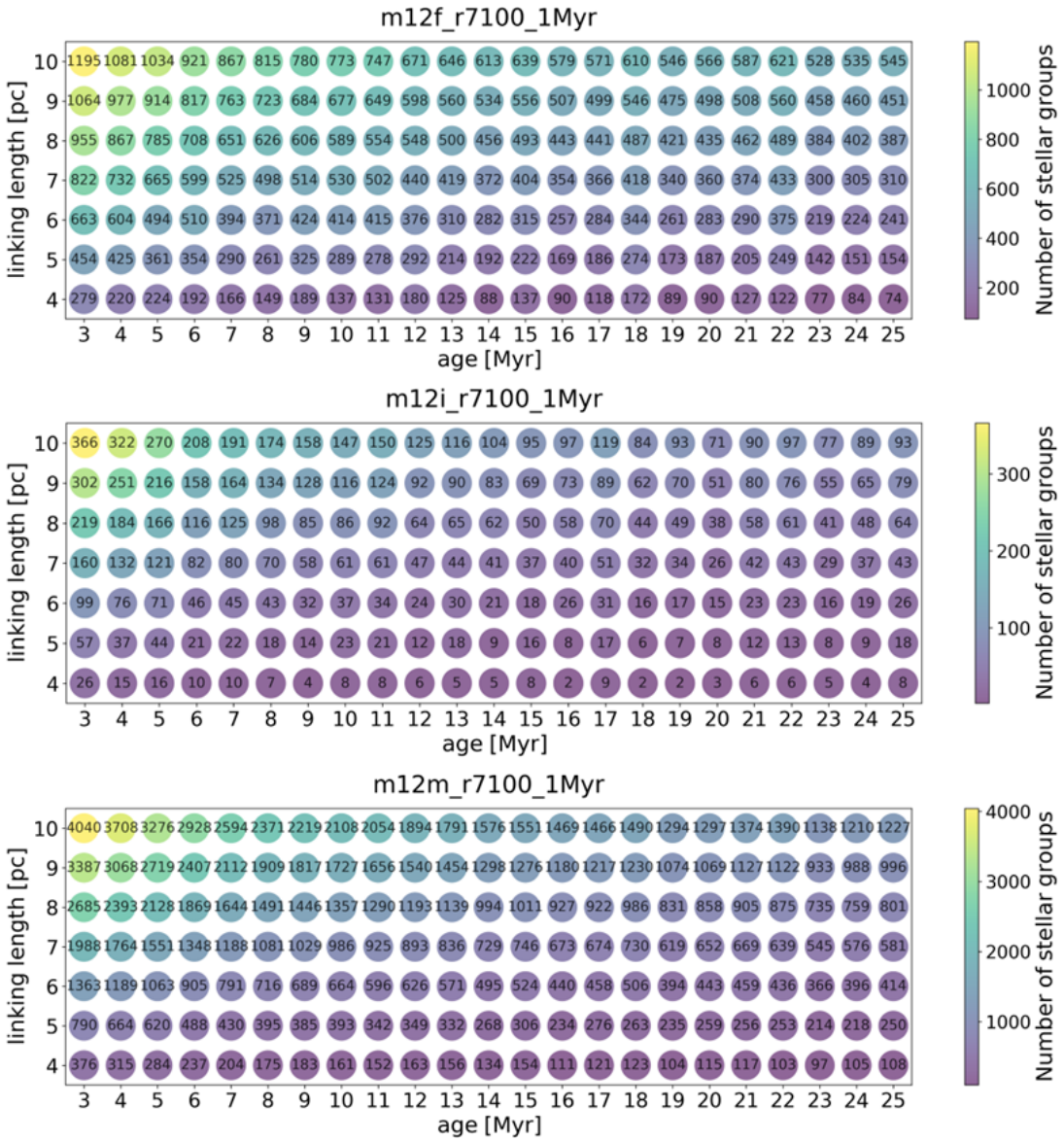

Figure A.1: Number of identified stellar groups (both bound and unbound) for each pair of an upper age limit and a fixed linking length in `m12f`, `m12i`, and `m12m`. Both the color and the numbers inside the points show the number of identified stellar groups that we have accumulated from 100 snapshots of `m12f`, `m12i`, and `m12m`.

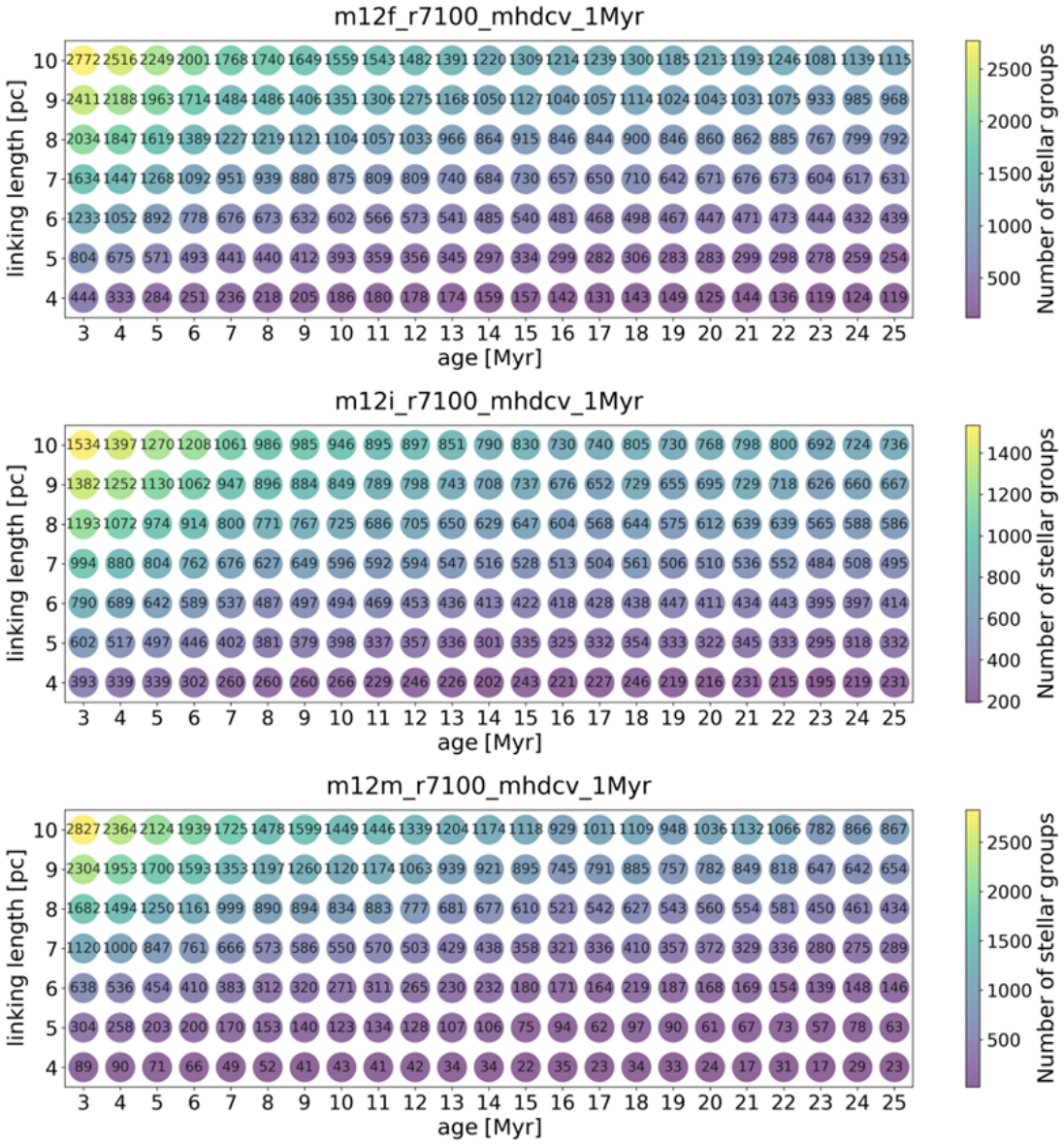

Figure A.2: Number of identified stellar groups (both bound and unbound) for each pair of an upper age limit and a fixed linking length in `m12f-mhdcv`, `m12i-mhdcv`, and `m12m-mhdcv`. Both the color and the numbers inside the points show the number of identified stellar groups that we have accumulated from 100 snapshots of `m12f-mhdcv`, `m12i-mhdcv`, and `m12m-mhdcv`.

Appendix B

Properties of YMCs and YMAs

This appedix includes Table 2 and Table 3 from Simon F. Portegies Zwart et al. (2010) [173].

Name	Ref	Age [Myr]	$\log M_{\rm phot}$	$\log M_{\rm dyn}$	$r_{\rm c}$ [pc]	$r_{\rm eff}$ [pc]	γ	$\sigma_{\rm 1D}$ [km s^{-1}]	$r_{\rm vir}$ [pc]	$t_{\rm dyn}$ [Myr]	Age/$t_{\rm dyn}$
Arches	1	2.00	4.30	–	0.20	0.40	–	–	0.68	0.06	33.86
DSB2003	2	3.50	3.80	–	–	1.20	–	–	2.04	0.55	6.41
NGC 3603	3	2.00	4.10	–	0.15	0.70	2.00	–	1.19	0.17	11.62
Quintuplet	4	4.00	4.00	–	1.00	2.00	–	–	3.40	0.93	4.29
RSGC 01	4	12.00	4.50	4.70	–	1.50	–	3.70	2.55	0.34	35.22
RSGC 02	5	17.00	4.60	4.80	–	2.70	–	3.40	4.58	0.73	23.18
RSGC 03	6	18.00	4.50	–	–	5.00	–	–	8.49	2.07	8.68
Trumpler 14	7	2.00	4.00	–	0.14	0.50	2.00	–	0.85	0.12	17.15
Wd 1	8	3.50	4.50	4.80	0.40	1.00	4.00	5.80	1.74	0.19	18.27
Wd 2	2	2.00	4.00	–	–	0.80	–	–	1.36	0.24	8.48
hPer	2	12.80	4.20	–	–	2.10	–	–	3.57	0.80	16.06
χPer	2	12.80	4.10	–	–	2.50	–	–	4.24	1.16	11.02
CYgOB	2	2.50	4.40	–	–	5.20	–	–	8.83	2.47	1.01
IC 1805	2	2.00	4.20	–	–	12.50	–	–	21.22	11.58	0.17
I Lac 1	2	14.00	3.40	–	–	20.70	–	–	35.14	61.97	0.23
Lower Cen-Crux	2	11.50	3.30	–	–	15.00	–	–	25.46	42.89	0.27
NGC 2244	2	2.00	3.90	–	–	5.60	–	–	9.51	4.90	0.41
NGC 6611	2	3.00	4.40	–	–	5.90	–	–	10.02	2.98	1.01
NGC 7380	2	2.00	3.80	–	–	6.50	–	–	11.03	6.88	0.29
ONC	9	1.00	3.65	–	0.20	2.00	2.00	–	3.40	1.40	0.72
Ori Ia	2	11.40	3.70	–	–	16.60	–	–	28.18	31.50	0.36
Ori Ib	2	1.70	3.60	–	–	6.30	–	–	10.70	8.26	0.21
Ori Ic	2	4.60	3.80	–	–	12.50	–	–	21.22	18.35	0.25
Upper Cen-Crux	2	14.50	3.60	–	–	22.10	–	–	37.52	54.30	0.27
U Sco	2	5.50	3.50	–	–	14.20	–	–	24.11	31.38	0.18

Table B.1: Properties of YMCs (top) and YMAs (bottom) in the Milky Way, with the distinction based on age/$t_{\rm dyn}$ (Ref. [173], Table 2). Highlighted rows show stellar groups with ages $\leq$ 3 Myr.

1: [63]; 2: [164]; 3: [86]; 4: [62]; 5: [46]; 6: [42]; 7: [11]; 8: [148]; 9: [92].

(1) Gal	(2) Name	(3) Ref	(4) Age [Myr]	(5) M_V [mag]	(6) $\log M_{\rm phot}$	(7) $\log M_{\rm dyn}$	(8) $r_{\rm c}$ [pc]	(9) $r_{\rm eff}$ [pc]	(10) γ	(11) $\sigma_{\rm 1D}$ [km s^{-1}]	(12) $r_{\rm vir}$ [pc]	(13) $t_{\rm dyn}$ [Myr]	(14) Age/$t_{\rm dyn}$
LMC	R136	1,2,3,4	3.0	−11.74	4.78	–	0.10	1.70	1.50	–	2.89	0.30	10.14
LMC	NGC 1818	2,3	25.1	−9.62	4.42	–	2.07	5.39	3.30	–	9.76	2.80	8.96
LMC	NGC 1847	2,3	26.3	−9.67	4.44	–	1.73	32.58	2.05	–	10.33	2.98	8.82
LMC	NGC 1850	2,3	31.6	−10.52	4.86	5.22	2.69	11.25	2.05	3.00	3.56	0.37	84.83
LMC	NGC 2004	2,3	20.0	−9.60	4.36	–	1.41	5.27	2.90	–	9.81	3.03	6.59
LMC	NGC 2100	2,3	15.8	−9.77	4.36	–	0.99	4.41	2.30	–	6.32	1.57	10.12
LMC	NGC 2136	2,3	100.0	−8.60	4.30	–	1.59	3.42	3.50	–	6.10	1.59	62.85
LMC	NGC 2157	2,3	39.8	−9.10	4.31	4.90	1.99	5.39	3.05	2.80	9.95	3.27	12.16
LMC	NGC 2164	2,3	50.1	−8.65	4.18	5.15	1.48	4.76	2.95	4.30	8.84	3.19	15.72
LMC	NGC 2214	2,3	39.8	−8.40	4.03	5.28	1.83	8.13	2.45	3.90	14.24	7.74	5.14
LMC	NGC 1711	2,3	50.1	−8.82	4.24	–	1.91	5.19	2.70	–	9.70	3.42	14.66
M31	KW246	5	75.9	−7.80	4.19	–	–	3.20	–	–	5.43	1.52	50.01
M31	B257D	6	79.4	−8.84	4.45	–	3.16	15.14	–	–	25.70	11.57	6.86
M31	B318	6	70.8	−8.76	4.38	–	0.19	6.61	–	–	11.22	3.62	19.57
M31	B327	6	50.1	−8.95	4.38	–	0.20	4.47	–	–	7.59	2.01	24.91
M31	B448	6	79.4	−9.20	4.58	–	0.20	16.22	–	–	27.54	11.05	7.19
M31	Vdb0	7	25.1	−10.00	4.85	–	1.40	7.40	–	–	12.56	2.49	10.07
M31	KW044/B325	5	58.9	−9.20	4.59	–	–	10.00	–	–	16.98	5.29	11.14
M31	KW120	5	87.1	−8.80	4.57	–	–	2.60	–	–	4.41	0.72	121.43
M31	KW208	5	56.2	−7.70	4.01	–	–	2.90	–	–	4.92	1.61	34.93
M31	KW272	5	53.7	−9.00	4.50	–	–	9.00	–	–	15.28	5.01	10.73
M31	B015D	6	70.8	−9.71	4.76	–	0.24	16.60	–	–	28.18	9.30	7.61
M31	B040	6	79.4	−9.00	4.50	–	0.55	12.88	–	–	21.87	8.57	9.27
M31	B043	6	79.4	−8.81	4.43	–	0.72	3.98	–	–	6.76	1.60	49.77
M31	B066	6	70.8	−8.43	4.25	–	0.38	6.76	–	–	11.48	4.35	16.29
NGC 6822	Hubble IV	8,9	25.1	−8.00	4.00	–	0.40	2.00	–	–	3.40	0.93	26.93
SMC	NGC 330	2,3	25.1	−9.94	4.56	5.64	2.34	6.11	2.55	6.00	11.17	2.92	8.60
M31	KW249	5	5.0	−10.50	4.30	–	–	13.50	–	–	22.92	11.58	0.43
M31	KW258	5	5.0	−9.90	4.05	–	–	3.40	–	–	5.77	1.95	2.57
M33	NGC 595	10	4.0	−11.40	4.50	–	–	26.90	–	–	45.67	25.87	0.15
M33	NGC 604	10	3.5	−12.60	5.00	–	–	28.40	–	–	48.21	15.78	0.22
SMC	NGC 346	11	3.0	-	5.60	–	–	9.00	–	–	15.28	1.41	2.13

Table B.2: Same as Table B.1, but for YMCs and YMAs in the Local Group (Ref. [173], Table 3). Highlighted rows show stellar groups with ages ≤ 3 Myr.
1: [105]; 2: [138]; 3: [146]; 4: [5]; 5: [213]; 6: [14]; 7: [158]; 8: [221]; 9: [40]; 10: [139]; 11: [180].

Appendix C

one simulation in each plot, age $\leq$ 3 Myrs, linking length: 4 pc

This Appendix includes all the plots of Subsection 6.3.4.

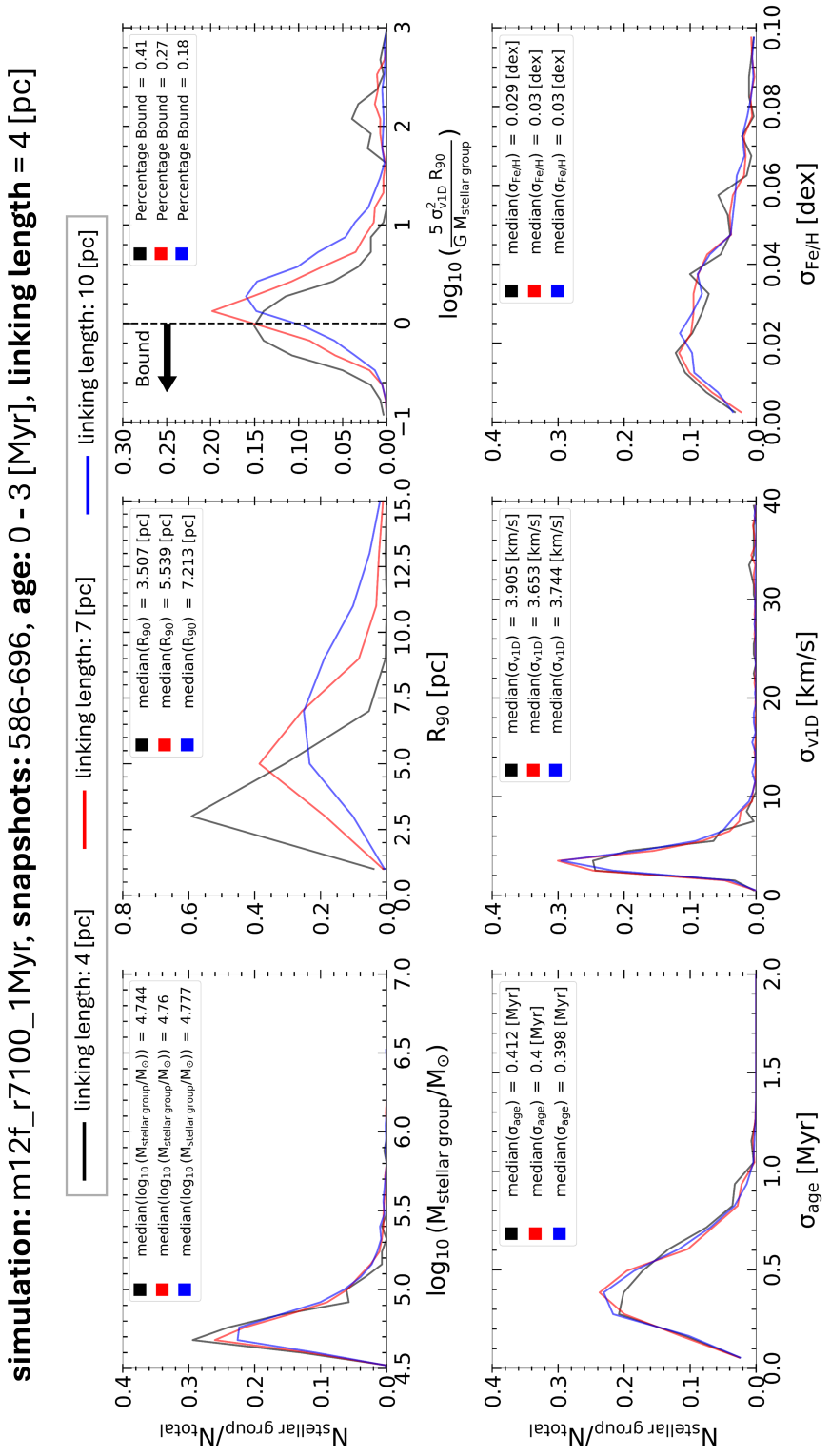
simulation: m12f_r7100_1Myr, snapshots: 586-696, age: 0 - 3 [Myr], linking length = 4 [pc]
linking length: 4 [pc]
linking length: 7 [pc]
linking length: 10 [pc]
median(log10 (Mstellar group/M⊙)) = 4.744
median(log10 (Mstellar group/M⊙)) = 4.76
median(log10 (Mstellar group/M⊙)) = 4.777
Nstellar group/Ntotal
log10 (Mstellar group/M⊙)
median(R90) = 3.507 [pc]
median(R90) = 5.539 [pc]
median(R90) = 7.213 [pc]
R90 [pc]
Bound
Percentage Bound = 0.41
Percentage Bound = 0.27
Percentage Bound = 0.18
log10 (5 σ²1D R90 / G Mstellar group)
median(σage) = 0.412 [Myr]
median(σage) = 0.4 [Myr]
median(σage) = 0.398 [Myr]
σage [Myr]
median(σ1D) = 3.905 [km/s]
median(σ1D) = 3.653 [km/s]
median(σ1D) = 3.744 [km/s]
σ1D [km/s]
median(σFe/H) = 0.029 [dex]
median(σFe/H) = 0.03 [dex]
median(σFe/H) = 0.03 [dex]
σFe/H [dex]

Figure C.1

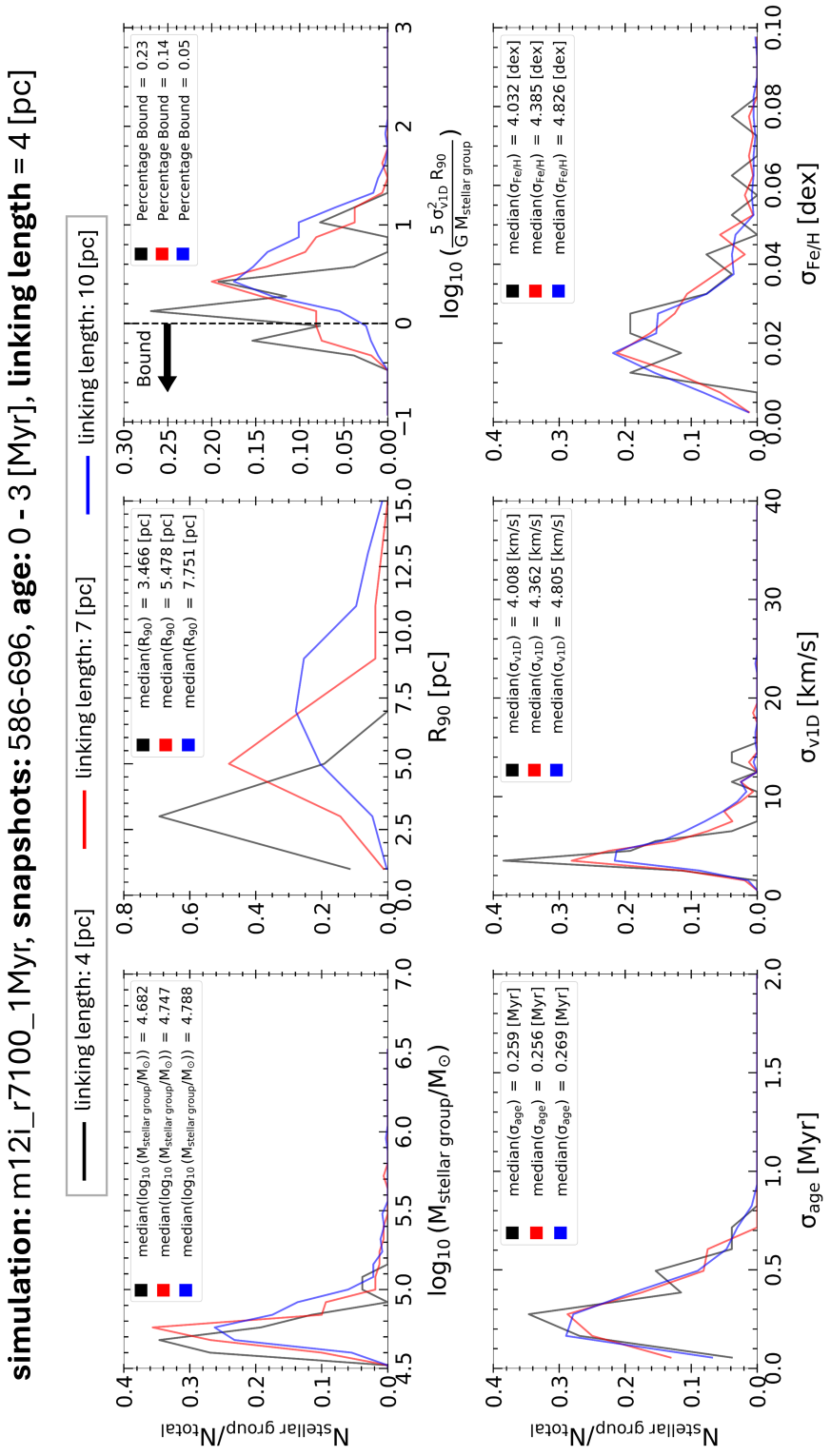
simulation: m12i_r7100_1Myr, snapshots: 586-696, age: 0 - 3 [Myr], linking length = 4 [pc]
linking length: 4 [pc]
linking length: 7 [pc]
linking length: 10 [pc]
median(log10 (Mstellar group/M⊙)) = 4.682
median(log10 (Mstellar group/M⊙)) = 4.747
median(log10 (Mstellar group/M⊙)) = 4.788
Nstellar group/Ntotal
log10 (Mstellar group/M⊙)
median(R90) = 3.466 [pc]
median(R90) = 5.478 [pc]
median(R90) = 7.751 [pc]
R90 [pc]
Percentage Bound = 0.23
Percentage Bound = 0.14
Percentage Bound = 0.05
Bound
log10 (5 σ2v1D R90 / G Mstellar group)
median(σage) = 0.259 [Myr]
median(σage) = 0.256 [Myr]
median(σage) = 0.269 [Myr]
σage [Myr]
median(σv1D) = 4.008 [km/s]
median(σv1D) = 4.362 [km/s]
median(σv1D) = 4.805 [km/s]
σv1D [km/s]
median(σFe/H) = 4.032 [dex]
median(σFe/H) = 4.385 [dex]
median(σFe/H) = 4.826 [dex]
σFe/H [dex]

Figure C.2

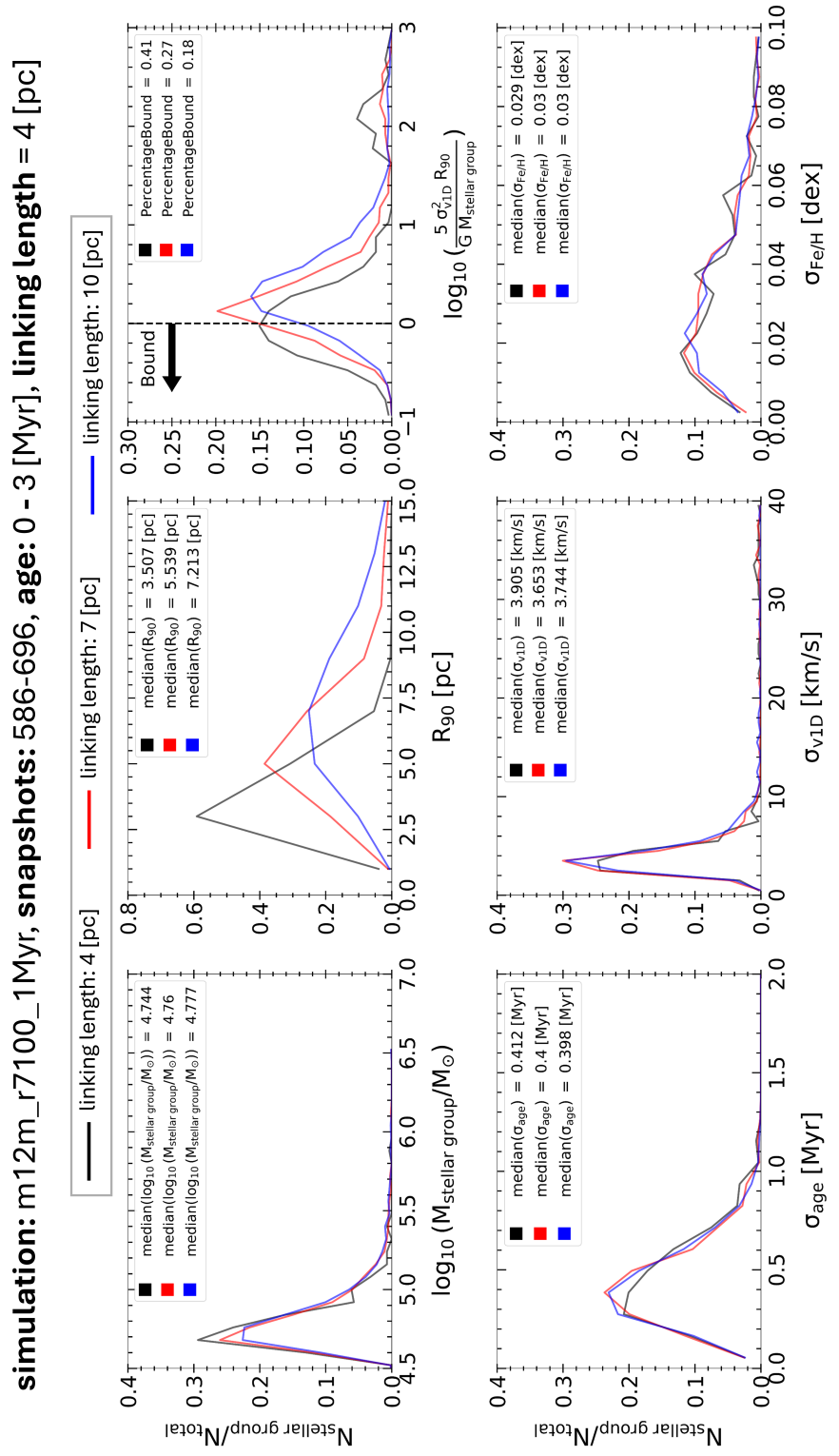
simulation: m12m_r7100_1Myr, snapshots: 586-696, age: 0 - 3 [Myr], linking length = 4 [pc]
linking length: 4 [pc]
linking length: 7 [pc]
linking length: 10 [pc]
median(log10 (Mstellar group/M⊙)) = 4.744
median(log10 (Mstellar group/M⊙)) = 4.76
median(log10 (Mstellar group/M⊙)) = 4.777
log10 (Mstellar group/M⊙)
median(R90) = 3.507 [pc]
median(R90) = 5.539 [pc]
median(R90) = 7.213 [pc]
R90 [pc]
PercentageBound = 0.41
PercentageBound = 0.27
PercentageBound = 0.18
Bound
log10 (5 σ²v1D R90 / G Mstellar group)
median(σage) = 0.412 [Myr]
median(σage) = 0.4 [Myr]
median(σage) = 0.398 [Myr]
σage [Myr]
median(σv1D) = 3.905 [km/s]
median(σv1D) = 3.653 [km/s]
median(σv1D) = 3.744 [km/s]
σv1D [km/s]
median(σFe/H) = 0.029 [dex]
median(σFe/H) = 0.03 [dex]
median(σFe/H) = 0.03 [dex]
σFe/H [dex]
Nstellar group/Ntotal

Figure C.3

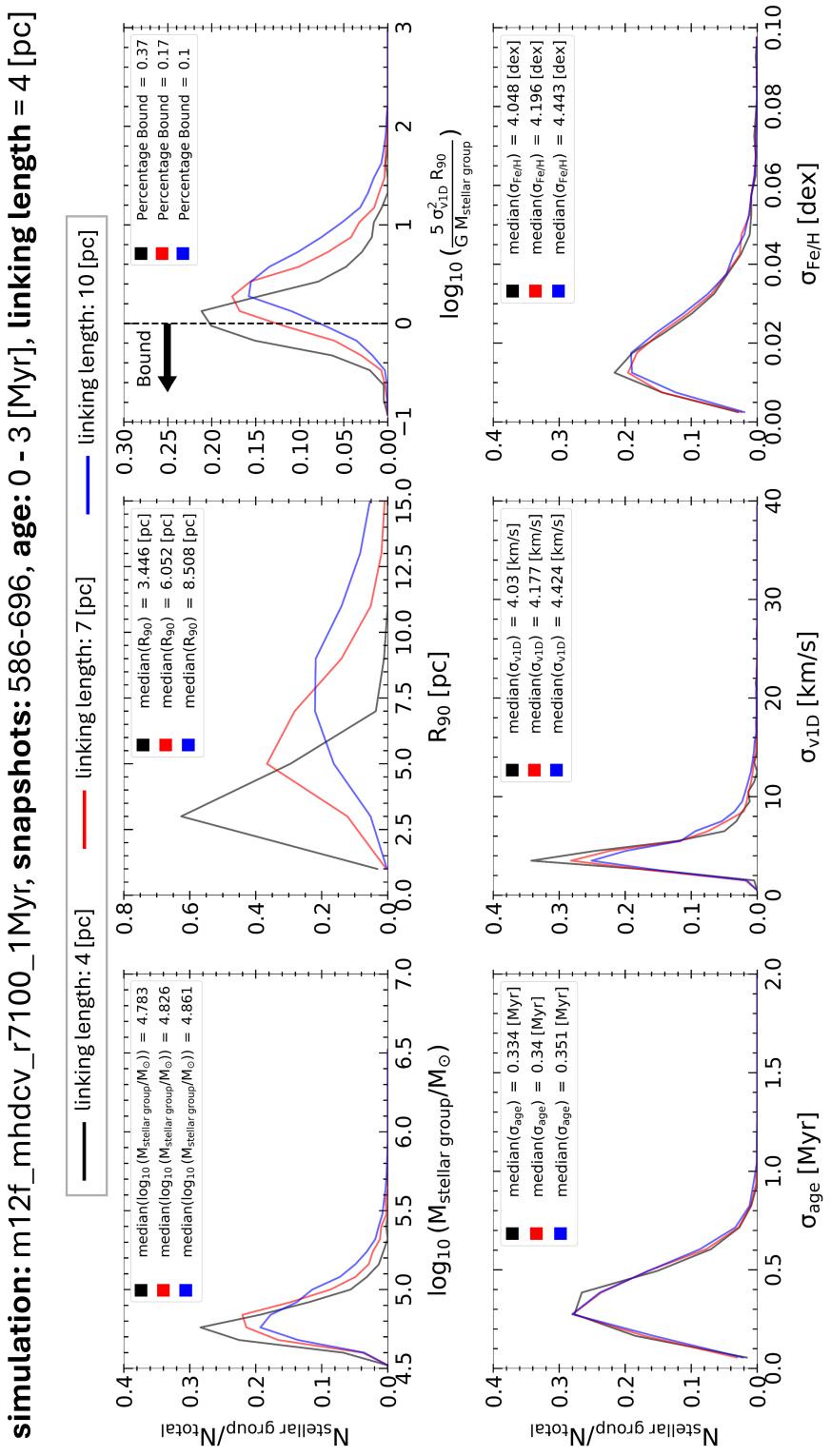
simulation: m12f_mhdcv_r7100_1Myr, snapshots: 586-696, age: 0 - 3 [Myr], linking length = 4 [pc]
linking length: 4 [pc]
linking length: 7 [pc]
linking length: 10 [pc]
median(log10 (Mstellar group/M⊙)) = 4.783
median(log10 (Mstellar group/M⊙)) = 4.826
median(log10 (Mstellar group/M⊙)) = 4.861
Nstellar group/Ntotal
log10 (Mstellar group/M⊙)
median(R90) = 3.446 [pc]
median(R90) = 6.052 [pc]
median(R90) = 8.508 [pc]
R90 [pc]
Percentage Bound = 0.37
Percentage Bound = 0.17
Percentage Bound = 0.1
Bound
log10 (5 σ²v1D R90 / G Mstellar group)
median(σv1D) = 4.03 [km/s]
median(σv1D) = 4.177 [km/s]
median(σv1D) = 4.424 [km/s]
σv1D [km/s]
median(σage) = 0.334 [Myr]
median(σage) = 0.34 [Myr]
median(σage) = 0.351 [Myr]
σage [Myr]
median(σFe/H) = 4.048 [dex]
median(σFe/H) = 4.196 [dex]
median(σFe/H) = 4.443 [dex]
σFe/H [dex]

Figure C.4

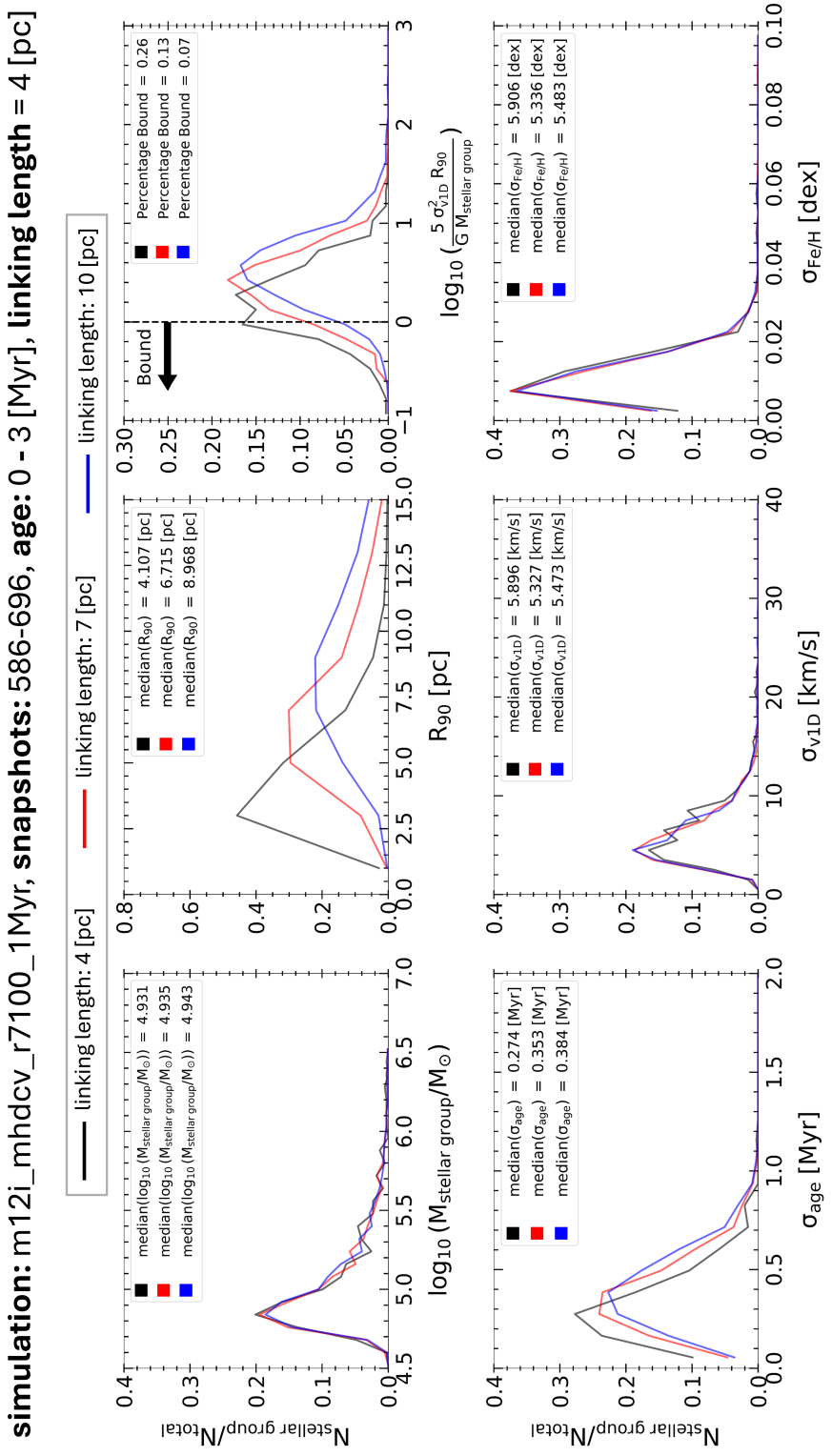
simulation: m12i_mhdcv_r7100_1Myr, snapshots: 586-696, age: 0 - 3 [Myr], linking length = 4 [pc]
linking length: 4 [pc]
linking length: 7 [pc]
linking length: 10 [pc]
median(log10 (Mstellar group/M⊙)) = 4.931
median(log10 (Mstellar group/M⊙)) = 4.935
median(log10 (Mstellar group/M⊙)) = 4.943
log10 (Mstellar group/M⊙)
median(R90) = 4.107 [pc]
median(R90) = 6.715 [pc]
median(R90) = 8.968 [pc]
R90 [pc]
Bound
Percentage Bound = 0.26
Percentage Bound = 0.13
Percentage Bound = 0.07
log10 (5 σ²v1D R90 / G Mstellar group)
median(σage) = 0.274 [Myr]
median(σage) = 0.353 [Myr]
median(σage) = 0.384 [Myr]
σage [Myr]
median(σv1D) = 5.896 [km/s]
median(σv1D) = 5.327 [km/s]
median(σv1D) = 5.473 [km/s]
σv1D [km/s]
median(σFe/H) = 5.906 [dex]
median(σFe/H) = 5.336 [dex]
median(σFe/H) = 5.483 [dex]
σFe/H [dex]
Nstellar group/Ntotal

Figure C.5

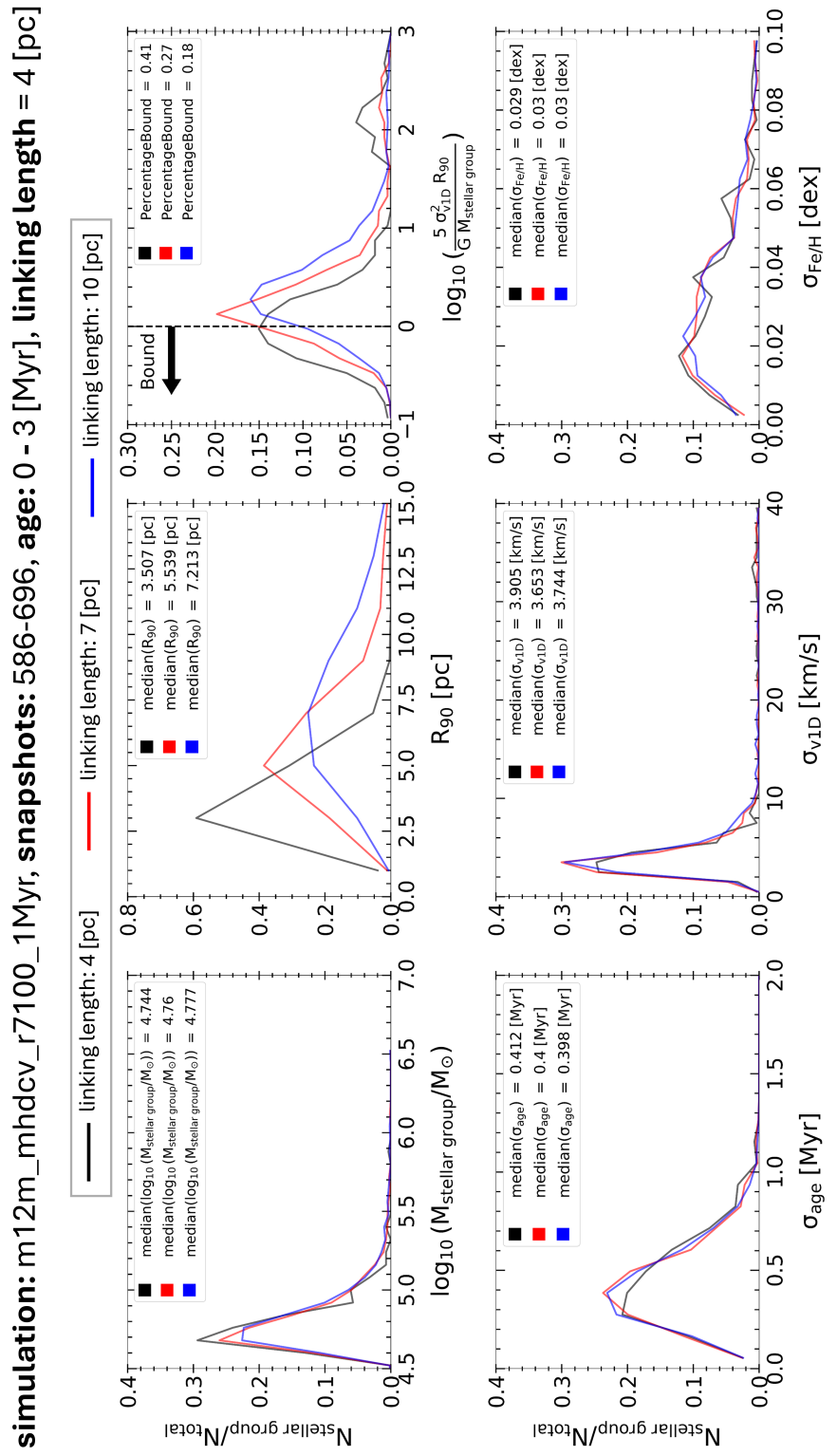
simulation: m12m_mhdcv_r7100_1Myr, snapshots: 586-696, age: 0 - 3 [Myr], linking length = 4 [pc]
linking length: 4 [pc]
linking length: 7 [pc]
linking length: 10 [pc]
median(log10 (Mstellar group/M⊙)) = 4.744
median(log10 (Mstellar group/M⊙)) = 4.76
median(log10 (Mstellar group/M⊙)) = 4.777
Nstellar group/Ntotal
log10 (Mstellar group/M⊙)
median(R90) = 3.507 [pc]
median(R90) = 5.539 [pc]
median(R90) = 7.213 [pc]
R90 [pc]
PercentageBound = 0.41
PercentageBound = 0.27
PercentageBound = 0.18
Bound
log10 (5 σ²v1D R90 / G Mstellar group)
median(σage) = 0.412 [Myr]
median(σage) = 0.4 [Myr]
median(σage) = 0.398 [Myr]
σage [Myr]
median(σv1D) = 3.905 [km/s]
median(σv1D) = 3.653 [km/s]
median(σv1D) = 3.744 [km/s]
σv1D [km/s]
median(σFe/H) = 0.029 [dex]
median(σFe/H) = 0.03 [dex]
median(σFe/H) = 0.03 [dex]
σFe/H [dex]

Figure C.6

Appendix D

one simulation in each plot, age $\leq$ 3 Myrs, linking lengths: 4 pc

This Appendix includes all the plots of Subsection 6.3.5.

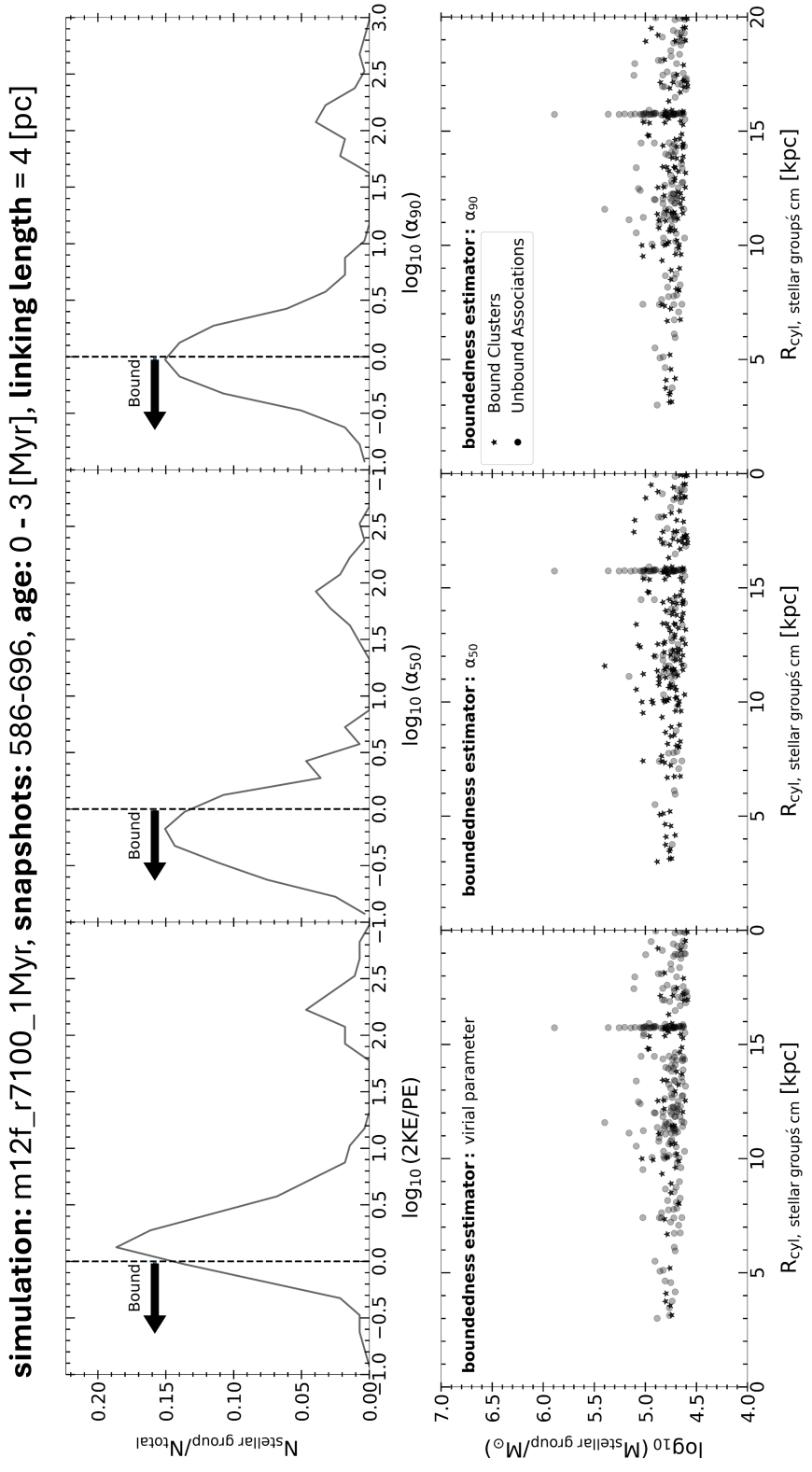
simulation: m12f_r7100_1Myr, snapshots: 586-696, age: 0 - 3 [Myr], linking length = 4 [pc]
N_stellar group/N_total
log10 (2KE/PE)
log10 (α50)
log10 (α90)
Bound
boundedness estimator : virial parameter
boundedness estimator : α50
boundedness estimator : α90
Bound Clusters
Unbound Associations
log10 (M_stellar group/M⊙)
R_cyl, stellar groups cm [kpc]

Figure D.1

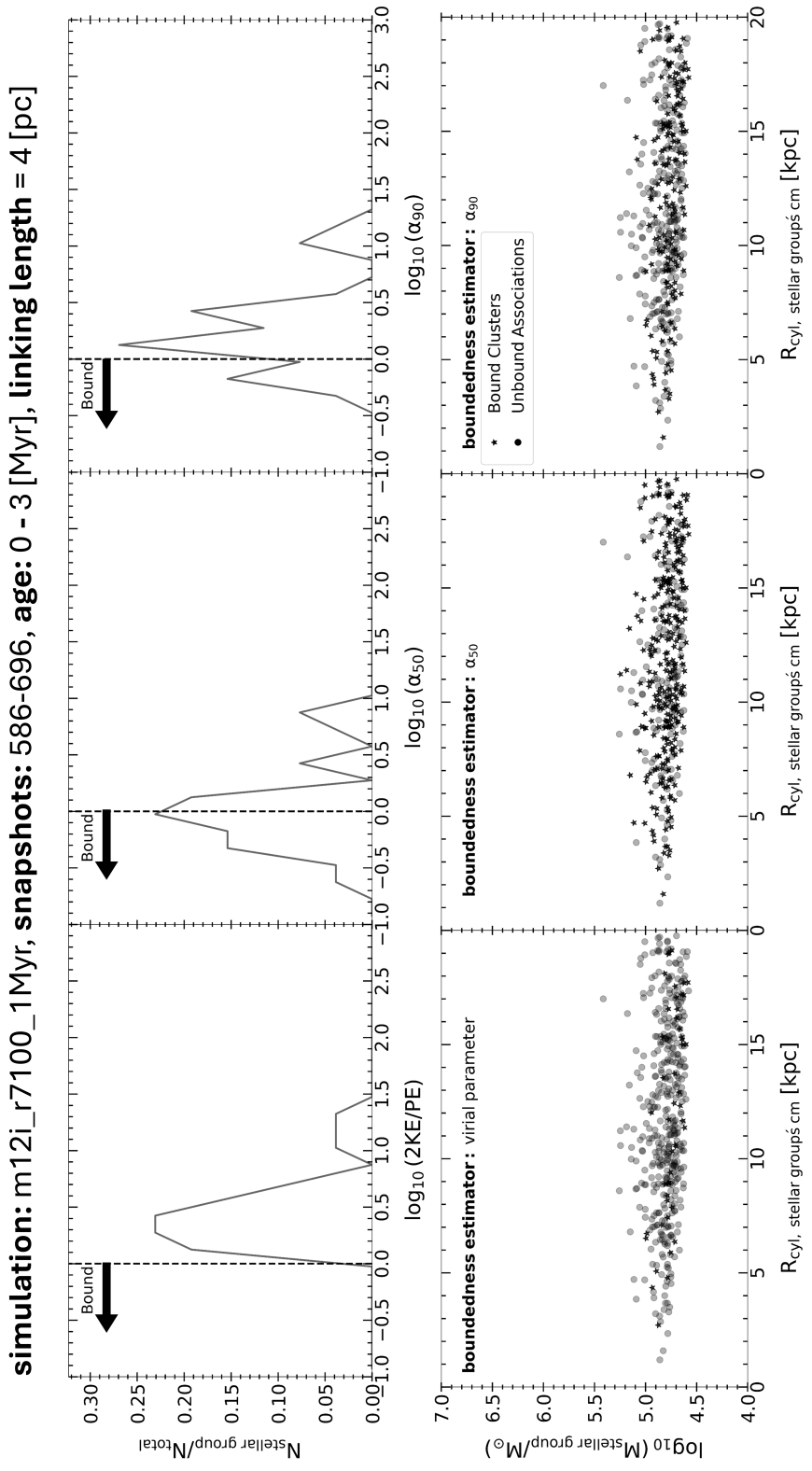
simulation: m12i_r7100_1Myr, snapshots: 586-696, age: 0 - 3 [Myr], linking length = 4 [pc]
Bound
Bound
Bound
N_stellar group/N_total
log10 (2KE/PE)
log10 (α50)
log10 (α90)
boundedness estimator : virial parameter
boundedness estimator : α50
boundedness estimator : α90
Bound Clusters
Unbound Associations
log10 (M_stellar group/M⊙)
R_cyl, stellar groups cm [kpc]
R_cyl, stellar groups cm [kpc]
R_cyl, stellar groups cm [kpc]

Figure D.2

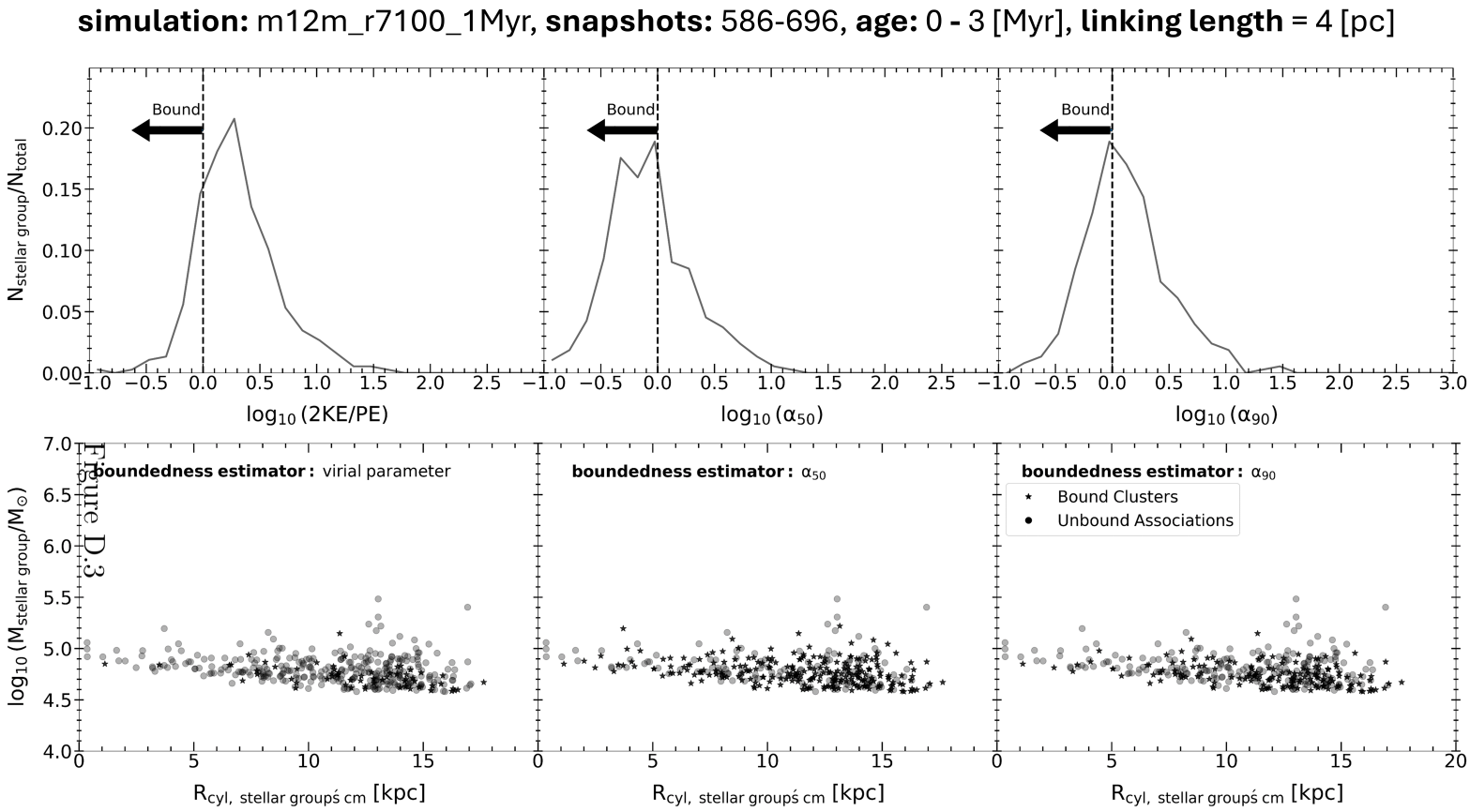
simulation: m12m_r7100_1Myr, snapshots: 586-696, age: 0 - 3 [Myr], linking length = 4 [pc]
Bound
Bound
Bound
N stellar group/N total
log10 (2KE/PE)
log10 (α50)
log10 (α90)
boundedness estimator : virial parameter
boundedness estimator : α50
boundedness estimator : α90
Bound Clusters
Unbound Associations
log10 (M stellar group/M⊙)
R cyl, stellar groups cm [kpc]
R cyl, stellar groups cm [kpc]
R cyl, stellar groups cm [kpc]

Figure D.3

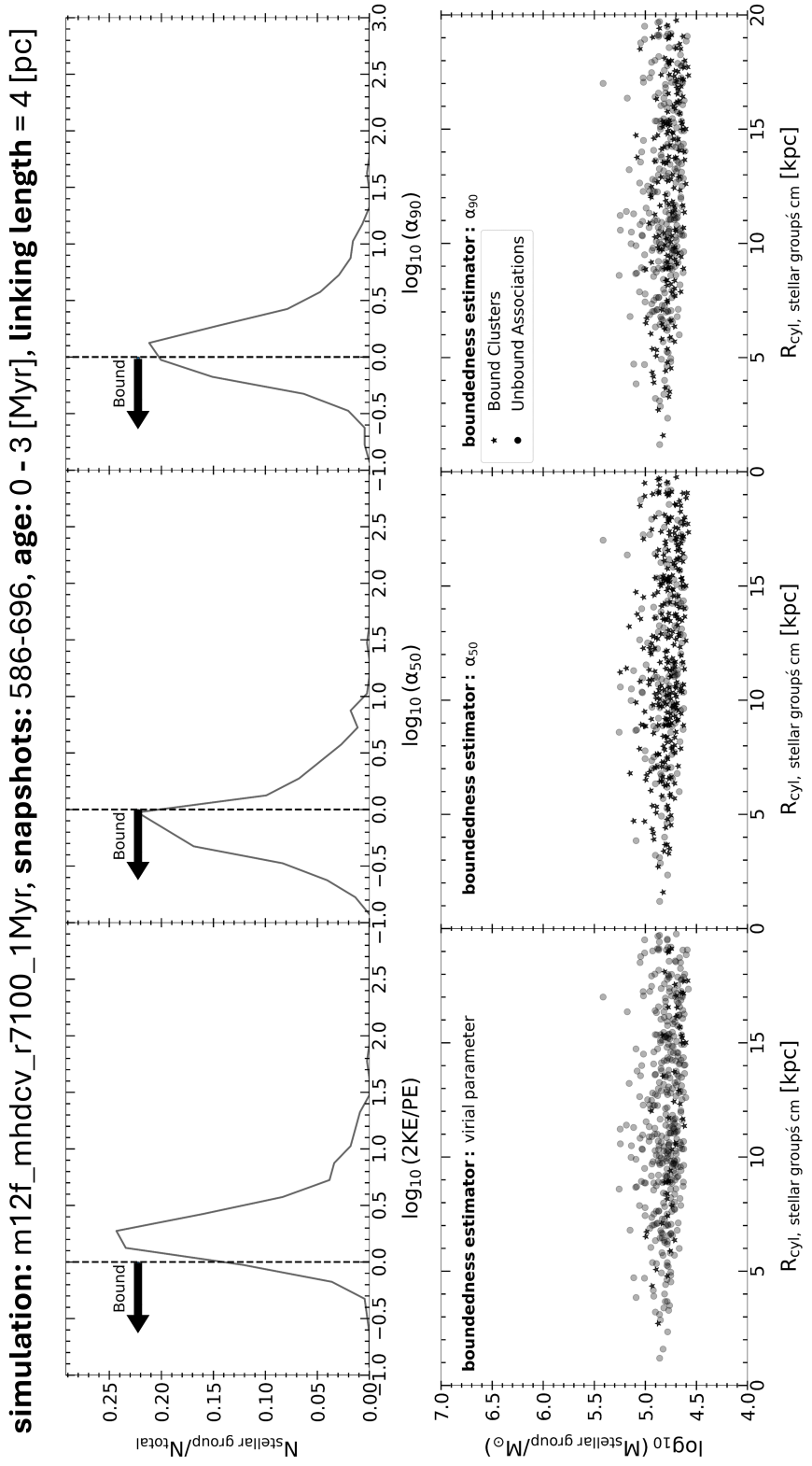
simulation: m12f_mhdcv_r7100_1Myr, snapshots: 586-696, age: 0 - 3 [Myr], linking length = 4 [pc]
N_stellar group/N_total
log10 (2KE/PE)
log10 (α90)
log10 (α50)
Bound
boundedness estimator : virial parameter
boundedness estimator : α50
boundedness estimator : α90
Bound Clusters
Unbound Associations
log10 (M_stellar group/M⊙)
R_cyl, stellar groups cm [kpc]

Figure D.4

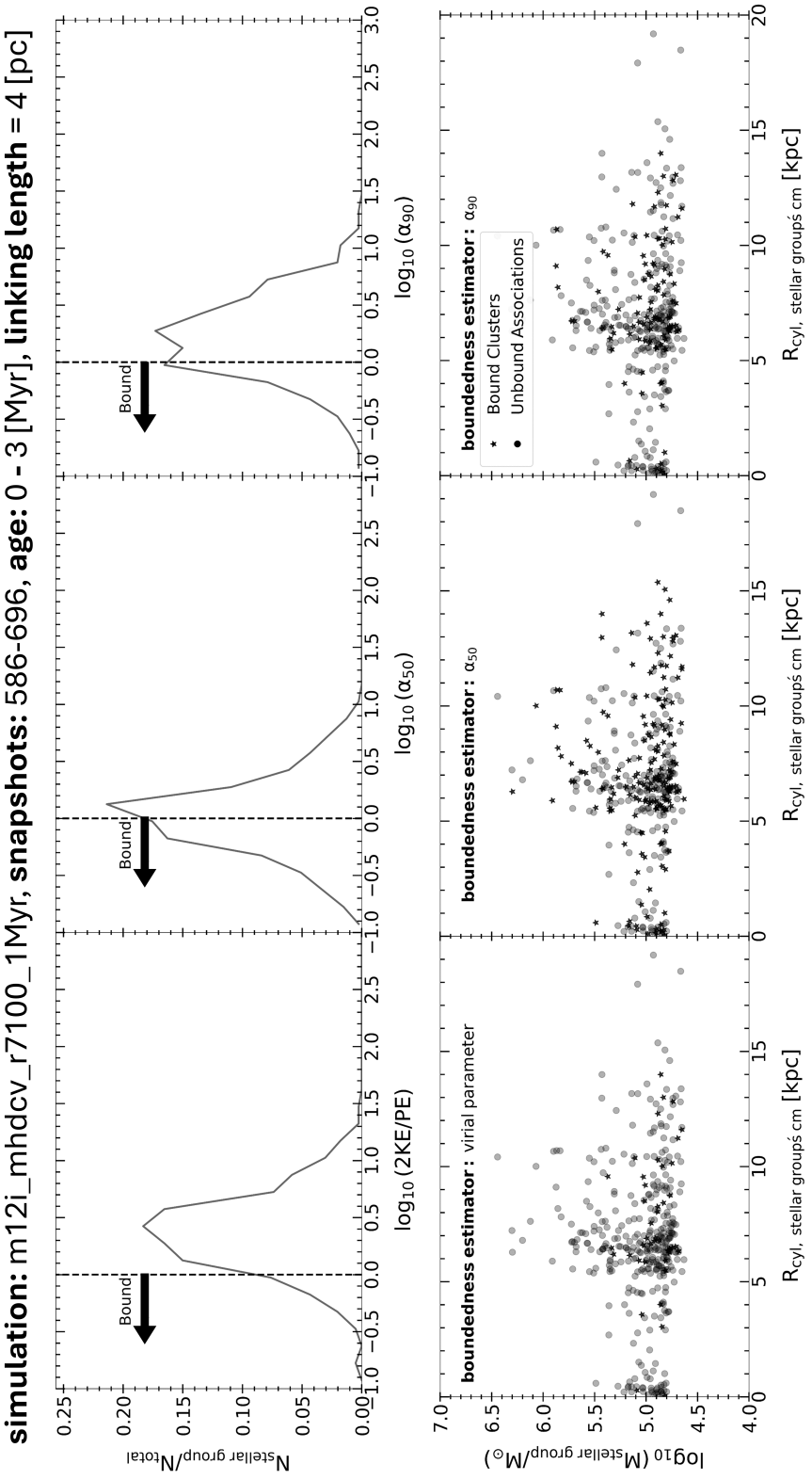
simulation: m12i_mhdcv_r7100_1Myr, snapshots: 586-696, age: 0 - 3 [Myr], linking length = 4 [pc]
N_stellar group/N_total
log10 (2KE/PE)
log10 (α50)
log10 (α90)
Bound
boundedness estimator : virial parameter
boundedness estimator : α50
boundedness estimator : α90
Bound Clusters
Unbound Associations
log10 (M_stellar group/M⊙)
R_cyl, stellar groups cm [kpc]

Figure D.5

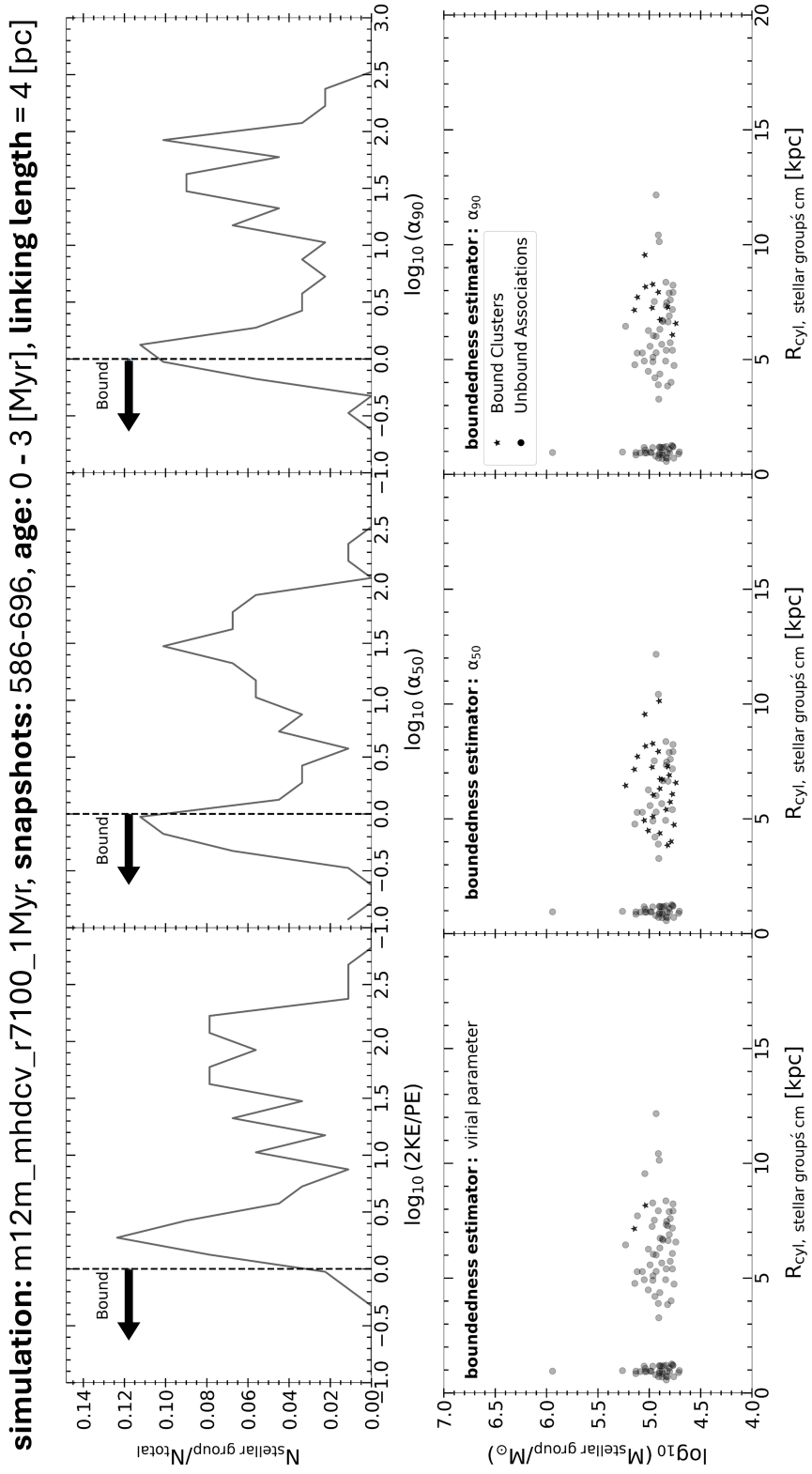
simulation: m12m_mhdcv_r7100_1Myr, snapshots: 586-696, age: 0 - 3 [Myr], linking length = 4 [pc]
N_stellar group/N_total
log10 (2KE/PE)
log10 (α90)
log10 (α50)
Bound
boundedness estimator : virial parameter
boundedness estimator : α50
boundedness estimator : α90
Bound Clusters
Unbound Associations
log10 (M_stellar group/M⊙)
R_cyl, stellar groups cm [kpc]

Figure D.6

Bibliography

[1] TESLA XFEL: First stage of the X-ray laser laboratory. Technical design report, supplement. Technical report, 10 2002.

[2] I. K. Affleck, O. Alvarez, and N. S. Manton. Pair production at strong coupling in weak external fields. *Nuclear Physics B*, 197(3):509–519, 1982.

[3] Y. Aharonov and D. Bohm. Significance of electromagnetic potentials in the quantum theory. *Phys. Rev.*, 115:485–491, Aug 1959.

[4] M. Ali-Akbari and M. Lezgi. Holographic qcd, entanglement entropy, and critical temperature. *Phys. Rev. D*, 96:086014, Oct 2017.

[5] M. Andersen, H. Zinnecker, A. Moneti, M. J. McCaughrean, B. Brandl, W. Brandner, G. Meylan, and D. Hunter. The Low-Mass Initial Mass Function in the 30 Doradus Starburst Cluster. , 707(2):1347–1360, Dec. 2009.

[6] B. Andersson, G. Gustafson, G. Ingelman, and T. Sjöstrand. Parton fragmentation and string dynamics. *Physics Reports*, 97(2):31–145, 1983.

[7] O. Andreev. $1/q^2$ corrections and gauge/string duality. *Phys. Rev. D*, 73:107901, May 2006.

[8] O. Andreev and V. I. Zakharov. Heavy-quark potentials and ads/qcd. *Phys. Rev. D*, 74:025023, Jul 2006.

[9] O. Andreev and V. I. Zakharov. The spatial string tension, thermal phase transition, and ads/qcd. *Physics Letters B*, 645(5):437–441, 2007.

[10] J. Arthur et al. Linac Coherent Light Source (LCLS) Design Study Report. 4 1998.

[11] J. Ascenso, J. Alves, S. Vicente, and M. T. V. T. Lago. NTT and VLT diffraction limited imaging of Trumpler 14: revealing a massive core-halo cluster. , 476(1):199–215, Dec. 2007.

[12] Z. Y. B. and V. S. Popov. Electronic structure of superheavy atoms. *Soviet Physics Uspekhi*, 14(6):673, jun 1972.

[13] C. Bamber, S. J. Boege, T. Koffas, T. Kotseroglou, A. C. Melissinos, D. D. Meyerhofer, D. A. Reis, W. Ragg, C. Bula, K. T. McDonald, E. J. Prebys, D. L. Burke, R. C. Field, G. Horton-Smith, J. E. Spencer, D. Walz, S. C. Berridge, W. M. Bugg, K. Shmakov, and A. W. Weidemann. Studies of nonlinear qed in collisions of 46.6 gev electrons with intense laser pulses. *Phys. Rev. D*, 60:092004, Oct 1999.

[14] P. Barmby, S. Perina, M. Bellazzini, J. G. Cohen, P. W. Hodge, J. P. Huchra, M. Kissler-Patig, T. H. Puzia, and J. Strader. A Hubble Space Telescope/WFPC2 Survey of Bright Young Clusters in M31. III. Structural Parameters. , 138(6):1667–1680, Dec. 2009.

[15] N. Bastian, K. R. Covey, and M. R. Meyer. A Universal Stellar Initial Mass Function? A Critical Look at Variations. , 48:339–389, Sept. 2010.

[16] M. A. Bég and A. Sirlin. Gauge theories of weak interactions (circa 1973-74 ce). *Annual review of nuclear science*, 24(1):379–450, 1974.

[17] M. A. B. Bég and A. Sirlin. Gauge theories of weak interactions ii (circa 1981–1982 ce). *Physics Reports*, 88(1):1–90, 1982.

[18] M. A. Bellardini, A. Wetzel, S. R. Loebman, and J. Bailin. 3D elemental abundances of stars at formation across the histories of Milky Way-mass galaxies in the FIRE simulations. , 514(3):4270–4289, Aug. 2022.

[19] S. M. Benincasa, S. R. Loebman, A. Wetzel, P. F. Hopkins, N. Murray, M. A. Bellardini, C.-A. Faucher-Giguère, D. Guszejnov, and M. Orr. Live fast, die young: GMC lifetimes in the FIRE cosmological simulations of Milky Way mass galaxies. , 497(3):3993–3999, Sept. 2020.

[20] F. Bertoldi and C. F. McKee. Pressure-confined Clumps in Magnetized Molecular Clouds. , 395:140, Aug. 1992.

[21] S. Bethke. s 2002. *Nuclear Physics B - Proceedings Supplements*, 121:74–81, 2003. Proceedings of the QCD 02 9th High-Energy Physics International Conference on Quantum ChromoDynamics.

[22] A. Bik, H. J. G. L. M. Lamers, N. Bastian, N. Panagia, and M. Romaniello. Clusters in the inner spiral arms of M 51: The cluster IMF and the formation history. , 397:473–486, Jan. 2003.

[23] T. Biro, H. Nielsen, and J. Knoll. Colour rope model for extreme relativistic heavy ion collisions. *Nuclear Physics B*, 245:449–468, 1984.

[24] N. D. Birrell and P. C. W. Davies. *Quantum Fields in Curved Space*. Cambridge Monographs on Mathematical Physics. Cambridge Univ. Press, Cambridge, UK, 2 1984.

[25] J. Bland-Hawthorn and O. Gerhard. The Galaxy in Context: Structural, Kinematic, and Integrated Properties. , 54:529–596, Sept. 2016.

[26] S. Bolognesi, F. Kiefer, and E. Rabinovici. Comments on Critical Electric and Magnetic Fields from Holography. *JHEP*, 01:174, 2013.

[27] R. Bonifacio, C. Pellegrini, and L. Narducci. Collective instabilities and high-gain regime in a free electron laser. *Optics Communications*, 50(6):373–378, 1984.

[28] E. Brezin and C. Itzykson. Pair production in vacuum by an alternating field. *Phys. Rev. D*, 2:1191–1199, Oct 1970.

[29] R. Brinkmann, G. Materlik, J. Rossbach, and A. Wagner. Hamburg, DESY, 1997, 1183 p; Hamburg DESY, DESY-97-048 (97/05. rec. Sep.) 1183 p. (ECFA 97-182). Technical report, DESY, 1997.

[30] A. G. A. Brown. Microarcsecond Astrometry: Science Highlights from Gaia. , 59:59–115, Sept. 2021.

[31] F. V. Bunkin and I. I. Tugov. The possibility of electron-positron pair production in vacuum when laser radiation is focussed. In *Doklady Akademii Nauk*, volume 187, pages 541–544. Russian Academy of Sciences, 1969.

[32] D. L. Burke, R. C. Field, G. Horton-Smith, J. E. Spencer, D. Walz, S. C. Berridge, W. M. Bugg, K. Shmakov, A. W. Weidemann, C. Bula, K. T. McDonald, E. J. Prebys, C. Bamber, S. J. Boege, T. Koffas, T. Kotseroglou, A. C. Melissinos, D. D. Meyerhofer, D. A. Reis, and W. Ragg. Positron production in multiphoton light-by-light scattering. *Phys. Rev. Lett.*, 79:1626–1629, Sep 1997.

[33] D. Calzetti. LEGUS: Legacy ExtraGalactic UV Survey. HST Proposal, Oct. 2013.

[34] D. Calzetti, J. C. Lee, E. Sabbi, A. Adamo, L. J. Smith, J. E. Andrews, L. Ubeda, S. N. Bright, D. Thilker, A. Aloisi, T. M. Brown, R. Chandar, C. Christian, M. Cignoni, G. C. Clayton, R. da Silva, S. E. de Mink, C. Dobbs, B. G. Elmegreen, D. M. Elmegreen, A. S. Evans, M. Fumagalli, I. Gallagher,

J. S., D. A. Gouliermis, E. K. Grebel, A. Herrero, D. A. Hunter, K. E. Johnson, R. C. Kennicutt, H. Kim, M. R. Krumholz, D. Lennon, K. Levay, C. Martin, P. Nair, A. Nota, G. Östlin, A. Pellerin, J. Prieto, M. W. Regan, J. E. Ryon, D. Schaerer, D. Schiminovich, M. Tosi, S. D. Van Dyk, R. Walterbos, B. C. Whitmore, and A. Wofford. Legacy Extragalactic UV Survey (LEGUS) With the Hubble Space Telescope. I. Survey Description. , 149(2):51, Feb. 2015.

[35] R. J. G. B. Campello, D. Moulavi, and J. Sander. Density-based clustering based on hierarchical density estimates. In J. Pei, V. S. Tseng, L. Cao, H. Motoda, and G. Xu, editors, *Advances in Knowledge Discovery and Data Mining*, pages 160–172, Berlin, Heidelberg, 2013. Springer Berlin Heidelberg.

[36] T. Cantat-Gaudin, C. Jordi, A. Vallenari, A. Bragaglia, L. Balaguer-Núñez, C. Soubiran, D. Bossini, A. Moitinho, A. Castro-Ginard, A. Krone-Martins, L. Casamiquela, R. Sordo, and R. Carrera. A Gaia DR2 view of the open cluster population in the Milky Way. , 618:A93, Oct. 2018.

[37] B. W. Carroll and D. A. Ostlie. *An introduction to modern astrophysics*. Cambridge University Press, 2017.

[38] J. Casalderrey-Solana, H. Liu, D. Mateos, K. Rajagopal, and U. A. Wiedemann. *Gauge/String Duality, Hot QCD and Heavy Ion Collisions*. Cambridge University Press, 2014.

[39] A. Casher, H. Neuberger, and S. Nussinov. Chromoelectric-flux-tube model of particle production. *Phys. Rev. D*, 20:179–188, Jul 1979.

[40] R. Chandar, L. Bianchi, and H. C. Ford. Spectroscopy of Star Cluster Candidates and H II Regions in NGC 6822. , 120(6):3088–3097, Dec. 2000.

[41] P. Chen and C. Pellegrini. Boiling the vacuum with intense electromagnetic

fields. In *15th Advanced ICFA Beam Dynamics Workshop on Quantum Aspects of Beam Physics*, pages 571–576, 1 1998.

[42] J. S. Clark, I. Negueruela, B. Davies, V. M. Larionov, B. W. Ritchie, D. F. Figer, M. Messineo, P. A. Crowther, and A. A. Arkharov. A third red supergiant rich cluster in the Scutum-Crux arm. , 498(1):109–114, Apr. 2009.

[43] C. J. Clarke, I. A. Bonnell, and L. A. Hillenbrand. The Formation of Stellar Clusters. In V. Mannings, A. P. Boss, and S. S. Russell, editors, *Protostars and Planets IV*, page 151, May 2000.

[44] T. Damour and R. Ruffini. Black-hole evaporation in the klein-sauter-heisenberg-euler formalism. *Phys. Rev. D*, 14:332–334, Jul 1976.

[45] H. David Politzer. Asymptotic freedom: An approach to strong interactions. *Physics Reports*, 14(4):129–180, 1974.

[46] B. Davies, D. F. Figer, R.-P. Kudritzki, J. MacKenty, F. Najarro, and A. Herrero. A Massive Cluster of Red Supergiants at the Base of the Scutum-Crux Arm. , 671(1):781–801, Dec. 2007.

[47] M. Davis, G. Efstathiou, C. S. Frenk, and S. D. M. White. The evolution of large-scale structure in a universe dominated by cold dark matter. , 292:371–394, May 1985.

[48] R. de Grijs. A revolution in star cluster research: setting the scene. *Philosophical Transactions of the Royal Society of London Series A*, 368(1913):693–711, Jan. 2010.

[49] G. F. de Téramond and S. J. Brodsky. Light-front holography and gauge/gravity duality: The light meson and baryon spectra. *Nuclear Physics*

B - Proceedings Supplements, 199(1):89–96, 2010. Proceedings of the International Workshop Light Cone 2009 (LC2009): Relativistic Hadronic and Particle Physics.

[50] W.-T. Deng and X.-G. Huang. Event-by-event generation of electromagnetic fields in heavy-ion collisions. *Phys. Rev. C*, 85:044907, Apr 2012.

[51] C. Dobbs. 2a Results: galaxy to cloud scales. *Frontiers in Astronomy and Space Sciences*, 10:1272771, Nov. 2023.

[52] C. L. Dobbs, A. Adamo, C. G. Few, D. Calzetti, D. A. Dale, B. G. Elmegreen, A. S. Evans, D. A. Gouliermis, K. Grasha, E. K. Grebel, K. E. Johnson, H. Kim, J. C. Lee, M. Messa, J. E. Ryon, L. J. Smith, D. Thilker, L. Ubeda, and B. Whitmore. The properties, origin and evolution of stellar clusters in galaxy simulations and observations. , 464(3):3580–3596, Jan. 2017.

[53] C. L. Dobbs, M. R. Krumholz, J. Ballesteros-Paredes, A. D. Bolatto, Y. Fukui, M. Heyer, M. M. M. Low, E. C. Ostriker, and E. Vázquez-Semadeni. Formation of Molecular Clouds and Global Conditions for Star Formation. In H. Beuther, R. S. Klessen, C. P. Dullemond, and T. Henning, editors, *Protostars and Planets VI*, pages 3–26, Jan. 2014.

[54] G. Dunne and T. Hall. Qed effective action in time dependent electric backgrounds. *Phys. Rev. D*, 58:105022, Oct 1998.

[55] F. J. Dyson. The radiation theories of tomonaga, schwinger, and feynman. *Phys. Rev.*, 75:486–502, Feb 1949.

[56] F. J. Dyson. The s matrix in quantum electrodynamics. *Phys. Rev.*, 75:1736–1755, Jun 1949.

[57] J. Einasto, A. A. Klypin, E. Saar, and S. F. Shandarin. Structure of superclusters and supercluster formation - III. Quantitative study of the Local Supercluster. , 206:529–558, Feb. 1984.

[58] E. Emsellem, E. Schinnerer, F. Santoro, F. Belfiore, I. Pessa, R. McElroy, G. A. Blanc, E. Congiu, B. Groves, I. T. Ho, K. Kreckel, A. Razza, P. Sanchez-Blazquez, O. Egorov, C. Faesi, R. S. Klessen, A. K. Leroy, S. Meidt, M. Querejeta, E. Rosolowsky, F. Scheuermann, G. S. Anand, A. T. Barnes, I. Bešlić, F. Bigiel, M. Boquien, Y. Cao, M. Chevance, D. A. Dale, C. Eibensteiner, S. C. O. Glover, K. Grasha, J. D. Henshaw, A. Hughes, E. W. Koch, J. M. D. Kruijssen, J. Lee, D. Liu, H.-A. Pan, J. Pety, T. Saito, K. M. Sandstrom, A. Schruba, J. Sun, D. A. Thilker, A. Usero, E. J. Watkins, and T. G. Williams. The PHANGS-MUSE survey. Probing the chemo-dynamical evolution of disc galaxies. , 659:A191, Mar. 2022.

[59] E. Fermi. Versuch einer theorie der β-strahlen. i. *Zeitschrift für Physik*, 88(3):161–177, 1934.

[60] R. P. Feynman. Space-time approach to quantum electrodynamics. *Phys. Rev.*, 76:769–789, Sep 1949.

[61] R. P. Feynman. Mathematical formulation of the quantum theory of electromagnetic interaction. *Phys. Rev.*, 80:440–457, Nov 1950.

[62] D. F. Figer, J. W. MacKenty, M. Robberto, K. Smith, F. Najarro, R. P. Kudritzki, and A. Herrero. Discovery of an Extraordinarily Massive Cluster of Red Supergiants. , 643(2):1166–1179, June 2006.

[63] D. F. Figer, I. S. McLean, and M. Morris. Massive Stars in the Quintuplet Cluster. , 514(1):202–220, Mar. 1999.

[64] W. Fischler, P. H. Nguyen, J. F. Pedraza, and W. Tangarife. Holographic schwinger effect in de sitter space. *Phys. Rev. D*, 91:086015, Apr 2015.

[65] H. M. Fried, Y. Gabellini, B. H. J. McKellar, and J. Avan. Pair production via crossed lasers. *Phys. Rev. D*, 63:125001, Apr 2001.

[66] Gaia Collaboration, A. Vallenari, A. G. A. Brown, T. Prusti, J. H. J. de Bruijne, F. Arenou, C. Babusiaux, M. Biermann, O. L. Creevey, C. Ducourant, D. W. Evans, L. Eyer, R. Guerra, A. Hutton, C. Jordi, S. A. Klioner, U. L. Lammers, L. Lindegren, X. Luri, F. Mignard, C. Panem, D. Pourbaix, S. Randich, P. Sartoretti, C. Soubiran, P. Tanga, N. A. Walton, C. A. L. Bailer-Jones, U. Bastian, R. Drimmel, F. Jansen, D. Katz, M. G. Lattanzi, F. van Leeuwen, J. Bakker, C. Cacciari, J. Castañeda, F. De Angeli, C. Fabricius, M. Fouesneau, Y. Frémat, L. Galluccio, A. Guerrier, U. Heiter, E. Masana, R. Messineo, N. Mowlavi, C. Nicolas, K. Nienartowicz, F. Pailler, P. Panuzzo, F. Riclet, W. Roux, G. M. Seabroke, R. Sordo, F. Thévenin, G. Gracia-Abril, J. Portell, D. Teyssier, M. Altmann, R. Andrae, M. Audard, I. Bellas-Velidis, K. Benson, J. Berthier, R. Blomme, P. W. Burgess, D. Busonero, G. Busso, H. Cánovas, B. Carry, A. Cellino, N. Cheek, G. Clementini, Y. Damerdji, M. Davidson, P. de Teodoro, M. Nuñez Campos, L. Delchambre, A. Dell'Oro, P. Esquej, J. Fernández-Hernández, E. Fraile, D. Garabato, P. García-Lario, E. Gosset, R. Haigron, J. L. Halbwachs, N. C. Hambly, D. L. Harrison, J. Hernández, D. Hestroffer, S. T. Hodgkin, B. Holl, K. Janßen, G. Jevardat de Fombelle, S. Jordan, A. Krone-Martins, A. C. Lanzafame, W. Löffler, O. Marchal, P. M. Marrese, A. Moitinho, K. Muinonen, P. Osborne, E. Pancino, T. Pauwels, A. Recio-Blanco, C. Reylé, M. Riello, L. Rimoldini, T. Roegiers, J. Rybizki, L. M. Sarro, C. Siopis, M. Smith, A. Sozzetti, E. Utrilla, M. van Leeuwen, U. Abbas, P. Ábrahám, A. Abreu Aramburu, C. Aerts, J. J. Aguado, M. Ajaj, F. Aldea-Montero, G. Altavilla, M. A. Álvarez, J. Alves, F. Anders, R. I. Ander-

son, E. Anglada Varela, T. Antoja, D. Baines, S. G. Baker, L. Balaguer-Núñez, E. Balbinot, Z. Balog, C. Barache, D. Barbato, M. Barros, M. A. Barstow, S. Bartolomé, J. L. Bassilana, N. Bauchet, U. Becciani, M. Bellazzini, A. Berihuete, M. Bernet, S. Bertone, L. Bianchi, A. Binnenfeld, S. Blanco-Cuaresma, A. Blazere, T. Boch, A. Bombrun, D. Bossini, S. Bouquillon, A. Bragaglia, L. Bramante, E. Breedt, A. Bressan, N. Brouillet, E. Brugaletta, B. Bucciarelli, A. Burlacu, A. G. Butkevich, R. Buzzi, E. Caffau, R. Cancelliere, T. Cantat-Gaudin, R. Carballo, T. Carlucci, M. I. Carnerero, J. M. Carrasco, L. Casamiquela, M. Castellani, A. Castro-Ginard, L. Chaoul, P. Charlot, L. Chemin, V. Chiaramida, A. Chiavassa, N. Chornay, G. Comoretto, G. Contursi, W. J. Cooper, T. Cornez, S. Cowell, F. Crifo, M. Cropper, M. Crosta, C. Crowley, C. Dafonte, A. Dapergolas, M. David, P. David, P. de Laverny, F. De Luise, R. De March, J. De Ridder, R. de Souza, A. de Torres, E. F. del Peloso, E. del Pozo, M. Delbo, A. Delgado, J. B. Delisle, C. Demouchy, T. E. Dharmawardena, P. Di Matteo, S. Diakite, C. Diener, E. Distefano, C. Dolding, B. Edvardsson, H. Enke, C. Fabre, M. Fabrizio, S. Faigler, G. Fedorets, P. Fernique, A. Fienga, F. Figueras, Y. Fournier, C. Fouron, F. Fragkoudi, M. Gai, A. Garcia-Gutierrez, M. Garcia-Reinaldos, M. García-Torres, A. Garofalo, A. Gavel, P. Gavras, E. Gerlach, R. Geyer, P. Giacobbe, G. Gilmore, S. Girona, G. Giuffrida, R. Gomel, A. Gomez, J. González-Núñez, I. González-Santamaría, J. J. González-Vidal, M. Granvik, P. Guillout, J. Guiraud, R. Gutiérrez-Sánchez, L. P. Guy, D. Hatzidimitriou, M. Hauser, M. Haywood, A. Helmer, A. Helmi, M. H. Sarmiento, S. L. Hidalgo, T. Hilger, N. Hładczuk, D. Hobbs, G. Holland, H. E. Huckle, K. Jardine, G. Jasniewicz, A. Jean-Antoine Piccolo, Ó. Jiménez-Arranz, A. Jorissen, J. Juaristi Campillo, F. Julbe, L. Karbevska, P. Kervella, S. Khanna, M. Kontizas, G. Kordopatis, A. J. Korn, Á. Kóspál, Z. Kostrzewa-Rutkowska, K. Kruszyńska, M. Kun, P. Laizeau, S. Lambert, A. F. Lanza, Y. Lasne, J. F. Le Campion, Y. Le-

breton, T. Lebzelter, S. Leccia, N. Leclerc, I. Lecoeur-Taibi, S. Liao, E. L. Licata, H. E. P. Lindstrøm, T. A. Lister, E. Livanou, A. Lobel, A. Lorca, C. Loup, P. Madrero Pardo, A. Magdaleno Romeo, S. Managau, R. G. Mann, M. Manteiga, J. M. Marchant, M. Marconi, J. Marcos, M. M. S. Marcos Santos, D. Marín Pina, S. Marinoni, F. Marocco, D. J. Marshall, L. Martin Polo, J. M. Martín-Fleitas, G. Marton, N. Mary, A. Masip, D. Massari, A. Mastrobuono-Battisti, T. Mazeh, P. J. McMillan, S. Messina, D. Michalik, N. R. Millar, A. Mints, D. Molina, R. Molinaro, L. Molnár, G. Monari, M. Monguió, P. Montegriffo, A. Montero, R. Mor, A. Mora, R. Morbidelli, T. Morel, D. Morris, T. Muraveva, C. P. Murphy, I. Musella, Z. Nagy, L. Noval, F. Ocaña, A. Ogden, C. Ordenovic, J. O. Osinde, C. Pagani, I. Pagano, L. Palaversa, P. A. Palicio, L. Pallas-Quintela, A. Panahi, S. Payne-Wardenaar, X. Peñalosa Esteller, A. Penttilä, B. Pichon, A. M. Piersimoni, F. X. Pineau, E. Plachy, G. Plum, E. Poggio, A. Prša, L. Pulone, E. Racero, S. Ragaini, M. Rainer, C. M. Raiteri, N. Rambaux, P. Ramos, M. Ramos-Lerate, P. Re Fiorentin, S. Regibo, P. J. Richards, C. Rios Diaz, V. Ripepi, A. Riva, H. W. Rix, G. Rixon, N. Robichon, A. C. Robin, C. Robin, M. Roelens, H. R. O. Rogues, L. Rohrbasser, M. Romero-Gómez, N. Rowell, F. Royer, D. Ruz Mieres, K. A. Rybicki, G. Sadowski, A. Sáez Núñez, A. Sagristà Sellés, J. Sahlmann, E. Salguero, N. Samaras, V. Sanchez Gimenez, N. Sanna, R. Santoveña, M. Sarasso, M. Schultheis, E. Sciacca, M. Segol, J. C. Segovia, D. Ségransan, D. Semeux, S. Shahaf, H. I. Siddiqui, A. Siebert, L. Siltala, A. Silvelo, E. Slezak, I. Slezak, R. L. Smart, O. N. Snaith, E. Solano, F. Solitro, D. Souami, J. Souchay, A. Spagna, L. Spina, F. Spoto, I. A. Steele, H. Steidelmüller, C. A. Stephenson, M. Süveges, J. Surdej, L. Szabados, E. Szegedi-Elek, F. Taris, M. B. Taylor, R. Teixeira, L. Tolomei, N. Tonello, F. Torra, J. Torra, G. Torralba Elipe, M. Trabucchi, A. T. Tsounis, C. Turon, A. Ulla, N. Unger, M. V. Vaillant, E. van Dillen, W. van Reeven, O. Vanel, A. Vecchiato, Y. Viala, D. Vicente, S. Voutsinas,

M. Weiler, T. Wevers, Ł. Wyrzykowski, A. Yoldas, P. Yvard, H. Zhao, J. Zorec, S. Zucker, and T. Zwitter. Gaia Data Release 3. Summary of the content and survey properties. , 674:A1, June 2023.

[67] S. Garrison-Kimmel, P. F. Hopkins, A. Wetzel, J. S. Bullock, M. Boylan-Kolchin, D. Kereš, C.-A. Faucher-Giguère, K. El-Badry, A. Lamberts, E. Quataert, and R. Sanderson. The Local Group on FIRE: dwarf galaxy populations across a suite of hydrodynamic simulations. , 487(1):1380–1399, July 2019.

[68] S. P. Gavrilov and D. M. Gitman. Vacuum instability in external fields. *Phys. Rev. D*, 53:7162–7175, Jun 1996.

[69] M. Ghodrati. Schwinger effect and entanglement entropy in confining geometries. *Phys. Rev. D*, 92:065015, Sep 2015.

[70] G. W. Gibbons and M. J. Perry. Black Holes and Thermal Green's Functions. *Proc. Roy. Soc. Lond. A*, 358(3):467–494, 1978.

[71] H. Goldstein. *Classical Mechanics*. Addison Wesley, 3rd edition, 2001.

[72] R. J. J. Grand, F. Fragkoudi, F. A. Gómez, A. Jenkins, F. Marinacci, R. Pakmor, and V. Springel. Overview and public data release of the Auriga Project: cosmological simulations of dwarf and Milky Way-mass galaxies. *arXiv e-prints*, page arXiv:2401.08750, Jan. 2024.

[73] K. Grasha, D. Calzetti, A. Adamo, R. C. Kennicutt, B. G. Elmegreen, M. Messa, D. A. Dale, K. Fedorenko, S. Mahadevan, E. K. Grebel, M. Fumagalli, H. Kim, C. L. Dobbs, D. A. Gouliermis, G. Ashworth, J. S. Gallagher, L. J. Smith, M. Tosi, B. C. Whitmore, E. Schinnerer, D. Colombo, A. Hughes, A. K. Leroy, and S. E. Meidt. The spatial relation between young star clusters and molecular clouds in M51 with LEGUS. , 483(4):4707–4723, Mar. 2019.

[74] W. Greiner, B. Müller, et al. *Gauge theory of weak interactions*, volume 5. Springer, 1996.

[75] W. Greiner and J. Reinhardt. Supercritical fields in heavy ion physics - A status report. In *15th Advanced ICFA Beam Dynamics Workshop on Quantum Aspects of Beam Physics*, pages 438–463, 1 1998.

[76] W. Greiner, S. Schramm, and E. Stein. *Quantum chromodynamics*. Springer Science & Business Media, 2013.

[77] D. Griffiths. *Introduction to elementary particles*. John Wiley & Sons, 2008.

[78] D. J. Gross and F. Wilczek. Asymptotically free gauge theories. i. *Phys. Rev. D*, 8:3633–3652, Nov 1973.

[79] D. J. Gross and F. Wilczek. Ultraviolet behavior of non-abelian gauge theories. *Phys. Rev. Lett.*, 30:1343–1346, Jun 1973.

[80] D. J. Gross and F. Wilczek. Asymptotically free gauge theories. ii. *Phys. Rev. D*, 9:980–993, Feb 1974.

[81] F. Gross, E. Klempt, S. J. Brodsky, A. J. Buras, V. D. Burkert, G. Heinrich, K. Jakobs, C. A. Meyer, K. Orginos, M. Strickland, et al. 50 years of quantum chromodynamics: Introduction and review. *The European Physical Journal C*, 83(12):1125, 2023.

[82] P. D. Group, R. L. Workman, V. D. Burkert, V. Crede, E. Klempt, U. Thoma, L. Tiator, K. Agashe, G. Aielli, B. C. Allanach, C. Amsler, M. Antonelli, E. C. Aschenauer, D. M. Asner, H. Baer, S. Banerjee, R. M. Barnett, L. Baudis, C. W. Bauer, J. J. Beatty, V. I. Belousov, J. Beringer, A. Bettini, O. Biebel, K. M. Black, E. Blucher, R. Bonventre, V. V. Bryzgalov, O. Buchmuller, M. A. Bychkov, R. N. Cahn, M. Carena, A. Ceccucci, A. Cerri, R. S. Chivukula,

G. Cowan, K. Cranmer, O. Cremonesi, G. D'Ambrosio, T. Damour, D. de Florian, A. de Gouvêa, T. DeGrand, P. de Jong, S. Demers, B. A. Dobrescu, M. D'Onofrio, M. Doser, H. K. Dreiner, P. Eerola, U. Egede, S. Eidelman, A. X. El-Khadra, J. Ellis, S. C. Eno, J. Erler, V. V. Ezhela, W. Fetscher, B. D. Fields, A. Freitas, H. Gallagher, Y. Gershtein, T. Gherghetta, M. C. Gonzalez-Garcia, M. Goodman, C. Grab, A. V. Gritsan, C. Grojean, D. E. Groom, M. Grünewald, A. Gurtu, T. Gutsche, H. E. Haber, M. Hamel, C. Hanhart, S. Hashimoto, Y. Hayato, A. Hebecker, S. Heinemeyer, J. J. Hernández-Rey, K. Hikasa, J. Hisano, A. Höcker, J. Holder, L. Hsu, J. Huston, T. Hyodo, A. Ianni, M. Kado, M. Karliner, U. F. Katz, M. Kenzie, V. A. Khoze, S. R. Klein, F. Krauss, M. Kreps, P. Križan, B. Krusche, Y. Kwon, O. Lahav, J. Laiho, L. P. Lellouch, J. Lesgourgues, A. R. Liddle, Z. Ligeti, C.-J. Lin, C. Lippmann, T. M. Liss, L. Littenberg, C. Lourenço, K. S. Lugovsky, S. B. Lugovsky, A. Lusiani, Y. Makida, F. Maltoni, T. Mannel, A. V. Manohar, W. J. Marciano, A. Masoni, J. Matthews, U.-G. Meißner, I.-A. Melzer-Pellmann, M. Mikhasenko, D. J. Miller, D. Milstead, R. E. Mitchell, K. Mönig, P. Molaro, F. Moortgat, M. Moskovic, K. Nakamura, M. Narain, P. Nason, S. Navas, A. Nelles, M. Neubert, P. Nevski, Y. Nir, K. A. Olive, C. Patrignani, J. A. Peacock, V. A. Petrov, E. Pianori, A. Pich, A. Piepke, F. Pietropaolo, A. Pomarol, S. Pordes, S. Profumo, A. Quadt, K. Rabbertz, J. Rademacker, G. Raffelt, M. Ramsey-Musolf, B. N. Ratcliff, P. Richardson, A. Ringwald, D. J. Robinson, S. Roesler, S. Rolli, A. Romaniouk, L. J. Rosenberg, J. L. Rosner, G. Rybka, M. G. Ryskin, R. A. Ryutin, Y. Sakai, S. Sarkar, F. Sauli, O. Schneider, S. Schönert, K. Scholberg, A. J. Schwartz, J. Schwiening, D. Scott, F. Sefkow, U. Seljak, V. Sharma, S. R. Sharpe, V. Shiltsev, G. Signorelli, M. Silari, F. Simon, T. Sjöstrand, P. Skands, T. Skwarnicki, G. F. Smoot, A. Soffer, M. S. Sozzi, S. Spanier, C. Spiering, A. Stahl, S. L. Stone, Y. Sumino, M. J. Syphers, F. Takahashi, M. Tanabashi, J. Tanaka, M. Taševský, K. Terao, K. Terashi,

J. Terning, R. S. Thorne, M. Titov, N. P. Tkachenko, D. R. Tovey, K. Trabelsi, P. Urquijo, G. Valencia, R. Van de Water, N. Varelas, G. Venanzoni, L. Verde, I. Vivarelli, P. Vogel, W. Vogelsang, V. Vorobyev, S. P. Wakely, W. Walkowiak, C. W. Walter, D. Wands, D. H. Weinberg, E. J. Weinberg, N. Wermes, M. White, L. R. Wiencke, S. Willocq, C. G. Wohl, C. L. Woody, W.-M. Yao, M. Yokoyama, R. Yoshida, G. Zanderighi, G. P. Zeller, O. V. Zenin, R.-Y. Zhu, S.-L. Zhu, F. Zimmermann, and P. A. Zyla. Review of Particle Physics. *Progress of Theoretical and Experimental Physics*, 2022(8):083C01, 08 2022.

[83] M. Y. Grudić, J. M. D. Kruijssen, C.-A. Faucher-Giguère, P. F. Hopkins, X. Ma, E. Quataert, and M. Boylan-Kolchin. A model for the formation of stellar associations and clusters from giant molecular clouds. , 506(3):3239–3258, Sept. 2021.

[84] S. Gubser, I. Klebanov, and A. Polyakov. Gauge theory correlators from non-critical string theory. *Physics Letters B*, 428(1):105–114, 1998.

[85] F. Halzen and A. D. Martin. *Quark & Leptons: An introductory course in modern particle physics*. John Wiley & Sons, 2008.

[86] Y. Harayama, F. Eisenhauer, and F. Martins. The Initial Mass Function of the Massive Star-forming Region NGC 3603 from Near-Infrared Adaptive Optics Observations. , 675(2):1319–1342, Mar. 2008.

[87] W. E. Harris. A New Catalog of Globular Clusters in the Milky Way. *arXiv e-prints*, page arXiv:1012.3224, Dec. 2010.

[88] K. Hashimoto, T. Oka, and A. Sonoda. Electromagnetic instability in holographic QCD. *JHEP*, 06:001, 2015.

[89] S. W. Hawking. Particle creation by black holes. *Communications in Mathematical Physics*, 43(3):199–220, Aug. 1975.

[90] S. He, M. Huang, and Q.-S. Yan. Logarithmic correction in the deformed ads_5 model to produce the heavy quark potential and qcd beta function. *Phys. Rev. D*, 83:045034, Feb 2011.

[91] W. Heisenberg and H. Euler. Consequences of Dirac's theory of positrons. *Z. Phys.*, 98(11-12):714–732, 1936.

[92] L. A. Hillenbrand and L. W. Hartmann. A Preliminary Study of the Orion Nebula Cluster Structure and Dynamics. , 492(2):540–553, Jan. 1998.

[93] M. Hogervorst, M. Meineri, J. Penedones, and K. S. Vaziri. Hamiltonian truncation in Anti-de Sitter spacetime. *Journal of High Energy Physics*, 2021(8):1–113, Aug. 2021.

[94] P. F. Hopkins. Variations in the stellar CMF and IMF: from bottom to top. , 433(1):170–177, July 2013.

[95] P. F. Hopkins. Why do stars form in clusters? An analytic model for stellar correlation functions. , 428(3):1950–1957, Jan. 2013.

[96] P. F. Hopkins. A new class of accurate, mesh-free hydrodynamic simulation methods. , 450:53–110, June 2015.

[97] P. F. Hopkins. A constrained-gradient method to control divergence errors in numerical MHD. , 462(1):576–587, Oct. 2016.

[98] P. F. Hopkins, M. Y. Grudić, A. Wetzel, D. Kereš, C.-A. Faucher-Giguère, X. Ma, N. Murray, and N. Butcher. Radiative stellar feedback in galaxy formation: Methods and physics. , 491(3):3702–3729, Jan. 2020.

[99] P. F. Hopkins and M. J. Raives. Accurate, meshless methods for magnetohydrodynamics. , 455(1):51–88, Jan. 2016.

[100] P. F. Hopkins, A. Wetzel, D. Kereš, C.-A. Faucher-Giguère, E. Quataert, M. Boylan-Kolchin, N. Murray, C. C. Hayward, and K. El-Badry. How to model supernovae in simulations of star and galaxy formation. , 477(2):1578–1603, June 2018.

[101] P. F. Hopkins, A. Wetzel, D. Kereš, C.-A. Faucher-Giguère, E. Quataert, M. Boylan-Kolchin, N. Murray, C. C. Hayward, and K. El-Badry. How to model supernovae in simulations of star and galaxy formation. , 477(2):1578–1603, June 2018.

[102] P. F. Hopkins, A. Wetzel, D. Kereš, C.-A. Faucher-Giguère, E. Quataert, M. Boylan-Kolchin, N. Murray, C. C. Hayward, S. Garrison-Kimmel, C. Hummels, R. Feldmann, P. Torrey, X. Ma, D. Anglés-Alcázar, K.-Y. Su, M. Orr, D. Schmitz, I. Escala, R. Sanderson, M. Y. Grudić, Z. Hafen, J.-H. Kim, A. Fitts, J. S. Bullock, C. Wheeler, T. K. Chan, O. D. Elbert, and D. Narayanan. FIRE-2 simulations: physics versus numerics in galaxy formation. , 480(1):800–863, Oct. 2018.

[103] J. P. Huchra and M. J. Geller. Groups of Galaxies. I. Nearby groups. , 257:423–437, June 1982.

[104] E. L. Hunt and S. Reffert. Improving the open cluster census. II. An all-sky cluster catalogue with Gaia DR3. , 673:A114, May 2023.

[105] D. A. Hunter, E. J. Shaya, J. A. Holtzman, R. M. Light, J. O'Neil, Earl J., and R. Lynds. The Intermediate Stellar Mass Population in R136 Determined from Hubble Space Telescope Planetary Camera 2 Images. , 448:179, July 1995.

[106] Ž. Ivezić, A. J. Connolly, J. T. VanderPlas, and A. Gray. *Statistics, data mining, and machine learning in astronomy: a practical Python guide for the analysis of survey data*, volume 8. Princeton University Press, 2020.

[107] A. Jaffe and E. Witten. Quantum yang-mills theory. *The millennium prize problems*, 1:129, 2006.

[108] O. B. JEFFREY, O. D. MEGAN, S. NICHOLAS, and M. VOIT. *COSMIC PERSPECTIVE*. PEARSON, 8th edition, 2016.

[109] A. Karch, E. Katz, D. T. Son, and M. A. Stephanov. Linear confinement and ads/qcd. *Phys. Rev. D*, 74:015005, Jul 2006.

[110] N. Katz and S. D. M. White. Hierarchical Galaxy Formation: Overmerging and the Formation of an X-Ray Cluster. , 412:455, Aug. 1993.

[111] D. Kawai, Y. Sato, and K. Yoshida. Schwinger pair production rate in confining theories via holography. *Phys. Rev. D*, 89:101901, May 2014.

[112] D. Kawai, Y. Sato, and K. Yoshida. A holographic description of the schwinger effect in a confining gauge theory. *International Journal of Modern Physics A*, 30(11):1530026, 2015.

[113] R. C. Kennicutt and N. J. Evans. Star Formation in the Milky Way and Nearby Galaxies. , 50:531–608, Sept. 2012.

[114] N. V. Kharchenko, A. E. Piskunov, E. Schilbach, S. Röser, and R. D. Scholz. Global survey of star clusters in the Milky Way. I. The pipeline and fundamental parameters in the second quadrant. , 543:A156, July 2012.

[115] N. V. Kharchenko, A. E. Piskunov, E. Schilbach, S. Röser, and R. D. Scholz. Global survey of star clusters in the Milky Way. II. The catalogue of basic parameters. , 558:A53, Oct. 2013.

[116] D. E. Kharzeev, L. D. McLerran, and H. J. Warringa. The effects of topological charge change in heavy ion collisions: "event by event p and cp violation". *Nuclear Physics A*, 803(3):227–253, 2008.

[117] J. Kim, M. Chevance, J. M. D. Kruijssen, A. T. Barnes, F. Bigiel, G. A. Blanc, M. Boquien, Y. Cao, E. Congiu, D. A. Dale, O. V. Egorov, C. M. Faesi, S. C. O. Glover, K. Grasha, B. Groves, H. Hassani, A. Hughes, R. S. Klessen, K. Kreckel, K. L. Larson, J. C. Lee, A. K. Leroy, D. Liu, S. N. Longmore, S. E. Meidt, H.-A. Pan, J. Pety, M. Querejeta, E. Rosolowsky, T. Saito, K. Sandstrom, E. Schinnerer, R. J. Smith, A. Usero, E. J. Watkins, and T. G. Williams. PHANGS-JWST First Results: Duration of the Early Phase of Massive Star Formation in NGC 628. , 944(2):L20, Feb. 2023.

[118] J. Kim, M. Chevance, J. M. D. Kruijssen, A. Schruba, K. Sandstrom, A. T. Barnes, F. Bigiel, G. A. Blanc, Y. Cao, D. A. Dale, C. M. Faesi, S. C. O. Glover, K. Grasha, B. Groves, C. Herrera, R. S. Klessen, K. Kreckel, J. C. Lee, A. K. Leroy, J. Pety, M. Querejeta, E. Schinnerer, J. Sun, A. Usero, J. L. Ward, and T. G. Williams. On the duration of the embedded phase of star formation. , 504(1):487–509, June 2021.

[119] S. P. Kim and D. N. Page. Schwinger pair production via instantons in strong electric fields. *Phys. Rev. D*, 65:105002, Apr 2002.

[120] A. M. Kondratenko and E. L. Saldin. GENERATING OF COHERENT RADIATION BY A RELATIVISTIC ELECTRON BEAM IN AN ONDULATOR. *Part. Accel.*, 10:207–216, 1980.

[121] M. R. Krumholz. *Star Formation*. 2017.

[122] M. R. Krumholz and N. Y. Gnedin. A Comparison of Methods for Determining the Molecular Content of Model Galaxies. , 729(1):36, Mar. 2011.

[123] M. R. Krumholz, C. F. McKee, and J. Bland -Hawthorn. Star Clusters Across Cosmic Time. *arXiv e-prints*, page arXiv:1812.01615, Dec 2018.

[124] M. A. Kuhn, L. A. Hillenbrand, A. Sills, E. D. Feigelson, and K. V. Getman. Kinematics in Young Star Clusters and Associations with Gaia DR2. , 870(1):32, Jan. 2019.

[125] C. J. Lada. The physics and modes of star cluster formation: observations. *Philosophical Transactions of the Royal Society of London Series A*, 368(1913):713–731, Jan. 2010.

[126] C. J. Lada and E. A. Lada. Embedded Clusters in Molecular Clouds. , 41:57–115, Jan. 2003.

[127] H. J. G. L. M. Lamers, M. Gieles, N. Bastian, H. Baumgardt, N. V. Kharchenko, and S. Portegies Zwart. An analytical description of the disruption of star clusters in tidal fields with an application to Galactic open clusters. , 441(1):117–129, Oct. 2005.

[128] S. S. Larsen. The mass function of young star clusters in spiral galaxies. , 494(2):539–551, Feb. 2009.

[129] J. Lee. PHANGS-HST: Linking Stars and Gas throughout the Scales of Star Formation. HST Proposal, Nov. 2018.

[130] J. Lee, K. L. Larson, A. Leroy, K. M. Sandstrom, E. Schinnerer, D. Thilker, A. Barnes, F. Belfiore, F. Bigiel, A. Bolatto, M. Boquien, Y. Cao, R. Chandar, J. Chastenet, M. Chevance, D. Dale, S. Deger, E. Emsellem, C. Faesi, S. Glover, K. Grasha, B. Groves, A. Hughes, J. Kim, R. S. Klessen, E. Koch, K. Kreckel, D. Kruijssen, L. Lopez, S. Meidt, E. C. Ostriker, J. Pety, E. Rosolowsky, T. Saito, P. Sanchez-Blazquez, F. Santoro, A. Sardone, A. Schruba, J. Sun, A. Usero, D. Utomo, and T. Williams. A JWST-HST-VLT/MUSE-ALMA

Treasury of Star Formation in Nearby Galaxies. JWST Proposal. Cycle 1, ID. #2107, Mar. 2021.

[131] J. Lee, B. Whitmore, D. Thilker, S. Deger, R. Chandar, K. Larson, D. Dale, J. Turner, L. Ubeda, G. Anand, M. Boquien, E. Schinnerer, A. Leroy, and Phangs Team. The PHANGS-HST Survey: A Census of Star Clusters and Multi-Scale Stellar Associations in Nearby Spiral Galaxies. In *American Astronomical Society Meeting Abstracts*, volume 53 of *American Astronomical Society Meeting Abstracts*, page 331.04, June 2021.

[132] J. C. Lee, K. M. Sandstrom, A. K. Leroy, D. A. Thilker, E. Schinnerer, E. Rosolowsky, K. L. Larson, O. V. Egorov, T. G. Williams, J. Schmidt, E. Emsellem, G. S. Anand, A. T. Barnes, F. Belfiore, I. Bešlić, F. Bigiel, G. A. Blanc, A. D. Bolatto, M. Boquien, J. den Brok, Y. Cao, R. Chandar, J. Chastenet, M. Chevance, I.-D. Chiang, E. Congiu, D. A. Dale, S. Deger, C. Eibensteiner, C. M. Faesi, S. C. O. Glover, K. Grasha, B. Groves, H. Hassani, K. F. Henny, J. D. Henshaw, N. Hoyer, A. Hughes, S. Jeffreson, M. J. Jiménez-Donaire, J. Kim, H. Kim, R. S. Klessen, E. W. Koch, K. Kreckel, J. M. D. Kruijssen, J. Li, D. Liu, L. A. Lopez, D. Maschmann, N. M. Chen, S. E. Meidt, E. J. Murphy, J. Neumann, N. Neumayer, H.-A. Pan, I. Pessa, J. Pety, M. Querejeta, F. Pinna, M. J. Rodríguez, T. Saito, P. Sánchez-Blázquez, F. Santoro, A. Sardone, R. J. Smith, M. C. Sormani, F. Scheuermann, S. K. Stuber, J. Sutter, J. Sun, Y.-H. Teng, R. G. Treß, A. Usero, E. J. Watkins, B. C. Whitmore, and A. Razza. The PHANGS-JWST Treasury Survey: Star Formation, Feedback, and Dust Physics at High Angular Resolution in Nearby GalaxieS. , 944(2):L17, Feb. 2023.

[133] J. C. Lee, B. C. Whitmore, D. A. Thilker, S. Deger, K. L. Larson, L. Ubeda, G. S. Anand, M. Boquien, R. Chandar, D. A. Dale, E. Emsellem, A. K. Leroy, E. Rosolowsky, E. Schinnerer, J. Schmidt, J. Lilly, J. Turner, S. Van Dyk, R. L.

White, A. T. Barnes, F. Belfiore, F. Bigiel, G. A. Blanc, Y. Cao, M. Chevance, E. Congiu, O. V. Egorov, S. C. O. Glover, K. Grasha, B. Groves, J. D. Henshaw, A. Hughes, R. S. Klessen, E. Koch, K. Kreckel, J. M. D. Kruijssen, D. Liu, L. A. Lopez, N. Mayker, S. E. Meidt, E. J. Murphy, H.-A. Pan, J. Pety, M. Querejeta, A. Razza, T. Saito, P. Sánchez-Blázquez, F. Santoro, A. Sardone, F. Scheuermann, A. Schruba, J. Sun, A. Usero, E. Watkins, and T. G. Williams. The PHANGS-HST Survey: Physics at High Angular Resolution in Nearby Galaxies with the Hubble Space Telescope. , 258(1):10, Jan. 2022.

[134] A. K. Leroy, E. Schinnerer, A. Hughes, E. Rosolowsky, J. Pety, A. Schruba, A. Usero, G. A. Blanc, M. Chevance, E. Emsellem, C. M. Faesi, C. N. Herrera, D. Liu, S. E. Meidt, M. Querejeta, T. Saito, K. M. Sandstrom, J. Sun, T. G. Williams, G. S. Anand, A. T. Barnes, E. A. Behrens, F. Belfiore, S. M. Benincasa, I. Bešlić, F. Bigiel, A. D. Bolatto, J. S. den Brok, Y. Cao, R. Chandar, J. Chastenet, I.-D. Chiang, E. Congiu, D. A. Dale, S. Deger, C. Eibensteiner, O. V. Egorov, A. García-Rodríguez, S. C. O. Glover, K. Grasha, J. D. Henshaw, I. T. Ho, A. A. Kepley, J. Kim, R. S. Klessen, K. Kreckel, E. W. Koch, J. M. D. Kruijssen, K. L. Larson, J. C. Lee, L. A. Lopez, J. Machado, N. Mayker, R. McElroy, E. J. Murphy, E. C. Ostriker, H.-A. Pan, I. Pessa, J. Puschnig, A. Razza, P. Sánchez-Blázquez, F. Santoro, A. Sardone, F. Scheuermann, K. Sliwa, M. C. Sormani, S. K. Stuber, D. A. Thilker, J. A. Turner, D. Utomo, E. J. Watkins, and B. Whitmore. PHANGS-ALMA: Arcsecond CO(2-1) Imaging of Nearby Star-forming Galaxies. , 257(2):43, Dec. 2021.

[135] I. Lindau, M. Cornacchia, and J. Arthur. The Stanford XFEL project - LCLS. In *Workshop on the Development of Future Linear Electron-Positron Colliders for Particle Physics Studies and for Research Using Free Electron Lasers*, pages 153–161, 9 1999.

[136] L. Liu and X. Pang. A Catalog of Newly Identified Star Clusters in Gaia DR2. , 245(2):32, Dec. 2019.

[137] S. N. Longmore, J. M. D. Kruijssen, N. Bastian, J. Bally, J. Rathborne, L. Testi, A. Stolte, J. Dale, E. Bressert, and J. Alves. The Formation and Early Evolution of Young Massive Clusters. In H. Beuther, R. S. Klessen, C. P. Dullemond, and T. Henning, editors, *Protostars and Planets VI*, pages 291–314, Jan. 2014.

[138] A. D. Mackey and G. F. Gilmore. Surface brightness profiles and structural parameters for 53 rich stellar clusters in the Large Magellanic Cloud. , 338(1):85–119, Jan. 2003.

[139] J. Maíz-Apellániz. Structural Properties of Massive Young Clusters. , 563(1):151–162, Dec. 2001.

[140] J. M. Maldacena. The Large N limit of superconformal field theories and supergravity. *Adv. Theor. Math. Phys.*, 2:231–252, 1998.

[141] M. S. Marinov and V. S. Popov. Electron-Positron Pair Creation from Vacuum Induced by Variable Electric Field. *Fortsch. Phys.*, 25:373–400, 1977.

[142] D. Masoumi, L. Shahkarami, and F. Charmchi. Effect of electromagnetic fields on deformed ads_5 models. *Phys. Rev. D*, 101:126011, Jun 2020.

[143] G. Materlik and T. Wroblewski. The TESLA X-ray free electron laser project at DESY. In *Workshop on the Development of Future Linear Electron-Positron Colliders for Particle Physics Studies and for Research Using Free Electron Lasers*, pages 39–58, 9 1999.

[144] G. Materlik and T. Wroblewski. TESLA: The superconducting electron positron linear collider with an integrated X-ray laser laboratory. Technical design report. Pt. 5: The X-ray free electron laser. Technical report, 3 2001.

[145] F. McCluskey, A. Wetzel, S. R. Loebman, J. Moreno, and C.-A. Faucher-Giguere. Disk settling and dynamical heating: histories of Milky Way-mass stellar disks across cosmic time in the FIRE simulations. *arXiv e-prints*, page arXiv:2303.14210, Mar. 2023.

[146] D. E. McLaughlin and R. P. van der Marel. Resolved Massive Star Clusters in the Milky Way and Its Satellites: Brightness Profiles and a Catalog of Fundamental Parameters. , 161(2):304–360, Dec. 2005.

[147] A. C. Melissinos. The Spontaneous breakdown of the vacuum. In *15th Advanced ICFA Beam Dynamics Workshop on Quantum Aspects of Beam Physics*, pages 564–570, 2 1998.

[148] S. Mengel and L. E. Tacconi-Garman. Medium resolution 2.3 μm spectroscopy of the massive Galactic open cluster Westerlund 1. , 466(1):151–155, Apr. 2007.

[149] S. Millstone, R. Gutermuth, S. S. R. Offner, R. Pokhrel, and M. Y. Grudić. Co-Evolution of Stars and Gas: Using Analysis of Synthetic Observations to Investigate the Star-Gas Correlation in STARFORGE. *arXiv e-prints*, page arXiv:2310.11544, Oct. 2023.

[150] V. M. Mostepanenko and V. M. Frolov. Particle creation from vacuum by homogeneous electric field with a periodical time dependence. *Yad. Fiz.*, 19:885–896, 1974.

[151] V. Mukhanov and S. Winitzki. *Introduction to Quantum Effects in Gravity*. Cambridge University Press, 2007.

[152] B. Müller, J. Rafelski, and W. Greiner. Electron shells in over-critical external fields. *Zeitschrift für Physik A Hadrons and nuclei*, 257(1):62–77, 1972.

[153] Y. Nambu. The confinement of quarks. *Scientific American*, 235(5):48–63, 1976.

[154] J. Oñorbe, S. Garrison-Kimmel, A. H. Maller, J. S. Bullock, M. Rocha, and O. Hahn. How to zoom: bias, contamination and Lagrange volumes in multi-mass cosmological simulations. , 437(2):1894–1908, Jan. 2014.

[155] M. E. Orr, B. Burkhart, A. Wetzel, P. F. Hopkins, I. A. Escala, A. L. Strom, P. F. Goldsmith, J. L. Pineda, C. C. Hayward, and S. R. Loebman. Spiral arms are metal freeways: azimuthal gas-phase metallicity variations in flocculent discs in the FIRE-2 cosmological zoom-in simulations. , 521(3):3708–3726, May 2023.

[156] L. Parker. Quantized fields and particle creation in expanding universes. i. *Phys. Rev.*, 183:1057–1068, Jul 1969.

[157] M. B. Peacock, T. J. Maccarone, C. Knigge, A. Kundu, C. Z. Waters, S. E. Zepf, and D. R. Zurek. The M31 globular cluster system: ugriz and K-band photometry and structural parameters. , 402(2):803–818, Feb. 2010.

[158] S. Perina, P. Barmby, M. A. Beasley, M. Bellazzini, J. P. Brodie, D. Burstein, J. G. Cohen, L. Federici, F. Fusi Pecci, S. Galleti, P. W. Hodge, J. P. Huchra, M. Kissler-Patig, T. H. Puzia, and J. Strader. An HST/WFPC2 survey of bright young clusters in M31. I. VdB0, a massive star cluster seen at t 25 Myr. , 494(3):933–948, Feb. 2009.

[159] G. I. Perren, M. S. Pera, H. D. Navone, and R. A. Vázquez. The Unified Cluster Catalogue: towards a comprehensive and homogeneous database of stellar clusters. , Sept. 2023.

[160] M. E. Peskin. Lectures on the theory of the weak interaction. *arXiv preprint arXiv:1708.09043*, 2017.

[161] M. E. Peskin. *Concepts of Elementary Particle Physics*. Oxford Master Series in Physics. Oxford University Press, 9 2019.

[162] M. E. Peskin. *An introduction to quantum field theory.* CRC Press, London, England, Sept. 2019.

[163] M. E. Peskin. *An introduction to quantum field theory.* CRC Press, London, England, Sept. 2019.

[164] S. Pfalzner. Universality of young cluster sequences. , 498(2):L37–L40, May 2009.

[165] J. Polchinski and M. J. Strassler. Hard scattering and gauge/string duality. *Phys. Rev. Lett.*, 88:031601, Jan 2002.

[166] H. D. Politzer. Reliable perturbative results for strong interactions? *Phys. Rev. Lett.*, 30:1346–1349, Jun 1973.

[167] V. Popov. The schwinger effect and possibilities for its observation using optical and x-ray lasers. *Journal of Experimental and Theoretical Physics*, 94:1057–1069, 2002.

[168] V. S. Popov. Production of e+e- Pairs in an Alternating External Field. *JETP Lett.*, 13:185–187, 1971.

[169] V. S. Popov. Pair Production in a Variable External Field (Quasiclassical Approximation). *Soviet Journal of Experimental and Theoretical Physics*, 34:709, Jan. 1972.

[170] V. S. Popov. Resonant pair production in a strong electric field. *Soviet Journal of Experimental and Theoretical Physics Letters*, 18:255, Oct. 1973.

[171] V. S. Popov. Spontaneous production of positrons in collisions of heavy nuclei (production cross-section and the energy spectrum of e+). *Yad. Fiz.*, 19(1):155–168, 1974.

[172] V. S. Popov. Schwinger mechanism of electron positron pair production by the field of optical and X-ray lasers in vacuum. *JETP Lett.*, 74:133–138, 2001.

[173] S. F. Portegies Zwart, S. L. W. McMillan, and M. Gieles. Young Massive Star Clusters. , 48:431–493, Sept. 2010.

[174] J. L. Powell and B. Crasemann. *Quantum Mechanics*. Addison Wesley, 1961.

[175] G. Preparata, R. Ruffini, and S.-S. Xue. The dyadosphere of black holes and gamma-ray bursts. *Astronomy and Astrophysics*, 338(3):L87–L90, 1998.

[176] W. H. Press and M. Davis. How to identify and weigh virialized clusters of galaxies in a complete redshift catalog. , 259:449–473, Aug. 1982.

[177] A. Ringwald. Pair production from vacuum at the focus of an X-ray free electron laser. *Physics Letters B*, 510(1-4):107–116, June 2001.

[178] C. D. Roberts, S. M. Schmidt, and D. V. Vinnik. Quantum effects with an x-ray free-electron laser. *Phys. Rev. Lett.*, 89:153901, Sep 2002.

[179] J. W. Rohlf and P. J. Collings. Modern physics from α to z 0. *Review Of" Modern Physics*, 12:1–1994, 1994.

[180] E. Sabbi, M. Sirianni, A. Nota, M. Tosi, J. Gallagher, L. J. Smith, L. Angeretti, M. Meixner, M. S. Oey, R. Walterbos, and A. Pasquali. The Stellar Mass Distribution in the Giant Star Forming Region NGC 346. , 135(1):173–181, Jan. 2008.

[181] M. Salaris, A. Weiss, and S. M. Percival. The age of the oldest Open Clusters. , 414:163–174, Jan. 2004.

[182] R. E. Sanderson, A. Wetzel, S. Loebman, S. Sharma, P. F. Hopkins, S. Garrison-Kimmel, C.-A. Faucher-Giguère, D. Kereš, and E. Quataert. Syn-

thetic Gaia Surveys from the FIRE Cosmological Simulations of Milky Way-mass Galaxies. , 246(1):6, Jan. 2020.

[183] G. Sarri, K. Poder, J. M. Cole, W. Schumaker, A. di Piazza, B. Reville, T. Dzelzainis, D. Doria, L. A. Gizzi, G. Grittani, S. Kar, C. H. Keitel, K. Krushelnick, S. Kuschel, S. P. D. Mangles, Z. Najmudin, N. Shukla, L. O. Silva, D. Symes, A. G. R. Thomas, M. Vargas, J. Vieira, and M. Zepf. Generation of neutral and high-density electron-positron pair plasmas in the laboratory. *Nature Communications*, 6:6747, Apr. 2015.

[184] Y. Sato and K. Yoshida. Holographic description of the Schwinger effect in electric and magnetic fields. *JHEP*, 04:111, 2013.

[185] Y. Sato and K. Yoshida. Holographic Schwinger effect in confining phase. *JHEP*, 09:134, 2013.

[186] Y. Sato and K. Yoshida. Potential Analysis in Holographic Schwinger Effect. *JHEP*, 08:002, 2013.

[187] Y. Sato and K. Yoshida. Universal aspects of holographic Schwinger effect in general backgrounds. *JHEP*, 12:051, 2013.

[188] F. Sauter. Über das Verhalten eines Elektrons im homogenen elektrischen Feld nach der relativistischen Theorie Diracs. *Zeitschrift fur Physik*, 69(11-12):742–764, Nov. 1931.

[189] F. Scheck. Muon physics. *Physics Reports*, 44(4):187–248, 1978.

[190] E. Schinnerer, A. Hughes, A. Leroy, B. Groves, G. A. Blanc, K. Kreckel, F. Bigiel, M. Chevance, D. Dale, E. Emsellem, C. Faesi, S. Glover, K. Grasha, J. Henshaw, A. Hygate, J. M. D. Kruijssen, S. Meidt, J. Pety, M. Querejeta,

E. Rosolowsky, T. Saito, A. Schruba, J. Sun, and D. Utomo. The GasStar Formation Cycle in Nearby Star-forming Galaxies. I. Assessment of Multi-scale Variations. , 887(1):49, Dec. 2019.

[191] E. Schinnerer, A. Leroy, G. Blanc, E. Emsellem, A. Hughes, E. Rosolowsky, A. Schruba, F. Bigiel, A. Escala, B. Groves, K. Kreckel, D. Kruijssen, J. Lee, S. Meidt, J. Pety, P. Sanchez-Blazquez, K. Sandstrom, A. Usero, A. Barnes, F. Belfiore, I. Bešlić, R. Chandar, D. Chatzigiannakis, M. Chevance, E. Congiu, D. Dale, C. Faesi, M. Gallagher, A. Garcia-Rodriguez, S. Glover, K. Grasha, J. Henshaw, C. Herrera, I. T. Ho, A. Hygate, M. Jimenez-Donaire, S. Kessler, J. Kim, R. Klessen, E. Koch, P. Lang, K. Larson, A. Le Reste, D. Liu, R. McElroy, J. Nofech, E. Ostriker, I. Pessa Gutierrez, J. Puschnig, M. Querejeta, A. Razza, T. Saito, F. Santoro, S. Stuber, J. Sun, D. Thilker, J. Turner, L. Ubeda, J. Utreras, D. Utomo, S. van Dyk, J. Ward, and B. Whitmore. The Physics at High Angular resolution in Nearby GalaxieS (PHANGS) Surveys. *The Messenger*, 177:36–41, Sept. 2019.

[192] S. Schmeja, N. V. Kharchenko, A. E. Piskunov, S. Röser, E. Schilbach, D. Froebrich, and R. D. Scholz. Global survey of star clusters in the Milky Way. III. 139 new open clusters at high Galactic latitudes. , 568:A51, Aug. 2014.

[193] M. Schmidt. The Rate of Star Formation. , 129:243, Mar. 1959.

[194] P. Schmüser, M. Dohlus, and J. Rossbach. *Ultraviolet and soft X-ray free-electron lasers: Introduction to physical principles, experimental results, technological challenges*. Springer, Berlin, Germany, 2009 edition, 2008.

[195] R. D. Scholz, N. V. Kharchenko, A. E. Piskunov, S. Röser, and E. Schilbach. Global survey of star clusters in the Milky Way. IV. 63 new open clusters detected by proper motions. , 581:A39, Sept. 2015.

[196] M. D. Schwartz. *Quantum Field Theory and the Standard Model*. Cambridge University Press, 3 2014.

[197] J. Schwinger. On quantum-electrodynamics and the magnetic moment of the electron. *Phys. Rev.*, 73:416–417, Feb 1948.

[198] J. Schwinger. Quantum electrodynamics. i. a covariant formulation. *Phys. Rev.*, 74:1439–1461, Nov 1948.

[199] J. Schwinger. On gauge invariance and vacuum polarization. *Phys. Rev.*, 82:664–679, Jun 1951.

[200] G. W. Semenoff and K. Zarembo. Holographic schwinger effect. *Phys. Rev. Lett.*, 107:171601, Oct 2011.

[201] L. Shahkarami and F. Charmchi. Confining D-Instanton Background in an External Electric Field. *Eur. Phys. J. C*, 79(4):343, 2019.

[202] L. Shahkarami, M. Dehghani, and P. Dehghani. Holographic schwinger effect in a d-instanton background. *Phys. Rev. D*, 97:046013, Feb 2018.

[203] D. She, S.-Q. Feng, Y. Zhong, and Z.-B. Yin. Chiral magnetic currents with QGP medium response in heavy ion collisions at RHIC and LHC energies. *Eur. Phys. J. A*, 54(3):48, 2018.

[204] L. S. Sparke and J. S. Gallagher III. *Galaxies in the universe: an introduction*. Cambridge University Press, 2nd edition, 2007.

[205] V. Springel. The cosmological simulation code GADGET-2. , 364(4):1105–1134, Dec. 2005.

[206] M. Srednicki. *Quantum field theory*. Cambridge University Press, 2007.

[207] K.-Y. Su, P. F. Hopkins, C. C. Hayward, C.-A. Faucher-Giguère, D. Kereš, X. Ma, and V. H. Robles. Feedback first: the surprisingly weak effects of magnetic fields, viscosity, conduction and metal diffusion on sub-L* galaxy formation. , 471(1):144–166, Oct. 2017.

[208] S. Tomonaga. On a Relativistically Invariant Formulation of the Quantum Theory of Wave Fields*. *Progress of Theoretical Physics*, 1(2):27–42, 08 1946.

[209] T. G. Trippe, A. Barbaro-Galtieri, R. L. Kelly, A. Rittenberg, A. H. Rosenfeld, G. P. Yost, N. Barash-Schmidt, C. Bricman, R. J. Hemingway, M. J. Losty, M. Roos, V. Chaloupka, and B. Armstrong. Review of particle properties. *Rev. Mod. Phys.*, 48:S1–S245, Apr 1976.

[210] G. J. Troup and H. S. Perlman. Pair production in a vacuum by an alternating field. *Phys. Rev. D*, 6:2299–2299, Oct 1972.

[211] I. C. E. Turcu, S. Balascuta, F. Negoita, D. Jaroszynski, and P. McKenna. Strong field physics and QED experiments with ELI-NP 2×10PW laser beams. In *Exotic Nuclei and Nuclear/Particle Astrophysics (V) From Nuclei to Stars: Carpathian Summer School of Physics 2014*, volume 1645 of *American Institute of Physics Conference Series*, pages 416–420, Feb. 2015.

[212] D. A. VandenBerg, K. Brogaard, R. Leaman, and L. Casagrande. The Ages of 55 Globular Clusters as Determined Using an Improved VĤB_TO Method along with Color-Magnitude Diagram Constraints, and Their Implications for Broader Issues. , 775(2):134, Oct. 2013.

[213] V. Vansevičius, K. Kodaira, D. Narbutis, R. Stonkutė, A. Bridžius, V. Deveikis, and D. Semionov. Compact Star Clusters in the M31 Disk. , 703(2):1872–1883, Oct. 2009.

[214] E. Vasiliev. Proper motions and dynamics of the Milky Way globular cluster system from Gaia DR2. , 484(2):2832–2850, Apr. 2019.

[215] J. Von Neumann. *Mathematical foundations of quantum mechanics: New edition*, volume 53. Princeton university press, 2018.

[216] V. Voronyuk, V. D. Toneev, W. Cassing, E. L. Bratkovskaya, V. P. Konchakovski, and S. A. Voloshin. Electromagnetic field evolution in relativistic heavy-ion collisions. *Phys. Rev. C*, 83:054911, May 2011.

[217] A. R. Wetzel, P. F. Hopkins, J.-h. Kim, C.-A. Faucher-Giguère, D. Kereš, and E. Quataert. Reconciling Dwarf Galaxies with ΛCDM Cosmology: Simulating a Realistic Population of Satellites around a Milky Way-mass Galaxy. , 827:L23, Aug. 2016.

[218] J. P. Williams, R. K. Mann, C. N. Beaumont, J. J. Swift, J. D. Adams, J. Hora, M. Kassis, E. A. Lada, and C. G. Román-Zúñiga. Diverse Protostellar Evolutionary States in the Young Cluster AFGL961. , 699(2):1300–1306, July 2009.

[219] F. L. Wilson. Fermi's theory of beta decay. *American Journal of Physics*, 36(12):1150–1160, 1968.

[220] E. Witten. Anti-de Sitter space and holography. *Adv. Theor. Math. Phys.*, 2:253–291, 1998.

[221] T. K. Wyder, P. W. Hodge, and D. B. Zucker. Hubble Space Telescope Observations of the Hubble Clusters in NGC 6822: Ages and Structure. , 112(775):1162–1176, Sept. 2000.

[222] Y. B. Zeldovich and V. S. Popov. Electronic structure of superheavy atoms. *Uspekhi Fiz. Nauk*, 105(11):403–440, 1971.

[223] P. Zerwas. W & z physics at lep. *The European Physical Journal C-Particles and Fields*, 34:41–49, 2004.

[224] S.-J. Zhang and E. Abdalla. Holographic Schwinger effect in a confining background with Gauss–Bonnet corrections. *Gen. Rel. Grav.*, 48(5):60, 2016.